HARVARD UNIVERSITY
Graduate School of Arts and Sciences

DISSERTATION ACCEPTANCE CERTIFICATE

The undersigned, appointed by the

School of Engineering and Applied Sciences

have examined a dissertation entitled:

"Femtosecond laser direct writing of 3D metallic structures and 2D graphite"

presented by : Seungyeon Kang

candidate for the degree of Doctor of Philosophy and here by certify that it is worthy of acceptance.

Signature ______________________

Typed name: Professor E. Mazur

Signature ______________________

Typed name: Professor E. Hu

Signature Ken Crozier

Typed name: Professor K. Crozier

Date: *April 11, 2014*

Femtosecond laser direct writing of 3D metallic structures and 2D graphite

A thesis presented
by

Seungyeon Kang

to
The School of Engineering and Applied Sciences
in partial fulfillment of the requirements
for the degree of
Doctor of Philosophy
in the subject of

Applied Physics

Harvard University
Cambridge, Massachusetts
April 2014

Thesis advisor
Eric Mazur

Author
Seungyeon Kang

Femtosecond laser direct writing of 3D metallic structures and 2D graphite

Abstract

This thesis explores a novel methodology to fabricate three dimensional (3D) metal-dielectric structures, and two dimensional (2D) graphite layers for emerging metamaterials and graphene applications. The investigations we report here go beyond the limitations of conventional fabrication techniques that require multiple post-processing steps and/or are restricted to fabrication in two dimensions. Our method combines photoreduction mechanism with an ultrafast laser direct writing process in innovative ways. This study aims to open the doors to new ways of manufacturing nanoelectronic and nanophotonic devices. With an introductory analysis on how the various laser and chemical components affect the fabrication mechanism, this dissertation is divided into three sections.

First, we present our work on fabrication of metal structures in two dimensions with a focus on patterning silver crystals in a 2D array for plasmonic applications. We analyze the composition and structure of the crystals and discuss the advantages of the laser crystal growth procedure compared to conventional wet-chemistry techniques. We establish that the addition of alcohol as a solvent aids in the 2D crystal patterning process by promoting silver nanoseed growth.

Second, we describe our fabrication of 3D silver nanostructures in two different matrices: polyvinylpyrrolidone and gelatin. We analyze how different polymers can give various structural and optical properties to the matrices. We show that we can direct laser write more than 16 layers of silver structures embedded in a polymer matrix.

Third, we perform a systematic study of a laser-driven reduction process of graphene oxide to graphene by varying both the laser fluence and the pulse repetition rate. We conclude that the reduction process has both thermal and non-thermal components, and the fabricated 2D graphite patterns written using only non-thermal mechanisms may produce higher quality structures.

Finally, in the appendix of this thesis, we describe a Z-scan method to further probe the photoreduction mechanism important to both metal structure and graphene writing and present preliminary results.

Contents

Citations to previously published work

Parts of this dissertation cover research reported in the following articles:

1. S. Kang*, K. Vora*, E. Mazur, "Direct-laser Metal Writing Inside a Gelatin Matrix for Sub-100 nm 3D Silver Nanostructures," *soon to be submitted for publication*
2. K. Vora*, S. Kang*, E. Mazur, "Femtosecond laser direct writing of single crystalline hexagonal silver prisms," *submitted for publication in Applied Physics Letters.*
3. K. Vora, S. Kang, S. Shukla, E. Mazur, "Fabrication of disconnected three-dimensional silver nanostructures in a polymer matrix," *Applied Physics Letters*, **100**, 063120, 2012.
4. K. Vora, S. Kang, E. Mazur, "A Method to Fabricate Disconnected Silver Nanostructures in 3D," *Journal of Visualized Experiments*, **69**, e4399, 2012.
5. K. Vora, S. Kang, S. Shukla, E. Mazur, "Three-dimensional silver nanostructure fabrication through multiphoton photoreduction," *SPIE 2012 Photonics West Conference Proceedings*, (San Francisco, CA), 2012.
6. K. Vora, S. Kang, S. Shukla, E. Mazur, "2D and 3D Writing of Silver Nanostructures Through Multiphoton Photoreduction," *OSA 2011 Frontiers in Optics Conference Paper*, (San Jose, CA), 2011.
7. M. Moebius*, K. Vora*, P. Munoz, S. Kang, G. Deng, E. Mazur, "Direct Laser

Writing of 3-D Diffraction Gratings and Diffraction Optics," *Manuscript under preparation*

8. S. Kang, E. Mazur, K. Vora, "Micro-and-Nano-Fabrication of Connected and Disconnected Structures in Three-Dimensions Using Ultrafast Laser Pulses," **International Patent. WO2012100167 A3**

9. S. Kang, E. Mazur, K. Vora, "Systems and Methods for fabrication of metalized structures within a polymeric suport matrix," **International Patent Application No. PCT/US2014/014121, Patent pending**

10. S. Kang, M. Moebius, E. Mazur, K. Vora, "Crystal Growth Through Irradiation With Short Laser Pulses," **International Patent Application No. PCT/US2013/71676, Patent pending**

Acknowledgments

This research and the past six years of my wonderful graduate school life would have been impossible without the support from a countless number of people including my advisor, thesis committee, Mazur group members, collaborators, friends, and family. I am very grateful to have had the opportunity to work for my advisor, Professor Eric Mazur. I truly appreciate all his advice, his relentless support, his positive attitude, and his constant demand for excellence. I am thankful for the many opportunities and guidance he has provided me, and for giving us the freedom in research and teaching us valuable presentation skills. It was valuable to learn that in addition to excellent research, a true scientist should also know how to communicate about his/her research effectively. I would also like to thank my committee, Professor Ken Crozier and Professor Evelyn Hu, for their insight and feedback, and Professor Mike Aziz and Professor Frans Spaepen for their advice on my research. I have great respect for all of them.

Mazur group was inarguably the best group to spend the past 5 years. I couldn't have made it through without all their help and support. YuTing and I both joined the Mazur group around the same time in our second year. We took many same classes, share many great memories and went through hardships together. I greatly value her friendship and her support. Without the help from our metamaterials/micromachining subgroup members, Kevin, Michael, Phil, Yang, and Shobha, the content of this thesis would be nowhere close to where it is now. I got a lot of advice from Paul and Valeria when I first joined the group. I admire their integrity, extensive knowledge, and passion for learning. Chris helped me with the Z-scan experiments and the GO project later on. I was able to learn so much from Chris. I was fortunate enough to share so many fun memories and adventures with Ben and Kelly. I also had a great time working with Kelly on Z-scan measurements during her 299r project. In addition to being great friends, Orad made beautiful gold contacts for me, Guoliang helped us with the zone plate designs and Kasey helped me a lot with illustrator, latex and other things that made things look a lot prettier. I had so much fun teaching AP50 with Kelly and Phil. Fauzy was a great friend and a mentor. Renee's dumpling/sushi parties were awesome. There are too many good memories of the Mazur group that I cannot list every single one of them. I cannot picture myself having worked for any other advisor and being part of any other group!

Virginia Casas had the answer to any and all administrative questions and have helped me in so many ways. My PhD would have taken longer without her! There are some amazing staff members at the Center for Nanoscale Science at Harvard (CNS), without whom, this work would not be possible. JiangDong Deng, Arthur McClelland, Adam Graham, David Lange, Nicholas Antoniou, and Jason Tresback were always available to help and support my research in any way possible. Their contributions to this work, and to the CNS, are truly invaluable. I would like also like to thank our collaborators, Professor Willie Padilla and Wenchen for THz characterization, and Professor Cleber Mendonca for helpful discussions on the Z-scan measurements. I would like to acknowlege Zach Gault with his help on annealing experiments during his 299r, Jungmo Choi for fruitful discussions, JaeYoung Ahn for his help with NMR measurements, JungYoon Sun for his help with tensile test measurements, Thierry Sarnet and Paul Webster for their help with rendering and 3D images, and Nina Hong (at J.A Woollam) for her help with ellipsometry measurements. This work would have been far more difficult without all these people's help, support, and assistance.

I have had the opportunity to learn from extremely intelligent and talented colleagues and friends within our department. I value all the fun memories and the fruitful discussion I had with Mikhail, Romain, Jing, Tobias, and Omer.

Finally, this work could not have been possible without the support of some very close friends and family. JungHoon, TaeWook, DaIn, JongHyuk, JeeHye, JongHo, Thoomim, ChungJong during the first couple of years in graduate school made my life so much more exciting. Also without Yejin, Eunmi, EunGook, Junhyun, JungOok, YongSeok, ELP family, and friends from the 84, 85-moim, my life at Harvard would have been completely different, much less interesting, and much less enjoyable. In addition to my friends, the never-ending support of my parents, my grandmother and my brother drove me to succeed in this endeavor. From 6,800 miles away they constantly reminded me of their love and support and pride in my achievements. They were the ones who truly kept me moving toward my goals.

SeungYeon (Sally) Kang

Cambridge, Massachusetts

April, 2014

Acknowledgements of Financial Support

This thesis is based on work funded by the Air Force Office of Scientific Research (AFOSR) under contracts, FA9550-09-1-0546-DOD35CAP, FA9550-10-1-0402-DOD35 CAP, the National Science Foundation (NSF) grant, DMR-0820484, and the Harvard University Center for the Environment (HUCE) Research Fellowship.

To my loving family

Chapter 1

Introduction

Increasing number of novel materials and structures are being designed everyday to revolutionize and engineer our future. New fabrication methods to complement the development must be aligned with the design goals for actual realization of these devices. We motivate this thesis by providing an introduction to some of the emerging optical and electrical systems that exhibit extraordinary properties and discuss the significance of developing new nanomanufacturing methods for rapid, cost-effective and accurate prototyping.

1.1 Motivation

The dynamic nature of future optical and electrical systems generates novel materials and structures that require a flexible material choice and high levels of integration, especially in 3D. Photonic crystals, metamaterials and graphene based applications are some of the interesting systems to look into.

A photonic crystal is an artificial structure that exhibits a periodic variation of dielectric constant of material [1–3]. Such structures have a similar effect on propagation of photons, as the periodic variation of electric potential in regular crystals on propagating electrons [1–3]. As a result a photonic bandgap - a frequency range, for which the propagation of photons in a certain direction is forbidden, occurs [1–3]. Even though photonic crystals have been studied for a while, the development in the recent 3D fabrication process enabled new types of 3D photonic crystals leading to more exciting future applications [4–8]. Devices based on photonic crystals allow tailoring propagation of light in a desired manner and provide many fascinating physical phenomena such as control of spontaneous emission, sharp bending of light, lossless guiding, and tri-refrigence [1–8].

Metamaterials are artificial materials structurally engineered to provide properties that are not available in nature by interacting or controlling electromagnetic waves [9, 10]. These materials usually gain their properties from their carefully designed structures rather than their compositions [9, 10]. Periodicity is often a typical feature found in metamaterials, which consists of repeated unit cells containing one or more conducting resonators [9–11]. However, unlike photonic crystals, a typical unit cell size in metamaterials has to be much smaller than the free-space wavelength, so that the metamaterial structure can be seen as homogenous from an electromagnetic point of view [9–11]. Ever since the first reported actual experimental demonstration of a metamaterial in the year 2000 by Dr. Smith and his colleagues [12, 13], more complex and sophisticated designs of metamaterials have been developed with a focus on negative refractive index metamaterials [11, 14–23]. Negative index metamaterials (or left handed materials) raise the possibility of inventing super lenses that can have a spatial resolution below the diffraction limit of the wavelength, and of creating invisible cloaks [11, 14–23]. Negative refractive index is a property that is not found in any naturally occuring material [11, 24]. Almost all materials have positive values for both permittivity (ε) and permeability (μ), except materials such as metals (ex. silver and gold) that have negative ε at visible wavelengths and some magnetic materials that have negative μ [24]. Refractive index n can be determined from equation 1.1:

$$n = \pm\sqrt{\varepsilon\mu}, \tag{1.1}$$

While normal materials possess both positive ε and μ and give a positive n value, engineered metamaterials such as metamaterials can have $\varepsilon < 0$ and $\mu < 0$, resulting in a real n value. In this case, it is necessary to take the negative square root for n which would give a negative refractive index, giving a unique property to metamaterials [11, 25]. Therefore by precisely controlling gradients in both permittivity and permeability, light propagation can be engineered to form advanced lenses (superlenses) and optics, or even invisibility cloaks [9, 10, 26]. Figure 1.1 is a summary diagram for various materials and their refractive index.

Even though there has been many ground-breaking theoretical advances in recent years, experimental advances for infrared and optical metamaterial devices have been hampered by the difficulty in patterning metals in three dimensions (3D) at the submicrometer scale [27]. Figure 1.2 shows some examples of complex metamaterial structures that require a multi-component structure in 3D. Three-dimensional (3D) nanofabrication is important for realizing various types of photonic crystals and metamaterials. [14, 27, 28] Although various 3D designs that require metal and dielec-

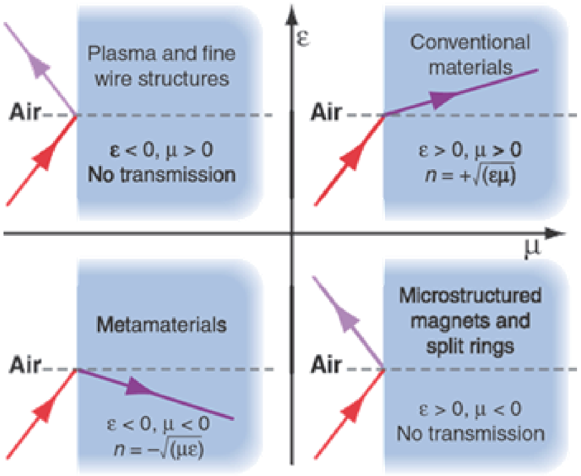

Figure 1.1: Summary diagram of refractive index properties of various materials. Adapted from reference [24].

tric components have been studied, a limited number of methods has been developed that allow fabrication of these 3D nanostructures with limitations such as lack of patterning capabilities and/or requiring many time-consuming steps [8, 14, 16, 27–31].

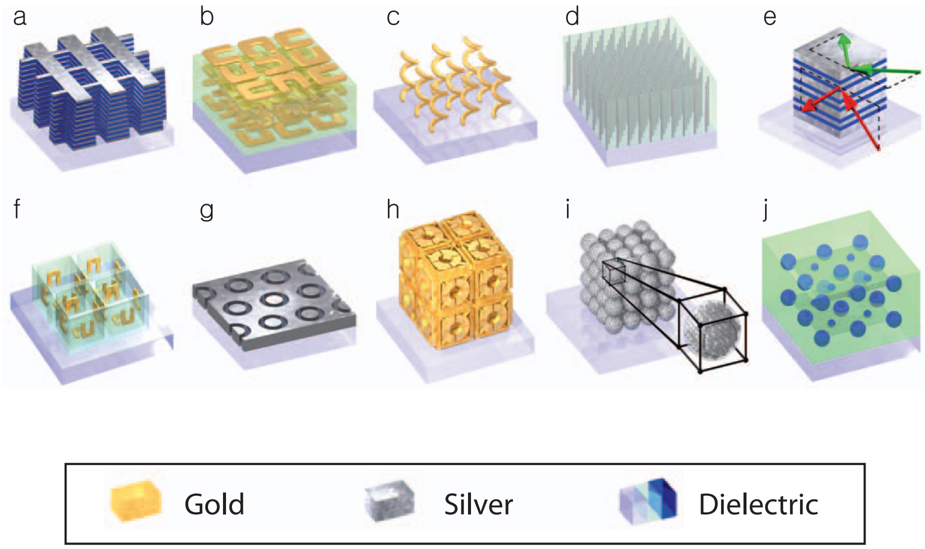

Figure 1.2: Examples of complex 3D metamaterials. Adapted from reference [27].

Lastly, graphene based systems are also one of the most interesting developments in the 21st century. Since its appearace in 2004 [32], graphene has gained immense interest due to its extraordinary electronic, optical, thermal, and mechanical properties. It is believed to be the thinnest and strongest material ever found [33, 34] and its optical properties, high surface area, and high capacitance allow graphene to be used in various applications [33–35], such as graphene optics [36], field-effect transistors (FETs) [37–39], photovoltaics and transparent electodes [40,41], microsensors [42, 43], optical modulators [44], supercapacitors [45, 46], and even as graphene metamaterials [47–50]. However, as in the photonic crystal and metamaterials case, the main barrier to commercializing graphene-integrated devices is from a lack of patternable fabrication method that is reliable, scalable and cost-effective [33, 51].

New nanomanufacturing methods are critical for advances in nanoelectronics and nanophotonics. This is critical for the progression of fundamental research as well as in helping research move from the lab to commercial products. Fabrication of next-generation devices will require techniques that produce patterned subwavelength features in three dimensions while spanning large volumes to deploy advanced materials as fast as possible, at a fraction of cost.

1.2 Aim

Our work starts from a basis that by investigating various chemistries and laser parameters to combine a photoreduction reaction with a femtosecond laser assisted direct laser writing technique, we can fabricate complex nanostructures. Our goal is to develop a new method of fabricating the next generation of materials, such as metamaterials and graphene-integrated systems, and to realize and advance nanoelectronic-and nanophotonics-devices. In this dissertation I aim to address:

1. The principles of a direct laser writing technique.

2. The critical difference with previous 3D fabrication methods that allows us to fabricate 3D metal-dielectric structures, in a simple, reliable, and cost-effective manner.

3. The unique properties of our fabricated matrices.

4. A systematic study on the fabrication process of graphene layers using a direct laser writing technique.

We hope the investigations reported in this dissertation shed light on new ways of realizing nanophotonics and graphene integrated devices in the future.

1.3 Organization of the dissertation

Chapter 2 gives an overview of the background principles and techniques that are necessary for the understanding and motivation of this work. Specifically, it focuses on explaining the need for an innovative system that can overcome previous limitations in conventional fabrication techniques to realize complex systems in the future.

Chapter 3 discusses the development of our direct laser writing method of 3D embedded metal structures and 2D graphite patterns. It elucidates on the various laser and chemical components and their roles in this new method.

Chapter 4 discusses the fabrication of 2D metal direct laser writing technique with a focus on patterning 2D silver hexagonal crystals.

Chapter 5 discusses the fabrication of 3D silver nanostructures that are embedded in polymer matrices and gives examples of applications that are achievable with this technique.

Chapter 6 studies the 2D fabrication technique of reducing graphene oxide films to produce 2D graphite (graphene layers). A systematic study of the photoreduction process of graphene oxide to graphene is conducted by varying both the laser fluence and the repetition rate.

Chapter 7 summarizes the work contained within this thesis and discusses the implications and potential directions for future research.

Chapter 2

Fabrication techniques for 2D & 3D nanosystems

Advances in material nanofabrication are critical for the progression of basic research as well as in helping research move from the lab to commercial products. Bottom-up methods such as self-assembly, deposition, or wet chemistry can be used to make large quantities of nanostructures in a cost effective manner but provide limited freedom in the design of the structures. A top-down approach that involves micromachining and lithography techniques can create complicated nanosystems with high resolution but are often very expensive, very slow and are limited to two dimensions. These drawbacks of conventional nanofabrication techniques make the task of manufacturing new materials for future optical and electrical applications difficult. This chapter discusses the conventional fabrication techniques that are currently widely used for making metal/dielectric nanostructures, and graphene, which recently has been getting a lot of interest due to its superior electrical and thermal properties. It concludes with a discussion of the importance of the innovative nanomanufacturing methods that are discussed in the subsequent chapters.

2.1 Conventional fabrication techniques

Conventional lithographic techniques have been sufficient for traditional silicon based 2D technologies but may not be sufficient to fabricate complex three dimensional structures. Three dimensional fabrication techniques that utilize the concept of self-assembly, multiphoton absorption and ultrafast-laser micromachining have been suggested and have been continuously studied [6, 7, 18, 27–29, 52–68].

2.1.1 Lithography methods

Photolithography is an inherently 2D fabrication technique that uses optical light on a photo-reactive material with a mask to acquire patterned structures. It goes through a series of steps: cleaning of the sample, spin coat of photoresist, alignment of photo-mask, exposure to a light source, developing of the exposed or unexposed area (depending on the type of photoresist), deposition of other materials if necessary, etching to reveal the patterns, and finally removal of the remaining photoresist. It is a well developed method with a fairly long history. However, due to the diffraction limit of light, it is not an effective technique to create high resolution structures, and problems such as limited aspect ratio and slanted side walls arise. In order to create 3D structures, these 2D structures can be repeatedly patterned and layered on top of each other, but as feature sizes get smaller and smaller, alignment becomes very difficult and time consuming.

E-beam lithography is analogous to photolithography but instead uses a focused electron beam to scan and directly write patterns to achieve a higher resolution. A layer by layer stacking method can be used to fabricate 3D structures, but e-beam lithography suffers from low throughput and also from complications during the stacking process. Figure 2.1(a) shows a four-layer optical metamaterial fabricated from repeated processes of e-beam lithography, spin coating of a space layer, and careful alignment.

Focused ion beam (FIB) lithography, often also referred to as FIB milling or FIB etching, uses a focused beam of ions (e.g., gallium) to sputter atoms from the surface to create a structured pattern on the surface [22]. It is less time consuming compared to the e-beam method and works best for single layer rapid prototyping [22, 69]. To create 3D structures, FIB lithography can also be used in a layer-by-layer stacking method, or when combined with other fabrication methods it can be useful in cutting the 3D stack into prisms or other optical components [14]. Figure 2.1(b) shows a negative index metamaterial prism fabricated from a layer-by-layer method combined with FIB milling.

Nanoimprint lithography (NIL), often referred to as 3D stamping method, is a molding technology for patterning deformable materials such as polymers. [70]. Patterns are transferred by mechanical deformation of the resist via a stamp rather than a photo- or electro-induced reaction in the resist as in most lithographic methods, and therefore the resolution of the technique is not limited by the wavelength of the light source; rather, the smallest attainable features are given solely by stamp fabrication [71]. NIL is great for single layer structures due to its high throughput,

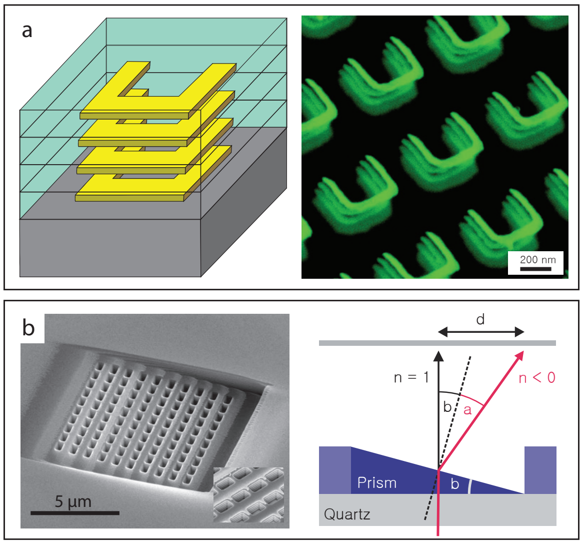

Figure 2.1: (a) A schematic diagram of one unit cell of a 4 layer-by-layer fabricated metamaterial structure (left) and its scanning electron microscopy (SEM) image (right) (b) An SEM image of a 3D fishnet NIM prism (left) and a geometry diagram of the optical setup using the NIM prism (right). 21-layer fishnet structure made from layer-by layer e-beam deposition was transformed into a prism using FIB milling. The inset image shows a magnified view of the fishnet structure. Negative index of refraction can be measured by determining distance d. Adapted from references [30] and [14].

allowing it to be suitable for large-scale production of nanoelectonics and optical metamaterials [22, 71]. However, as in other lithography techniques, a layer by layer stacking method needs to be implemented in order to incorporate other material components (such as metal) or to create a multi-layered 3D structure [72, 73].

2.1.2 3D printing

3D printing, often also referred to as inkjet printing or direct writing, is an attractive alternative technique for 3D design and metallic electrode writing for printed electronic and optoelectronic devices [74–77]. It uses a concentrated ink extruded through a tapered cylindrical nozzle that is translated using a three-axis, motioncontrolled stage. [74] With a sequential application of layers combined with computer modeling, a complex 3D structure can be achieved. Figure 2.2 shows some of the complex 3D structures that Lewis and her team fabricated [74–76]. However, the resolution achieved in this technique is generally on the order of 100 μm [74, 78], it only allows fabrication of completely interconnected structures (as in Figure 2.2(a)) and it requires a substrate to support the extruded ink (as in Figure 2.2(b)). Another drawback of this technique is that synthesizing an ink that has the right viscosity with high conductivity can be very challenging [77].

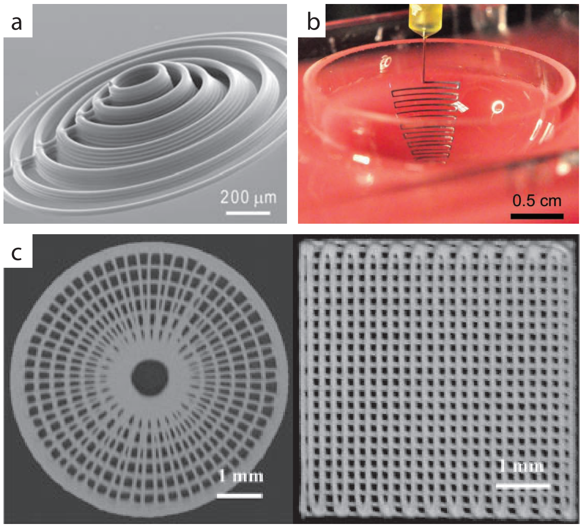

Figure 2.2: 3D printed structures from Jennifer A. Lewis and her team. (a) SEM images of multilayer silver microelectrodes patterned with a 30-μm nozzle. (b) An optical image of an antenna during the printing process. (c) Optical images (top view) of a 3D array (left) and 3D periodic lattice assembled from concentrated $BaTiO_3$ nanoparticle inks deposited through a 100-μm nozzle. Adapted from [74], [75] and [76].

2.1.3 Self-assembly

Unlike the methods discussed in previous sections, self-assembly is a bottom-up technical approach to fabrication that is easy and cost effective. It has been used to prepare inverse opal photonic crystals [6] and optical and plasmonic metamaterials [52, 79] (Figure 2.3). It is an effective method to use various materials to create composite structures. Gaps and pores of the structures can be filled with various liquids and polymers, and can also be filled in with metals by chemical vapor deposition (CVD), atomic layer deposition (ALD), or electroplating [6, 29, 52]. However in addition to the post processing steps to include other elements, it involves many steps such as heat treatment, surfactant encapsulation, or drying, can lose stability when exposed to high heat, and requires highly homogenous nanoparticles or well defined block co-polymers as starting materials [6, 7, 29]. Also it is not a true 3D patterning method and does not allow fabrication of arbitrary designs.

2.1.4 Direct laser writing

Direct laser writing (DLW) is similar to photolithography in a sense that it uses photosensitive materials. However, direct laser writing does not require photomasks or optical setups to achieve patterns but instead utilizes spatial confinement of the laser beam to draw patterns by scanning the beam or moving the sample stage. Ultrafast laser direct writing (multiphoton lithography) especially uses pulsed ultrafast lasers to modify the refractive properties or induce photoreduction through nonlinear light-matter interactions [53–57]. The materials to be patterned are transparent to the laser wavelengths and the pulses are focused at arbitrary points in the bulk or at the

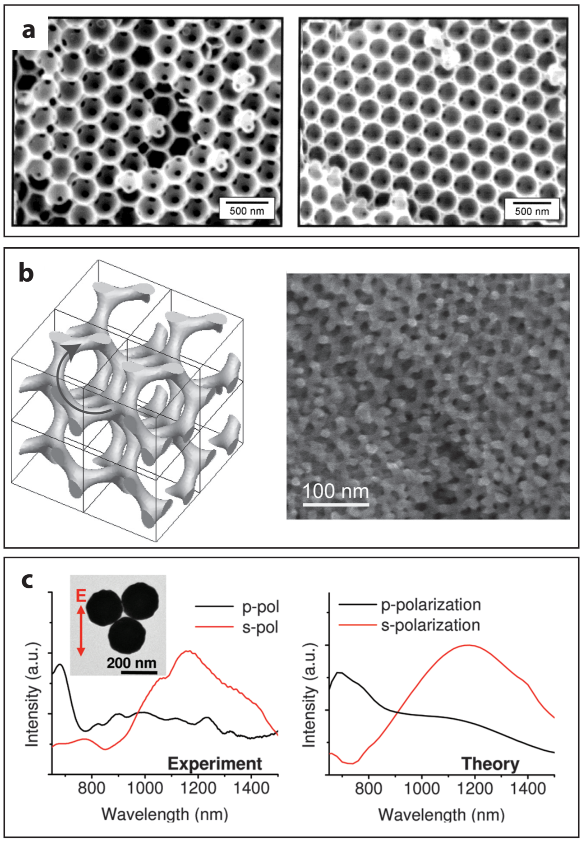

Figure 2.3: (a) SEM images of three-dimensionally ordered macroporous photonic structure made from silica (left) and mercaptopropyl silica (right), (b) 3D gold metamaterial based on isoprene-block-styrene-block-ethylene oxide blockcopolymer self-assembly. Left is a computer-simulated view of the single gyroid structure and right is an SEM image of a fabricated gyroid metamaterial structure. (c) A trimer nanoparticle cluster plasmonic metamaterial that shows magnetic dipole resonance. Plots show experimental and theoretical s- and p-polarized scattering spectra for an individual trimer shown in the inset. Adapted from references [6], [52] and [79].

surface of the substrates. Thus, devices can be patterned in three dimensions using x-, y- and z-translation.

2.1.4.1 Multi-photon / Two-photon polymerization

Multiphoton absorption (MPA) is the process in which two or more photons are absorbed by an atom simultaneously or in a very short allowable time, thereby allowing the same effects of the absorption process of a single higher energy photon [58]. Since the electronic transition in a material is driven by multiple photons simultaneously, the probability of MPA depends on the intensity of the light which leads to absorptions only within a certain focal volume of the beam where the intensity is the highest. Figure 2.4 shows single photon absorption vs. two photon absorption using a fluorescent dye. Through this nonlinear absorption at the focal point, one can initiate a polymerization process in a thick monomer layer to fabricate intricate three-dimensional polymer structures. In contrast to conventional laser microfabrication techniques, such as ablation or nonlinear lithography on planar material layers, this technique integrates both the multiphoton absorption process and the ultrafast-laser micromachining process to allow direct laser fabrication of three dimensional structures with feature sizes below the diffraction limit.

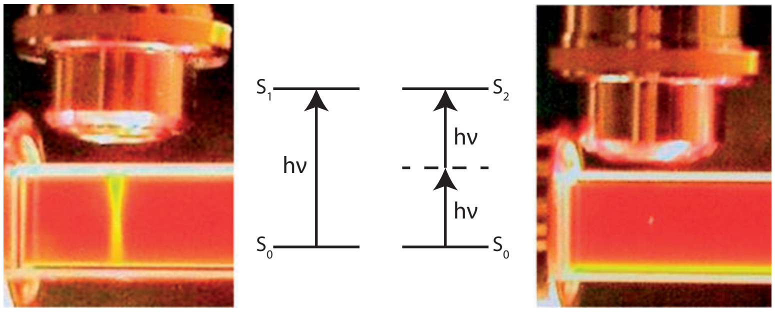

Figure 2.4: Fluorescence from a solution of rhodamine B caused by single-photon excitation from a UV lamp (left) and by two-photon excitation from a mode-locked Ti:sapphire laser operating at a wavelength of 800 nm (right). Adapted from reference [60].

However, most of the direct laser writing studies were done on polymer/dielectric materials and are not suitable for various metamerial designs [59,60]. Many metamaterial designs are based on metal/dielectric composites [18,27], and therefore, incorporating metal compositions into a bulk dielectric medium is crucial. This typically requires multiple time-consuming post steps such as removing the unnecessary polymer, ALD, CVD, or chemical electroplating in order to add a metal layer onto the 3D polymeric templates made with lithography, etching, printing, or two photon polymerization. Rill et al. were able to fabricate a 3D photonic metamaterial using a DLW followed by CVD of silver (Figure 2.5(a)) [61]. Gansel et al. created gold helix photonic metamaterial that acts as a broadband polarizer (Figure 2.5(b)) [28].

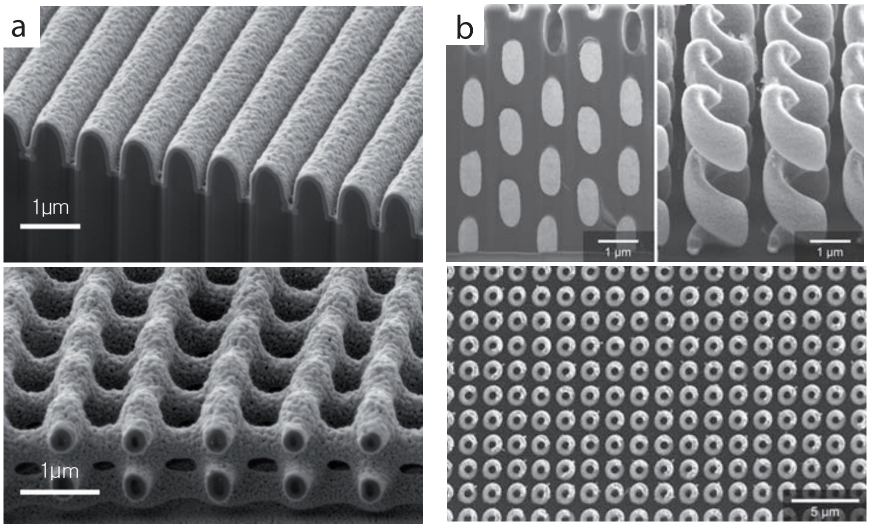

Figure 2.5: (a) SEM images of 3D structures made with DLW and CVD. The oblique views show structures that have been cut by a focused-ion beam after fabrication to reveal the interior (rather than an edge). (b) SEM images of 3D structures made with DLW and gold electroplating procedure. Top two images show focused-ion-beam (FIB) cut view of the interior before and after the removal of the polymer by plasma etching. Bottom is a top-view image revealing the circular cross section of the helices. Adapted from references [61] and [28].

In addition to the fact that it takes time-consuming post processing steps to create metal/dielectric composite structures, direct laser writing of polymers can create only continuous structures.

2.1.4.2 Direct laser writing of metal structures

A recently new application is to utilize multi-photon absorption (MPA) to create metal or partially metal structures. This is especially important because 3D metal structures open the door to applications in electrical circuits. There are basically two ways to fabricate 3D structures that include metals. The first method is to use selective post processing steps to deposit metals on pre-made polymer structures that were created with MPA as explained in the previous section. The second is to use MPA to directly deposit metal.

For direct deposition of metals by MPA, numerous chemistry methods [62–68]. These chemistries generally involve the photoreduction of metal ions dissolved in an aqueous medium. Several 2D and 3D structures that were fabricated by Kawata and his coworkers are shown in Figure 2.6.

This method allows only one-layer structures due to the lack of a supporting matrix and the fabricated structures usually have a high surface roughness. Section 2.2 discusses our approach to resolving these limitations.

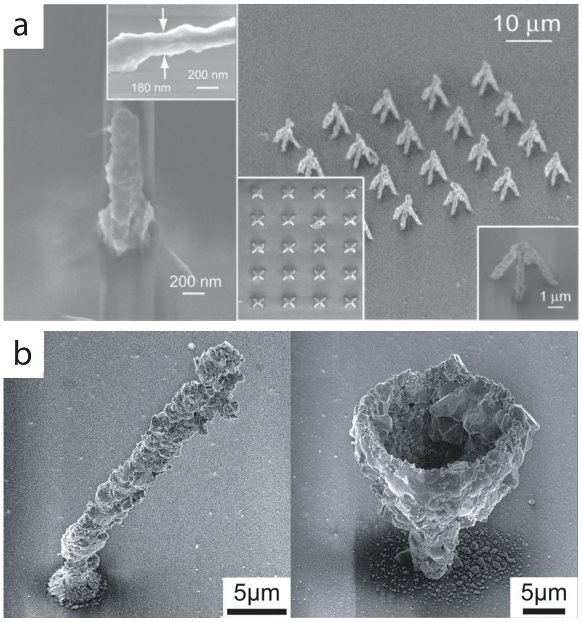

Figure 2.6: Examples of 3D silver structures fabricated by MPA. (a) SEM images of a free-standing silver pillar at an observation angle of 45 degrees and silver line pyramids at an observation angle of 45 degrees. The insets are a close up views from the side and the top. Fabricated by Cao et al. (b) SEM images of a silver tilted rod and a silver cup on a glass substrate fabricated by Ishikawa et al. Adapted from references [63] and [65].

2.2 Direct laser writing of 3D metallic structures embedded in a dielectric matrix

Several techniques have been discussed in section 2.1 that allow for nanometer patterning, but none of them have the required speed, cost, and versatility combination required for prototyping metal-dielectric nanosystems. To resolve these limitations, we develop a single-step method to fabricate disconnected 3D metallic nanostructures that are embedded in a polymer matrix. In this thesis, we present a new chemistry method to overcome previous limitations, and we fabricate high-resolution silver nanostructures in 3D using femtosecond laser direct metal writing. By utilizing nonlinear optical interactions between metal ions, chemical precursors, and femtosecond pulses, we limit the metal ion photo-reduction process to a focused spot smaller than that of the diffraction limit. This technique allows us to directly create metal patterns inside a dielectric medium. No photoinitiators or complex molecules are required for our process. Our work is further described in Chapters 4 and 5.

2.3 Conventional graphene fabrication techniques

Graphene, an emerging material, is a 2D single atomic layer of graphite. It is believed to be the thinnest and strongest material ever found; and it has massless fermions and extraordinary thermal and electrical conductivity [33,34]. Graphene is inherently a planar one-atom-thick layer, and it has been shown that the electronic structure rapidly changes with the number of layers, approaching the 3D limit of graphite at 10 layers [33, 80]. Only monolayer graphene and bilayer graphene can be considered to be zero-gap semiconductors, and for 3 or more layers, the optical spectra become increasingly complicated [32, 33, 80, 81]. Therefore, throughout this thesis, the term “2D graphite” or “reduced graphene oxide” will be used to refer to the multilayer graphene structure.

Recently, there has been an increasing amount of interest in ways of synthesizing graphene for device applications [33, 34, 51, 82–84]. Currently, there are many approaches to the synthesis of graphene and/or 2D graphite, including exfoliation of graphite and deposition and growth techniques. This section discusses the advantages and disadvantages of these various fabrication methods and concludes with an emphasis on the need for a more reliable, scalable, and cost efficient technique.

2.3.1 Liquid phase exfoliation

Liquid phase exfoliation is a cost-effective technique where graphene layers can be easily acquired from dispersing flakes of graphite in a suitable ionic liquid medium and by sonicating the solution [85–90]. Exfoliation occurs from a careful choice of solvent whose surface energy is so well matched to that of graphene that exfoliation occurs freely [88,89] and therefore no chemical reaction is involved. This decreases the chance of the flakes turning into graphene oxides and therefore allows the production of pristine graphene sheets. However since exfoliated graphene sheets are dispersed in a liquid medium, the yield concentration is usually low and the dispersed sheets need to be transferred to a desirable substrate for further use [86]. Also surfactants or dispersing agents may required to inhibit coagulation or sheet restacking due to Van der Waals forces. Careful handling is also required with the solvents [87, 90].

2.3.2 Mechanical exfoliation

(Micro-) mechanical exfoliation refers to the "scotch tape method" in which a piece of graphite is repeated peeled off using an adhesive tape [33]. This method is particularly useful for academic purposes since it generates pristine monolayer or few-layer graphene, but it only yields small samples, is impossible to pattern, and is far from commercial use. [32, 33, 83]

2.3.3 CVD & Epitaxial growth

Monolayer or few-layer graphene can be grown by CVD from carbon precursors [91–94] on metal substrates from epitaxial growth [95,96] on silicon carbide. Although large area production of graphene is possible, the costs are high and the high temperature and vacuum conditions associated with fabrication parameters cause complexity in the process. Also, although a lot of research is going to search for various substrates to grow graphene [92, 93], choice in substrates is very limited and difficulties are encountered when transferring the produced sheets to other substrates for various applications [51, 83, 86]. Although the exact quality of graphene fabricated using these methods remains unknown, epitaxial growth creates materials through crystal lattice matching and may offer better quality graphene sheets than other methods [33]. Likewise, these methods suffer from high cost and limited patternability.

2.3.4 Carbon nanotube unzipping

This method produces graphene structures by unzipping curved carbon structures such as carbon nanotubes, cones, and fullerenes through methods such as electro-oxidative chemical unzipping [97, 98], electrochemical unzipping [99], or by reactive ion etching [100]. Chemically unzipped carbon structures go through oxidation during the unzipping process and therefore have to go through a post processing reduction step [97, 98]. The growth process of the curved carbon structures are not yet fully understood, and due to limitations in size of these structures and scalability this is also not a viable method for device fabrication [33, 101].

2.3.5 Chemical reduction of graphene oxide

Graphene oxides can be made in massive amounts and through cheap and common solution-processing capabilities and are widely used as an effective route to producing graphene materials [51]. To acquire graphene oxides, first graphite oxide (a more thick, bulk form of graphene oxide) is made by using a very cheap (modified) "Hummer's" method which uses a chemical mixture of flakes of graphite, sulfuric acid (H_2SO_4), sodium nitrate ($NaNO_3$) and potassium permanganate ($KMnO_4$) [82]. Then through a variety of chemical, thermal and mechanical methods graphite oxide can be exfoliated or dispersed into single or a few layer graphene oxides [51, 82, 102].

These thin layers of graphene oxides can be used as insulating sheets or can be further reduced to graphene for electronic applications. Further reduction of graphene is achieved chemically through the use of strong reductants (such as hydrazine or sodium borohydride), thermally, or electrochemically [83]. This is a very cost effective process with no limits on the choice of substrates. Figure 2.7 shows a schematic of the whole procedure with a suggested structure of graphene oxide layer.

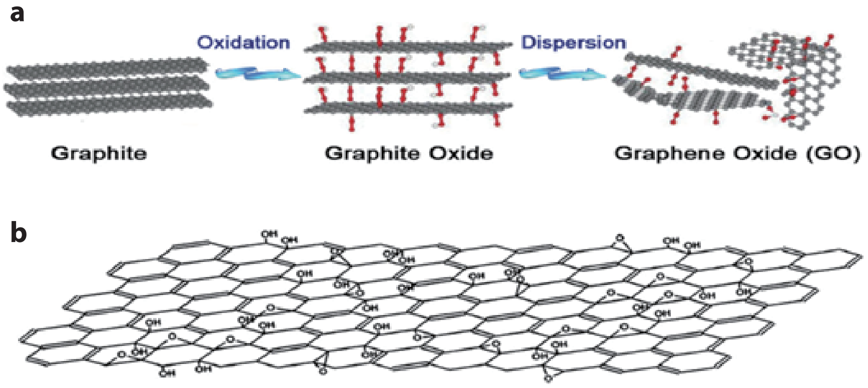

Figure 2.7: (a) A schematic describing the chemical reduction of graphene process. (b) One possible structure of a graphene oxide. Adapted from reference [51].

In addition to the fact that this is not a patterning method that can produce arbitrary patterns of graphene layers, it has some other disadvantages; despite of the extensive research, several models of graphene oxide are still being debated in the literature [83], and due to the use of harsh chemicals, substantial structural damage occurs during the reduction process [82, 102].

2.4 Direct laser writing of reduced graphene oxide structures

In recent years, in addition to thermal and chemical reduction, photoreduction of graphene oxides to fabricate graphene has emerged as an appealing process because photoreduction does not rely on either high temperature or toxic chemicals [51]. In addition to photolithographic techniques where patterned masks are used together with a broad light source, photoreduction through focused laser beams can produce patterned reduced graphene oxide (2D graphite) structures [51, 103–106]. Figure 2.8 shows some of the direct laser written structures. The advantage of this technique is that it is reliable, scalable, cost-effective, and does not require the use of any predefined patterned substrates. We extend our ultrafast laser direct writing expertise to work on graphene oxide. Most of the previous photoreduction studies utilized ultraviolet, Hg, or Xe lamps or continuous wave (CW) lasers [51, 103–105]. It is possible that these reduction mechanisms resulted from thermal effects and/or linear absorption. Only a few works were done with an ultrafast laser [51, 104, 106], which suggests the possibility that reduction of graphene oxide may occur through nonlinear interactions. By lowering the laser repetition rate down to 10kHz, we study graphene oxide reduction through nonlinear absorption.

In Chapter 6, we present our work on studying direct laser writing of 2D

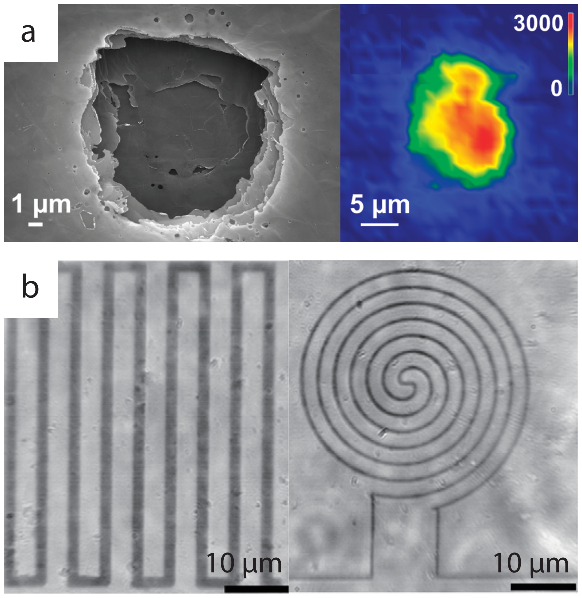

Figure 2.8: (a) SEM image of a laser reduced spot by a 532-nm CW laser (left) and a spatially resolved map of the Raman 2D band, which is a characteristic Raman signal for graphene structures (left). (b) Optical microscopy images of reduced and patterned GO films. Adapted from references [104] and [106].

graphite with various laser parameters. We perform a systematic study of the reduction process of graphene oxide to graphene by varying both the laser fluence and the repetition rate. We expect that the production of cheap graphene oxide films coupled with laser lithography may offer a preferred route to generate very large-scale graphene integrated devices in the future.

2.5 Summary

Fabrication of next-generation photonic and graphene devices requires techniques that produce patterned subwavelength features freely in 2D & 3D while spanning large volumes. The bottleneck in experimental development is due to the state of current nanofabrication techniques, which are limited in scope, resolution, or dimensions in key ways.

For photonic device fabrication, conventional lithography techniques can provide the high resolution required for applications such metamaterials but is fundamentally two-dimensional. Efforts to extend such techniques to three dimensions via layer-by-layer fabrication are typically limited by low throughput, high cost, and the difficulty of producing more than a few layers. Self-assembly techniques can produce high-quality, large volume metamaterials; however, this approach lacks 3D partternability and is very limited in the types of design that can be fabricated. As a solution to this problem, femtosecond laser-writing techniques have been steadily improving to provide high resolution fabrication of complex 3D patterns but have been mostly focused on polymer based metamaterial structures.

For graphene device fabrication, finding reliable fabrication methods is still an ongoing challenge. Exfoliation techniques can give high quality graphene sheets but are limited by very low throughput and cannot produce patterns required by devices. Chemical reduction techniques are cost-effective and scalable but generate structural and chemical defects, leading to lower quality graphene sheets.

We explore innovative ways of fabrication by combining photoreduction mechanism with an ultrafast laser direct writing process. By clever choice of chemistry, we can fabricate metallic nanostructures that are patterned and embedded in a dielectric matrix. From a systematic study with various laser parameters we achieve a more efficient reduction process of graphene oxide to graphene. More detailed explanation can be found in the following chapters.

Chapter 3

Fabrication parameters and mechanism

Ultrafast-laser micromachining allows for 3D fabrication of structures much smaller than the diffraction limited laser spot size in various media. Under a linear regime, the medium does not absorb light at the operating wavelength of the laser. However, using ultrafast pulses, we can obtain material modification or induce chemical reactions through non-linear absorption. This chapter discusses how we utilize an ultrafast laser with selected chemistry to fabricate metal-dielectric systems and 2D graphite patterned structures.

3.1 Direct laser writing of 3D metallic structures in a dielectric matrix

We analyze how various laser parameters and chemistries affect the fabrication process of 3D metallic structures in a dielectric matrix.

3.1.1 Role of the laser

Ultrafast lasers are used broadly to refer to pulsed lasers with pulse duration on the order of a picoseconds or less. Due to the short pulse duration, a very high peak power can be generated, which leads to nonlinear light-matter interactions that initiate the metal fabrication process through photoreduction.

3.1.1.1 Photoreduction by nonlinear absorption

As explained in Chapter 2, multiphoton absorption (MPA) is a process where two or more lower-energy photons are absorbed by an atom simultaneously or on a very short time scale. This allows the same effects as absorbing a single higher energy photon while the bulk of the sample remains transparent to the light source. While multiphoton absorption can initiate a polymerization reaction as in a two photon polymerization process, it can also excite an electron to be used in a chemical reduction process. A double bond is comprised of a stronger sigma (σ) bond, and a weaker pi (π) bond that allows an easy excitation of an electron from a bonding state to an anti-bonding state through light absorption. Chemical reduction is a process where an electron deficient positive ion receives electrons to turn into a neutral- or negative-charged state. By using a polymer that has plenty of double bonds, such as polyvinylpyrrolidone (PVP), lasers can initiate a process where these double bonds get excited and transfer electrons to positively charged ions in the surrounding medium. By using ultrafast lasers, such as a femtosecond laser, we can prohibit linear absorption in the bulk of PVP but induce nonlinear absorption for photoreduction only in a minimal volume, where the laser is most focused, providing temporal and spatial confinement of photons.

During the laser writing process, silver ions are reduced and form silver structures in the focal volume of the pulses. This process is limited to a small volume where the laser is most intensely focused, which allows the fabrication of structures smaller than the diffraction limit of light. Because the resin does not polymerize, degrade nor induce metal reduction through single photon absorption at the laser wavelength of 800 nm, we have full 3D access inside the bulk of the mixture. By controlling the position of the focus with a three-axis translation stage we are able to fabricate complex nanostructures in three dimensions.

To determine suitable chemistry for photoreduction through nonlinear absortption and observe initial silver formation, we measure absorbance at various wavelengths. The chemistry we choose must remain transparent at longer laser operating wavelengths for nonlinear absorption to occur within the restricted focal volume. Figure 3.1 shows absorbance vs. wavelength plots for three chemical mixtures: 1) aqueous silver nitrate ($AgNO_3$) solution (top), 2) aqueous PVP solution (middle) and 3) aqueous $AgNO_3$ and PVP solution (bottom). Several absorption bands can be observed. In the aqueous $AgNO_3$ absorbance plot, we expect an absorption band around ∼210 nm from the $4d10$ to $4d9$ transition of the Ag^+ ion [107, 108]. Additional peaks may be due to $NO_3{}^-$. We also observe a band ∼300 nm which is due to Ag_n (n≈3) clusters which acts as precursors for Ag nanoparticles [107, 109, 110]. In the aqueous PVP absorbance plot, a cluster of peaks is seen in the UV regime. The carbonyl group (C=O) in PVP has a strong absorption due to π-$\pi*$ transition at ∼254 nm and this can be excited through a multi-photon process and reduce a neighboring silver ion to a silver atom [111]. An absorbance peak around 420 nm was detected only when both silver nitrate and PVP were used. This peak is due to plasmon resonance from the silver nanoparticles and we can confirm that PVP induces photoreduction from linear absorption of UV light (in natural room lighting). Therefore by using an ultrafast laser at longer wavelengths, we can initiate a nonlinear absorption in a focal volume.

Figure 3.2 is a time progression plot of the silver nitrate & PVP solution. As time passes, the peak at ∼300 nm decreases, indicating a decrease in silver atom clusters. Instead the peak at ∼420 increases, indicating an increase in silver nanoparticle formation.

3.1.1.2 Laser fabrication parameters

During the laser exposure step, the silver ion reduction process is limited to the focal volume of the pulses and allows fabrication of silver structures smaller than the diffraction limit of light. The size of these structures is controlled by numerous laser parameters, such as the wavelength, pulse energy, repetition rate (rep rate) and total exposure time. The femtosecond laser pulse irradiation process is fundamentally dif-

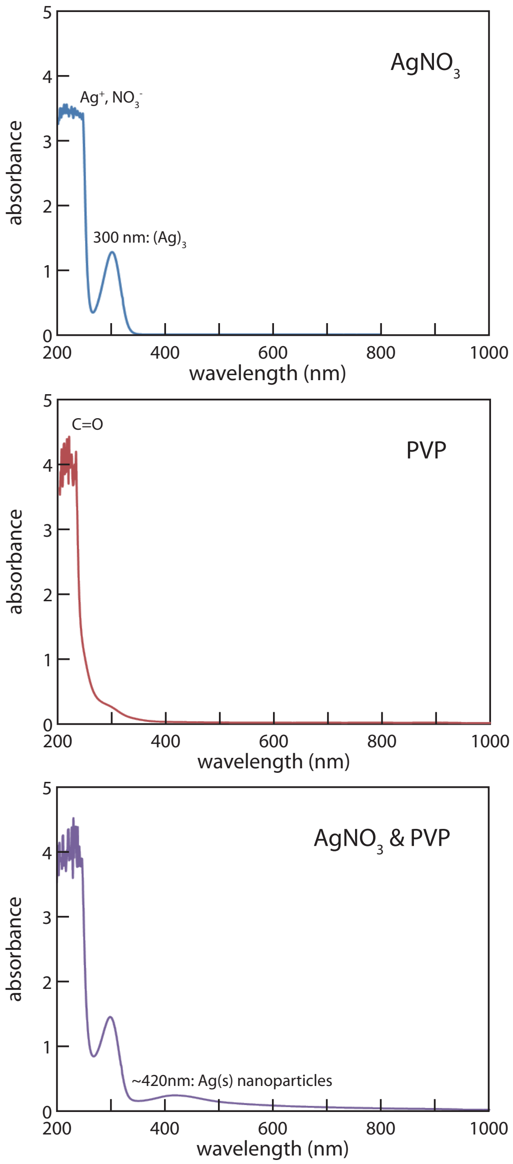

Figure 3.1: Absorbance vs. wavelength plots: (Top) 0.21g of $AgNO_3$ in 8 mL of deionized water (DI H_2O), (middle) 0.206 g of PVP in 8 mL of DI H_2O and (bottom) a mix of 0.21 g of $AgNO_3$ and 0.206 g of PVP in 8 mL of DI H_2O. All measurements were made using a Hitachi U-4100 spectrophotometer in quartz cuvets.

ferent from processes with longer pulse durations due to the timescale over which the electrons are excited [53]. Femtosecond pulses end before the electrons can thermally excite any ions and therefore heat diffusion outside the focal area is minimized [53].

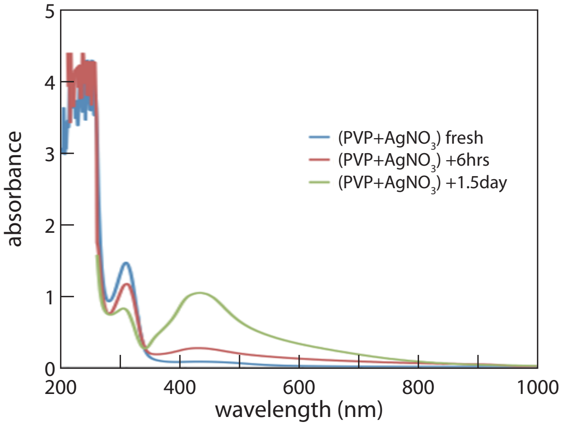

Figure 3.2: Time progression plot of absorbance vs. wavelength. As time passes, peak at ∼300 nm decreases and peak at ∼420 nm increases.

Pulse duration, rep rate and total exposure time can be modified to limit heat accumulation and thermal effects within the sample. A set of gratings can be used to modify pulse duration. Rep rate is controlled by use of Q-switches or saturable absorbers. Total exposure time can be controlled by using an acousto optical modulator (AOM) which acts like a Bragg cell to diffract the laser beam. Diffraction of the beam results in alignment or misalignment of the beam with the rest of the laser path allowing modification in the laser exposure time. By selecting dry objectives with long working distances, a thicker layer of structures can be fabricated. By selecting oil or water immersion lenses, numerical aperture (NA) can be increased to 1.45, which is beyond the theoretical maximum NA of 1 for dry objectives. This will allow a much smaller focal volume, while sacrificing the long working distance. By using a Titanium: Sapphire laser centered at 800 nm and NA of 0.8, we easily generate metal structures that are in the range of 80-150 nm and 200-300 nm depending on the chemistry. (More information in the following chapters) With a higher NA objective and a shorter wavelength laser, we expect to produce smaller features.

An additional parameter that can be controlled is the beam profile. Because multi-photon absorption occurs in a volume surrounding the intensity peak above the threshold value for nonlinear absorption, the morphology of the structure is related to the laser beam profile. We use a basic beam profile shape that can be approximated to a zeroth-order Gaussian beam. By utilizing equipments such as a spatial light modulator (SLM) that uses fourier optics and phase front engineering, it is possible to engineer the beam profile and obtain a complex beam profile. Figure 3.3 is an example of the engineered beams used to generate a 3rd order Hermite-Gaussian beam, a superimposed Laguerre-Gaussian beam, a flat top and an airy beam [112].

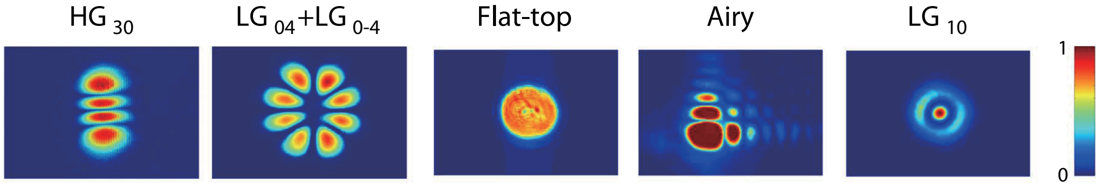

Figure 3.3: Customized spatial modes by amplitude and phase modulation. From left to right, a Hermite-Gaussian beam (n=3, m=0), a Laguerre-Gaussian (p=0, l=±4), a flat-top beam, an Airy beam and a Laguerre-Gaussian beam (p=1, l=0). The first two were generated by complex amplitude modulation and a flat-top and an Airy beam were by phase-only modulation. The last mode was created by combining amplitude and phase effects. Adapted from reference [112].

As Wloarczyk et al demonstrated in their paper, we expect the morphology of the fabricated features to reflect the engineered beam profile (Figure 3.4) [113]. Using a computer to simultaneously control the spatial light modulator, acousto-optic modulator, and translation stage position and speed, complex structures can be fabricated.

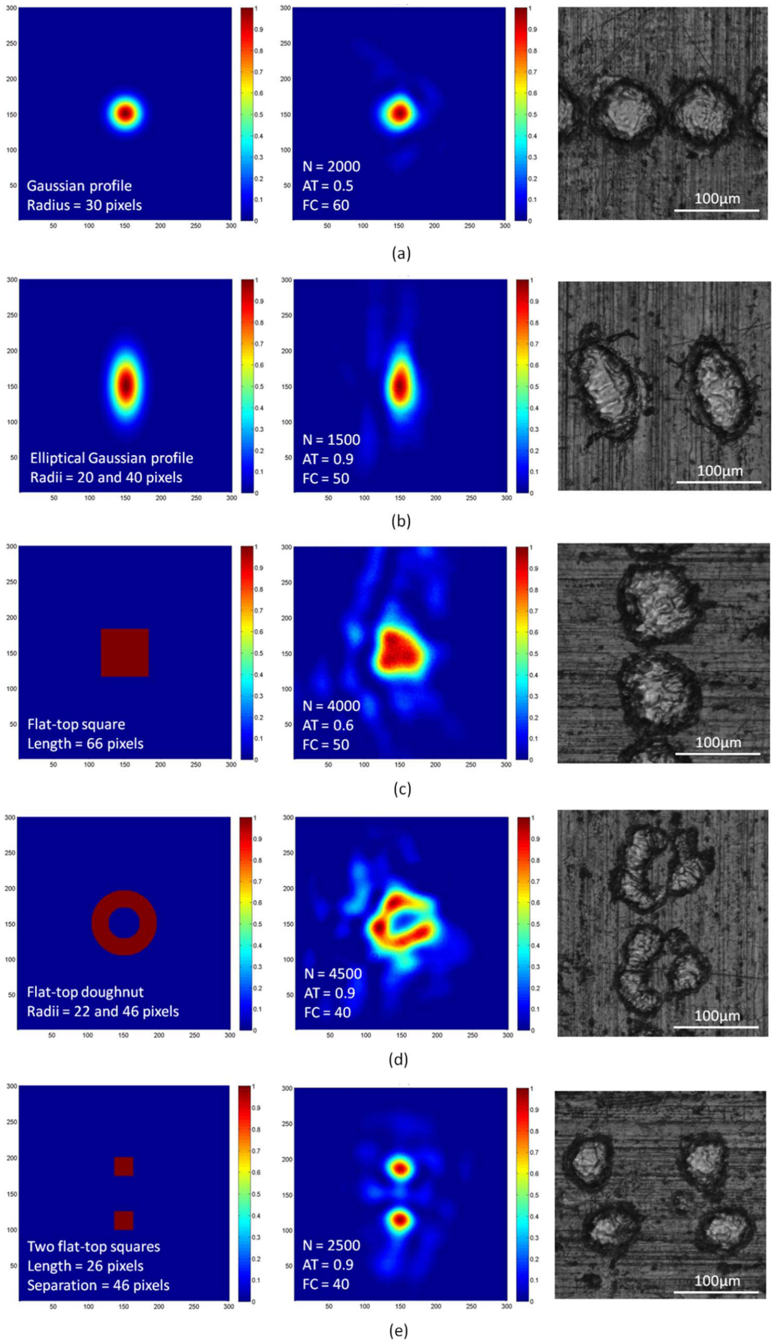

Figure 3.4: (a)-(e) Different beams obtained with a stacked array of piezoelectric deformable mirrors. Left column: target images; middle column: the best beam shaping results; right column: aluminium machined with the shaped laser beam. Adapted from reference [113].

3.2 Role of chemistry

In this section, the chemistry that affects the photo-induced metal growth will be discussed. By varying types of solvent, the concentration ratio between metal ion precursors and a polymer capping agent, as well as laser pulse parameters (section 3.1.1.2), we can demonstrate control over the morphology of the resulting metal structures.

To design an embedded 3D metal nanostructure system that meets our goals, we need to analyze the three building-block components that will comprise the fabricated system; the metal content, the supporting matrix, and the solvent that can hold all these components together.

3.2.1 Metal precursors

Metal precursors provide the necessary metal cation source for metal formation through the photoreduction process. Some examples are silver nitrate ($AgNO_3$), silver tetrafluoroborate ($AgBF_4$), silver percholate ($AgClO_4$), chloroauric acid ($HAuCl_4$) and etc. One can get a good sense of how readily the metal ion can acquire an electron by comparing the reduction potential. Reduction potential or redox potential is a measure of the tendency of chemical species to gain electrons. The more positive the potential is the more likely that ion will be reduced. Table 3.1 is a table of reduction potential for common metal salts [114].

Gold and Silver ions have a large reduction potential and are easier to reduce compared to other metal ions. This serves as one of the reasons why we chose silver (and gold) to test out our method. We mainly focus on the silver writing method

Table 3.1: Reduction potential for common metal salts (with respect to hydrogen). Adapted from reference [114].

Reaction	E^o (volts)
$Au^+ + e^- \rightarrow Au$	+1.692
$Au^{3+} + 3e^- \rightarrow Au$	+1.498
$Ag^+ + e^- \rightarrow Ag$	+0.7996
$Cu^+ + e^- \rightarrow Cu$	+0.521
$Cu^{2+} + 2e^- \rightarrow Cu$	+0.3419
$2H^+ + 2e^- \rightarrow H_2$	+0.0000
$Al^{3+} + 3e^- \rightarrow Al$	-1.662

due to future metamaterial applications in the visible wavelength range. Less loss is expected from silver structures (than gold) in the optical regime [115].

3.2.2 Solvents

In addition to acting as a medium to dissolve the metal salts in, solvents give the appropriate viscosity, rate of heat dissipation, and can provide additional chemical processes to either enhance or reduce metal reduction. Therefore understanding the role of solvents is crucial.

Conventionally a polyol process has been used to fabricate silver nanoparticles by chemical reduction [62, 65, 116, 117]. Polyol process refers to a chemistry where alcohols are used as a solvent to aid the metal ion reduction process. In our method, we use ethanol and deionized (DI) water as main solvents. Water has a very high polarity and is the most effective and safest solvent available to dissolve ionic salts. Other researchers who have tried to direct laser write metal structures chose a mix of ethanol and water [62, 65] or just water as solvents [64]. To investigate what effect ethanol has in the metal reduction process, absorptance spectra were taken for two different samples with $AgNO_3$, PVP and one with only DI H_2O as the solvent and the other with ethanol and DI H_2O. The absorptance plot (Figure 3.5) shows a larger amount of silver nanoparticle formation for the solution that included ethanol. Absorptance peak around 0.42 μm is due to silver nanoparticle plasmon resonance and the sudden increase near 0.3 μm is from UV absorbance of the cuvet.

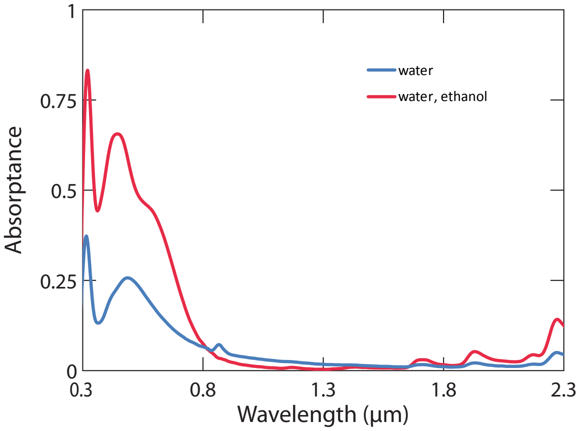

Figure 3.5: Absorptance vs. wavelength plot of water and water with ethanol. Larger absorption peak is detected by choosing a mix of water and ethanol as solvent.

There are two ways that ethanol (alcohols) could be playing a role in this reaction. First is that it serves as a reducing agent (to reduce silver) by oxidizing into aldehydes (-CHO) or carboxylic acids (-COOH). Second is that it acts as a catalyst by lowering the reaction energy barrier. In the first case, we expect formation of a byproduct, such as acetaldehyde and/or acetic acid, from the reaction caused by ethanol. By doing a proton NMR (^{1}H-NMR) on the product solution we can check if the reactant ethanol has oxidized to an aldehyde or a carboxylic acid. ^{1}H-NMR can be used in detecting minute chemical compositions by determining the structure of the molecules [118, 119]. It is one application of nuclear magnetic resonance (NMR) spectroscopy that measures chemical shifts (δ) with respect to hydrogen. Chemical shift is measured by applying an external magnetic field and letting the spins of magnetic nuclei in hydrogen orient (either in parallel or antiparallel) to the external field. Then when the oriented nuclei are irradiated with the proper frequency of electromagnetic radiation, energy absorption occurs and the lower-energy state spin flips to the higher energy state. This energy is shown as chemical shift. Delta (δ) is defined as the resonance frequency (Hz) difference between the sample chemical and the calibration chemical, over the spectrometer frequency [118, 119]. Therefore regardless of the various types of spectrometers with varying magnetic fields, one can get a constant delta value that is specific to each hydrogen. Deuteriochloroform ($CDCl_3$) was used as a diluting solvent for this measurement. Figure 3.6 shows results of the ^{1}H NMR on a solution with ethanol, DI water, silver nitrate and with and without the polymer PVP. (More information on PVP will be explained in the following section. PVP is another crucial component to our 3D fabrication chemistry)

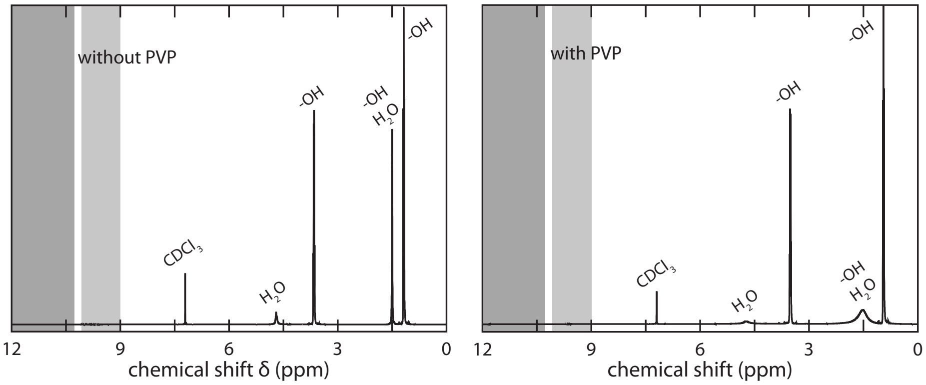

Figure 3.6: ^{1}H-NMR results from $AgNO_3$ and DI H_2O mix (a) without PVP and (b) with PVP.

The aldehyde chemical shift peak is around 9-10 ppm region and the carboxylic chemical shift peak is around 10-13 ppm. [118,119] No signs of aldehyde nor carboxyl formation was observed and therefore we can conclude that ethanol does not undergo chemical reactions with silver nitrate but instead provides a catalytic pathway in the silver ion reduction process [1].

Therefore if the fabrication process requires initial silver nanoparticle seeds, then ethanol can be added to speed up the initial silver ion reduction process. This is valuable to our 2D silver nanocrystal fabrication technique that will be discussed in Chapter 4. For 3D fabrication, a more stable and slower silver reduction method needs to be utilized in order to prohibit unnecessary growth in the rest of the bulk matrix. Hence, we omit ethanol in our chemistry for 3D fabrication which will be discussed in Chapter 5. In addition to omitting the ethanol, nitric acid (HNO_3) can be added to further reduce the effect of the -OH group which may also come from H_2O. An increase in the $[H^+]$ concentration from HNO_3 leads to a decrease in the $[OH^-]$ concentration, due to constant K_w [2]. Figure 3.7 shows the color differences between solutions prepared with and without HNO_3. As silver nanoparticles are formed, color changes from transparent to yellow and to darker brown. Solutions with HNO_3 remain transparent compared to the ones without HNO_3. Solutions on the left were prepared using PVP as our polymer choice, and gelatin on the right. More information on our choice of gelatin can be found in the following section and in Chapter 5.

To further control the role of solvents, we oven bake or air-dry the samples at

---

[1] To analyze the catalyst mechanism further one can measure the reaction time at various concentrations to get exponents and the reaction constant of a reaction: $[Ag^+]^a+[C_2H_5OH]^b \rightarrow [Ag]^c+[CH_3CHO]^d$.This won't be discussed in this thesis.

[2] Dissociation constant of water (K_w) $=[H^+][OH^-]=10^{-14}$

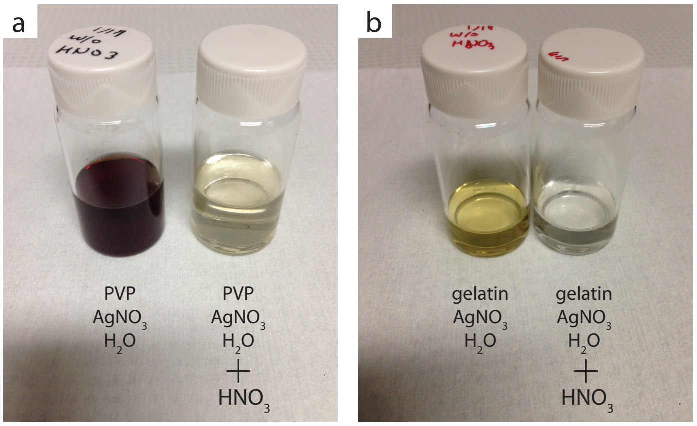

Figure 3.7: Pictures to compare solutoins with and without HNO_3. (a) Picture of PVP base chemistry and (b) Picture of gelatin base chemistry.

the end of the sample preparation procedure. This prevents the sample from flowing off the substrate during the laser writing process and also restricts movement of ions from freely participating in the photoreduction process. During laser exposure, only a limited volume in the focal area can be heated up to allow a flow of Ag^+ to attach to silver nanoparticle seeds and grow into larger structures.

3.2.3 Polymers

In addition to initiating the photoreduction reaction by absorbing nonlinearly and therefore act as an electron donor, polymers are also used to provide the supporting matrix and serve as a capping agent. There exist many polymers such as polymethylmethacrylate, polyester, polystyrene, polyvinyl alcohol, polyvinylpyrrolidone, polylactic acid, polyacetate and etc. These polymers can be a durable supporting matrix, however many of these do not dissolve in water which is crucial in dissolving metal salt precursors. Therefore, the chosen polymer must satisfy these criteria; one, it should dissolve in water (one can use toxic chemical solvents but this is not desired for safety reasons and handling of the sample during the fabrication process). Two, it should be transparent to the laser source (see absorption graph of PVP in H_2O (Figure 3.1)) and lastly, it should have electron rich groups such as carbonyl (C=O) groups (or something equivalent) to provide electrons. One of the reasons why we can successfully fabricate 3D structures that are embedded in a dielectric matrix is by this careful choice of our polymer. Since there was no need to remove the unreacted monomer or the polymer matrix, we can leave the fabricated 3D silver nanostructures inside the supporting polymer matrix. Unlike a TPP direct laser writing process that uses monomers (refer to Chapter 2), our technique uses PVP of molecular weight 58,000 g as a supporting matrix to fabricate silver structures which eliminates the need for a polymerization process. PVP satisfies the above three criteria. It dissolves readily in water, is transparent to 800 nm and has many carbonyl groups for photoreduction to occur. Figure 3.8 shows one repeating unit of the PVP molecular structure.

Figure 3.8: PVP molecular structure (n is approximately 570 for MW of 58,000 g).

Fourier transform infrared spectroscopy (FTIR) analysis has shown that peak shiftings occur at peaks corresponding to C-N and C=O bonds which is attributed to bonding via partial donation of lone pair electrons from nitrogen and oxygen in PVP to vacant orbitals of Ag [120–122]. This confirms the strong interactions of embedded Ag nanoparticles with N and O atoms of C-N and C=O bonds in PVP. Also, PVP was shown to preferentially adhere to the {100} facets which leads to addition of silver atoms to the {111} facets and therefore silver growth in the <111> direction [116,117]. By utilizing these characteristics, various shapes of silver nanostructures can be grown by controlling the ratio of PVP and silver nitrate [116,117]. Figure 3.9(a) shows wet-chemistry fabricated silver nanocubes with a silver nitrate concentration of 0.2 M and PVP to silver nitrate ratio of 1.5. Decreasing the concentration of silver nitrate results in insufficient encapsulation of all 100 facets and leads to growth of silver nanowires as in Figure 3.9(b) and with very high concentrations of PVP, silver nanospheres can be obtained as in Figure 3.9(c).

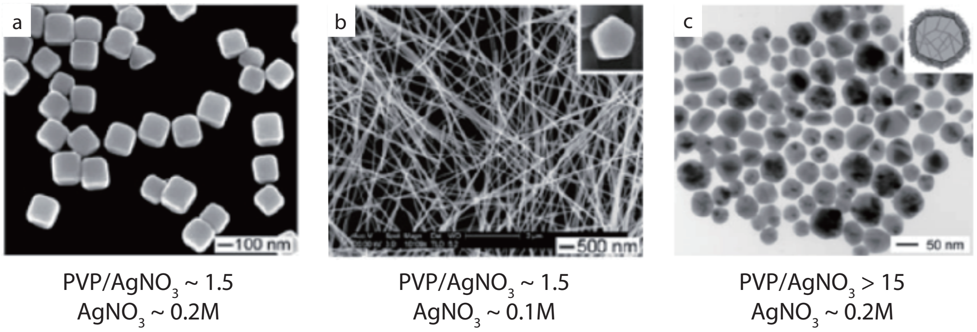

Figure 3.9: Silver nanocubes, wires and spheres fabricated by controlling the ratio of PVP/AgNO$_3$. Adapted from reference [117].

This PVP adsorption due to electron donation from numerous C-N and C=O bonds is the key to fabricating high resolution silver nanostructures that will be presented in Chapter 5. Chapter 5 will also discuss fabrication of 3D structures with gelatin as the supporting polymer matrix. In addition to the advantages PVP has, gelatin is composed of longer molecular chains which provide more effective size control of silver and its hydrogel properties allow for a streachable matrix.

3.2.4 Additives

Other chemicals such as surfactants, stabilizing agents, reducing agents, photosensitive agents, dyes and nanoseed particles can be added to manipulate the chemistry. For example, Cao et al. [63] were able to reduce the size of fabricated silver structures by adding extra surfactant, n-decanoylsarcosine sodium (NDSS). Ishikawa et al. [65] were also able to reduce the feature size by adding a two-photon sensitive dye, Cumarin 400. Sun et al. [123] added sodium citrate, a commonly used charge stabilizing agent for Ag nanoparticles in aqueous solutions, to transform silver nanoparticles into nanotriangles and nanobelts.

To devise a simple and cost-effective fabrication method, we aimed to develop a fabrication method that doesn't require extra additives.

3.3 Direct laser writing of reduced graphene structures

Ultrafast pulses, as mentioned in section 3.1.1.1, can induce material modification or chemical reactions through non-linear absorption. We study direct laser writing of 2D graphite patterns through photoreduction of graphene oxide films. Although producing graphene-like materials through photoreduction of graphene oxide has been verified [51, 103–106], finding reliable fabrication methods and discovering the true chemical structure of graphene oxide and many of graphene derivatives is still an ongoing challenge [83]. Additionally the reduction mechanism remains unclear [82]. Most of the photoreduction of graphene oxide (GO) structures has been demonstrated by using light sources such as UV, Hg, Xe lamps, and CW lasers [51, 103–105]. It is very likely that these reduction mechanisms resulted from thermal effects and/or linear absorption. Only a few works were done with an ultrafast laser [51, 104, 106] which also suggests the possibility that reduction of graphene oxide may occur through nonlinear interactions. However, previous studies did not confirm that the process was nonlinear and did not decouple thermal and non-thermal effects. By testing various repetition rates and pulse durations and by lowering the laser repetition rate down to 10 kHz, we study the possibility of graphene oxide reduction through purely nonlinear effects. (Refer to section 3.1.1.2 for more information on the effects of various laser setup parameters.) Among the many possible GO structures, a few proposed structures contain several C=O bonds [124, 125]. Figure 3.10 shows one such GO structure proposed by Dékány and coworkers. We hypothesize that we can produce 2D graphite by only allowing nonlinear photoreduction processes in chemical groups such as C=O which will result in a similar process used for direct laser writing metal structures in section 3.1.

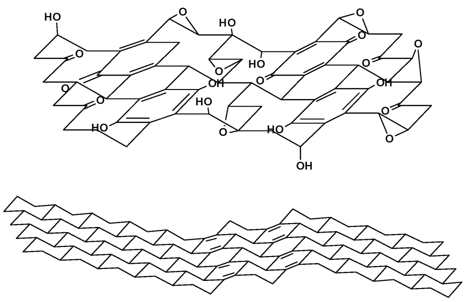

Figure 3.10: Structure of GO proposed by Dékány and coworkers. Adapted from reference [124].

Figure 3.11 is a schematic of the GO reduction process through ultrafast laser photoreduction. GO has similar structure to graphite (many stacked layers of graphene) with much wider spacing (6-12 Å) between the layers due to its hygroscopic nature [82, 126]. We expect a much thinner layer of 2D graphite in the laser irradiated areas from the reduction of the functional groups between the graphene layers.

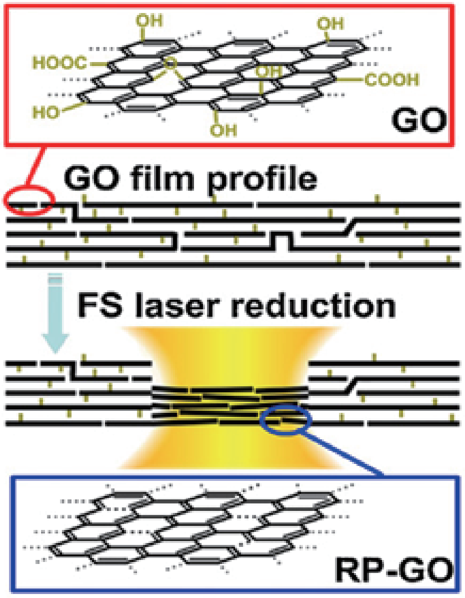

Figure 3.11: Schematic of ultrafast laser direct writing of GO. Adapted from reference [106].

We hypothesize that compared to the reduction process that was derived from both thermal and non-thermal components, the reduced patterns written using only non-thermal mechanism may produce higher quality structures. By using various laser fluence and repetition rates to decouple thermal and non-thermal mechanisms, we investigate the possibility of achieving a high degree of flexibility and control in the fabrication of graphene layers. This work is presented in Chapter 6.

3.4 Summary

We use an ultrafast laser to induce photoreduction of C=O bonds in polymers and graphene oxide films. Ultrafast lasers restrict the nonlinear interaction between the laser and the materials to the focal volume which results in fabricated structures that are smaller than the diffraction limit of light. For direct laser writing of metal structures we combine a metal precursor, a polymer and a solvent and choose an appropriate laser wavelength that the bulk of the sample is transparent to and a repetition rate that causes minimal heat accumulation. When choosing a polymer, electron donating properties, optical characteristics and its solubility in water should be taken into account to consider whether it is suitable for supporting embedded structures and for allowing fabrication of high resolution structures. We can further control the speed of the reaction by hardening the sample solution to restrict the movement of ions, or by adding additional solvent such as alcohols to provide a faster catalytic pathway of reduction. Figure 3.12 is a transmittance vs. wavelength plot of various chemistries to fabricate metal structures. (We also tested ethylene glycol (EG)) as a solvent to confirm the effects of -OH functional groups. EG has two -OH groups rather than one, as in ethanol (EtOH).) This figure summarizes the different chemistries. The absorption at ∼420 nm is due to silver nanoparticle formation. Without the use of ultrafast lasers, addition of PVP reduces silver ions from linear absorption of UV. Addition of alcohols causes a faster reduction of silver ions. (A more broad absorption peak with use of EG indicates a broader distribution of silver nanoparticle formation.)

By optimizing the chemistry and laser parameters, we fabricate 2D silver crystals

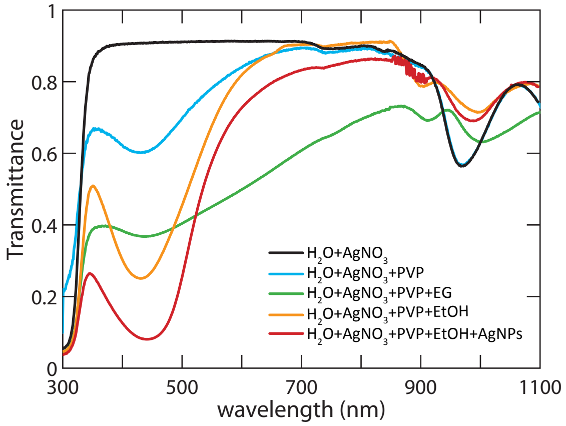

Figure 3.12: Transmittance vs. wavelength plot of various chemistries for DLW of metal structures. Each mixture was measured in its solution form in a cuvett rather than as thin films to magnify the absorption bands.

and 3D silver nanostructures that can be embedded in a matrix. These works are presented in chapters 4 and 5 respectively. Although finding out the structure of graphene derivatives and the reduction mechanism of GO is still a challenging issue, we aim to gain further understanding by decoupling thermal and non-thermal aspects of the reduction mechanism. Our work on fabricating 2D graphite structures is presented in Chapter 6.

Chapter 4

Direct laser writing of 2D metal systems in a polymer matrix

In this chapter, we report the fabrication of silver nanoprisms, especially hexagonal silver nanocrystals through irradiation with focused femtosecond laser pulses. A nonlinear optical interaction between femtosecond laser pulses and a polyvinylpyrrolidone film doped with silver nitrate leads to the growth of silver nanoprism crystals in irradiated volumes. The nanoprisms have hexagonal bases hundreds of nanometers in size and the crystal growth occurs over exposure times of less than 1 ms (8 orders of magnitude faster than traditional chemistry techniques). Electron backscatter diffraction analysis shows that these nanoprisms are single crystalline. The fabrication method combines advantages from wet chemistry and femtosecond laser direct-writing to grow silver crystals in targeted locations. The results may offer a new approach to growing silver crystals for plasmonic devices.

4.1 Crystals

Compared to bulk silver, nanocrystals have unique characteristics [127–129] that make them useful for various applications, such as catalysis, biomedical sensing and electronics [56, 130–135]. A variety of techniques have been developed to fabricate silver nanoparticles, including laser ablation, microwave, photochemical, sonochemical, electrochemical and wet chemistry methods [116, 117, 136–143]. Among these techniques, wet chemistry is popular for growing high-quality silver crystals in a multitude of shapes, including pyramids, bipyramids, cubes, triangular prisms, hexagonal prisms, and nanowires [116,117,142,143]. However, unlike top-down methods these techniques lack patternability. Conversely, femtosecond laser direct-writing methods are used to grow silver in engineered patterns in two and three dimensions [62–65, 68, 144, 145]. However, they lead to silver structures that are composed of silver nanoparticle agglomerations with void, polymer, or multiple domain inclusions [144]. We present a method that leads to hexagonal silver nanocrystal growth through irradiation with focused femtosecond laser pulses. The technique combines advantages from traditional wet chemistry and femtosecond laser direct writing: high-quality silver crystals and targeted growth with high speed.

4.1.1 Materials & Method

4.1.1.1 Materials

Silver nitrate ($AgNO_3$) and ethanol was purchased from Sigma-Aldrich. Polyvinylpyrrolidone (PVP) with an average molecular weight of 58,000 g was chosen for this method and was purchased from Alfa Aesar. Mercapto propyl trimethoxy silane (MPTS) was purchased from Alfa Aesar. Deionized water was used. Regular 25 × 75mm plain, precleaned microscope glass slides were purchased from VWR and were cleaved into a third to make 25 × 25 mm glass substrates for sample preparation. For samples to analyze under the SEM, 25 × 25 mm indium tin oxide (ITO) glass slides purchased from Delta Technologies, Limited were used as substrates. Sheet resistance (RS) of 4-10 W/sq was selected to minimize charging effects under SEM.

4.1.1.2 Method

Sample preparation

To fabricate the nanocrystals we use a mixture of PVP, $AgNO_3$, ethanol, and water. We first prepare a solution by dissolving 0.25 g of PVP in 10 mL ethanol at room temperature. In a separate vial, we dissolve 0.4 g of $AgNO_3$ in 2 mL of deionized water. Once both mixtures are dissolved, we add them together and stir for 25 min. at room temperature. Next, we spin-coat the prepared solution onto a glass slide (1000 rpm for 30 s.). We use a glass slide coated with a thin 20-nm layer of indium tin oxide (ITO) that was oxygen plasma treated and silanized with MPTS. Lastly, the sample is baked in an oven for 25 min. at 110 °C. These steps are done in a room filtered of ultraviolet light to minimize unnecessary silver nanoparticle formation. The resulting sample consists of a thin polymer film doped with silver ions on a glass substrate. To only acquire the fabricated silver structures (without the un-irradiated polymer layer) or to make samples for SEM analysis, one extra step is required. After irradiation, the polymer film is removed with ethanol, leaving behind the silver nanostructures on the glass substrate.

Laser fabrication

We use a Ti:sapphire laser centered at 795 nm with an 11-MHz repetition rate, and 300-fs pulse length for the irradiation process. See Figure 4.1 for a schematic of the set-up. An objective with a numerical aperture (NA) of 0.8 focuses the pulses into the sample. The exposure is controlled by an acousto-optic modulator to produce 100$\sim$800 μs exposure windows during sample irradiation. Appropriate neutral density filters are selected to obtain 3$\sim$8 nJ pulses after the objective. A high-precision Aerotech 3-axis translation stage selects the region to be exposed and is translated at $\sim$100 μm/s for fabrication. The laser exposure is limited to individual voxels inside the PVP film, near the glass-polymer interface. The laser focal diameter is approximately 1 μm (full-width half-max). At the focus, nonlinear light-matter interactions induce metal-ion photoreduction processes in a volume smaller than the diffraction-limited focal spot, initiating silver nanocrystal growth. The fabrication process is monitored in real time by attaching a CCD camera that utilizes transmitted light with a video screen.

Characterization

An optical microscopy was carried out for real-time monitoring of the fabrication process and post-fabrication characterization of structure dimensions. Scanning electron microscopy (SEM), energy dispersive spectrometer (EDS) and electron back scatter diffraction (EBSD) measurements were performed in Zeiss ULTRA and SUPRA 55VP microscopes, using in-lens, EDAX and EBSD detectors. Optical measurements

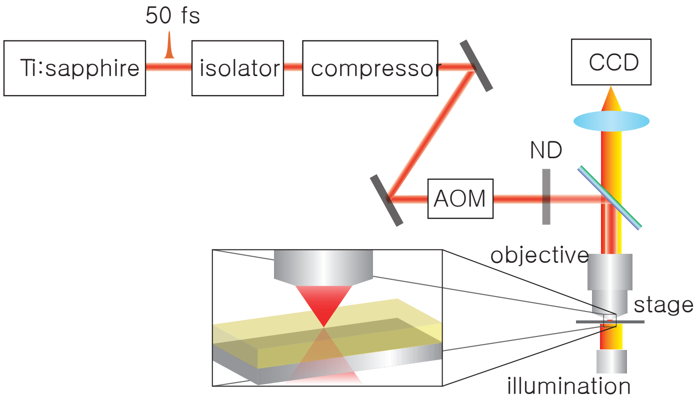

Figure 4.1: Schematic of the fabrication process. A microscope objective (NA 0.8) focuses laser pulses from an 11-MHz ultrafast Ti:sapphire laser system inside a doped polymer sample. The microscope objective also provides in-situ imaging. A high-precision and long-travel three-axis translation stage scans the sample in the x-, y- and z-directions while an acousto-optic modulator shutters laser pulses to control exposure. The result is a direct-written dielectric-embedded silver structure in 3D.

on doped films (prior to laser exposure) were made with Hitachi U-4100 spectrophotometer and J.A.Woollam V VASE-32 spectroscopic ellipsometer.

4.1.1.3 Silanization

This section describes the role and the importance of using a silane for 2D fabrication, especially like in our method when it involves a washing step. Silanes (sometimes named as coupling agents) have been used widely in research and in industry for many different purposes, such as for adhesion of biological and chemical materials to various substrates, treating the surface to make it more hydrophobic or hydrophilic, for coatings, and etc [146–149]. In our experiments silane is used to treat the substrate previous to depositing the sample to enhance adhesion between the laser fabricated structures and the substrate. Figure 4.2 [148] is a schematic of how silanes work. Silanes are typically comprised of a hydrolysable group, Si and a functional group.

Hydrolysable groups are usually alkoxy (RO-) groups such as methoxy (CH_3O-) and ethoxy groups (CH_3CH_2O-). By hydrolysis (addition of water) and condensation (subtraction of water), the hydrolysable groups get modified to have (-OH) endings. When these endings come in contact with a plasma treated glass substrate that is free of carbon residue and has dangling -OH bonds, hydrogen bonding and condensation occur that lead to a monolayer of silane adhered to the glass substrate with dangling functional groups on the other end. It is these functional groups that help adhesion of structures to the substrate. Initially, we used acryloxy-propyl-trimethoxy silane (APMS) as our silanizing agent that was bought from Gelest, Inc. Figure 4.3 shows the long functional group of APMS. Although the electronegative oxygen atoms are present, the long length of the carbon backbone chain weakens this effect. By choosing a silane with a functional group that has a stronger affinity for electron positive elements or metallic components, we are able to dramatically enhance the adhesion properties of our silver structures to the glass substrate. For our experiments, we choose mercapto propyl trimethoxy silane (MPTS) that was purchased from Alfa Aesar. Figure 4.3 shows the sulfuric functional group of MPTS.

4.1.2 Results & Discussion

4.1.2.1 Crystal structure characterization

We observe crystal growth under a variety of experimental conditions Figure 4.4. Several factors such as pulse energy, exposure time, laser focus position and laser stability affect the crystal growth, Figure 4.4(a) and Figure 4.4(b) show scanning electron microscopy (SEM) images of laser grown crystals that are larger than 2 μm.

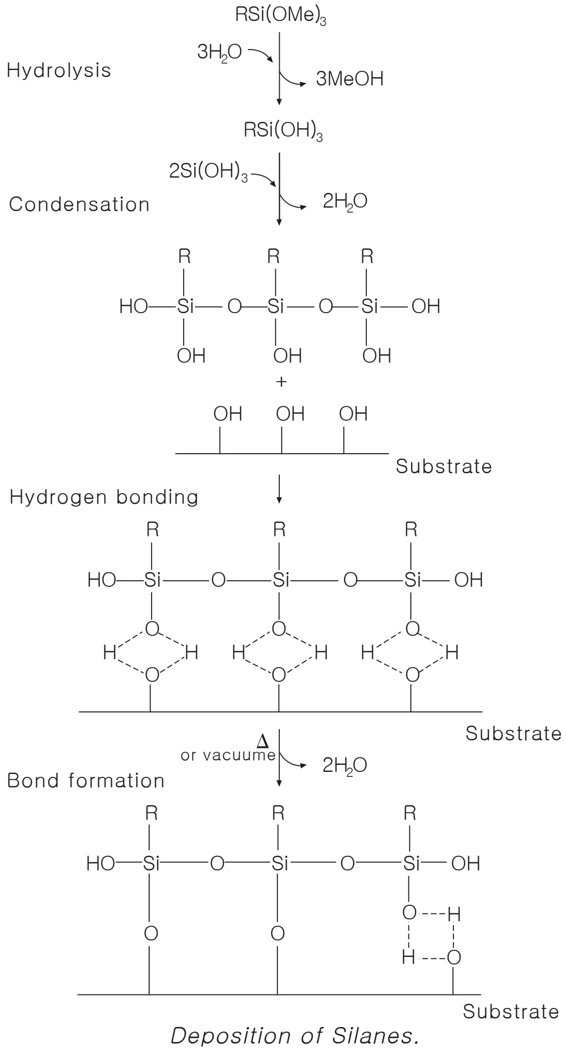

Figure 4.2: Schematic of a silanization process [148].

a Acryloxy propyl trimethoxy silane (APMS)

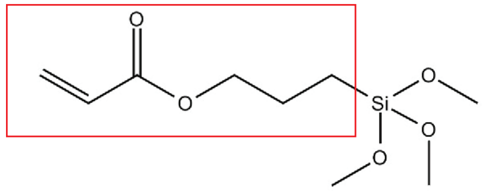

b Mercapto propyl trimethoxy silane (MPTS)

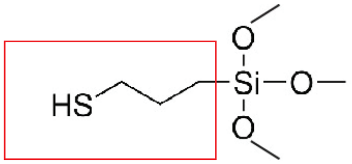

Figure 4.3: Molecular diagram of an APMS and MPTS. Red box indicates functional groups.

These large crystals tend to be washed away more easily than the smaller ones and are found next to the irradiated laser-spots. Figure 4.4(c) shows an SEM image of a 900-nm crystal grown with a total exposure time of 100 μs and 4.1 nJ per pulse; Figure 4.4(d) shows an SEM image of a 500-nm crystal grown with an exposure of 800 μs and 1.5 nJ per pulse. Crystals in figure 4.4(c) and 4.4(d) are found right at the laser spots. We also observe crystal growth with irradiation from a 11-MHz, 1050-nm laser with pulses of 270-fs duration and an average laser power of 80 mW (Figures 4.4(e) and 4.4(f)). Despite variations in these conditions, the vast majority of crystals grown through this femtosecond laser technique are hexagonally shaped.

Figure 4.5(a) shows an SEM image of a nanocrystal grown at an exposure of 800 μs and its corresponding energy dispersion x-ray spectroscopy (EDS) map of silver element (Figure 4.5(b)). EDS gives an elemental distribution map in the electron image. The EDS elemental map and the spectrum (Figure 4.5(c)) confirm that the

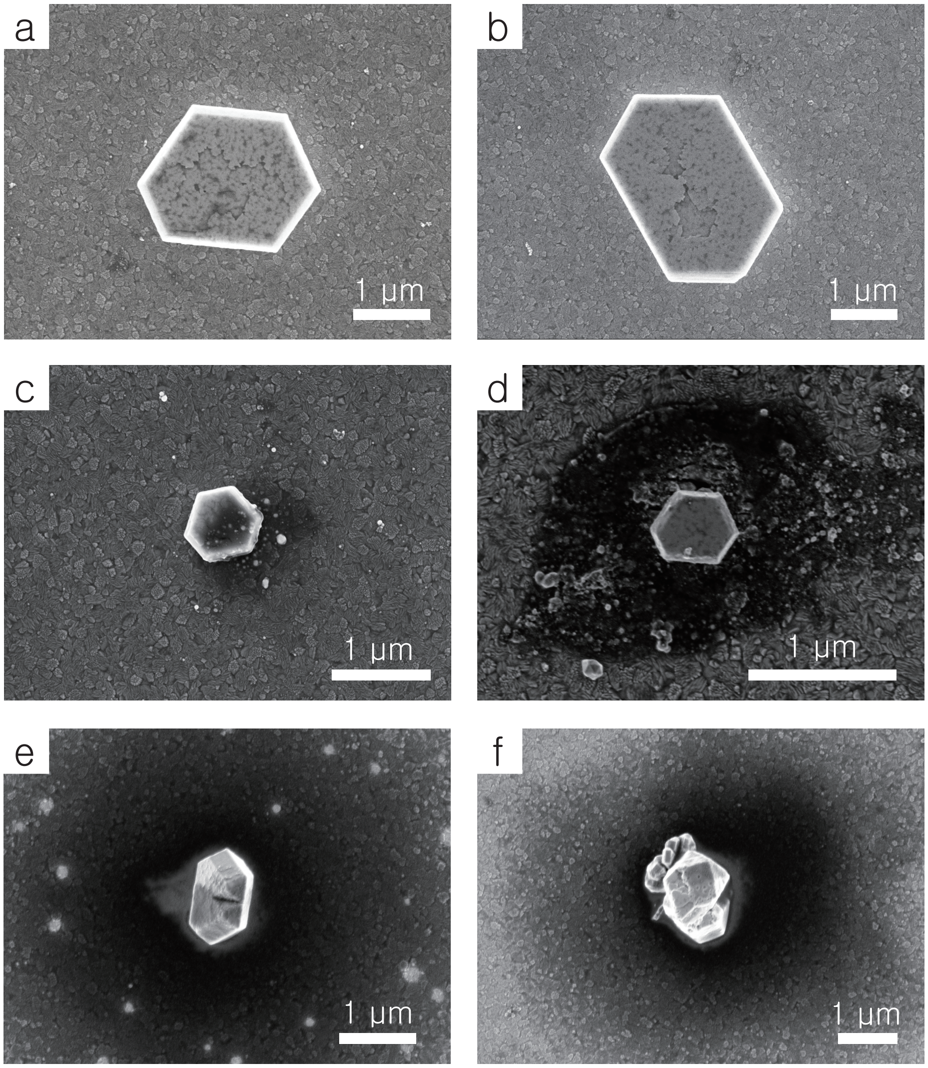

Figure 4.4: SEM images of various sized hexagonal crystals. (a) & (b) Crystals that are larger than 2 μm found near laser irradiated spots (c) A 900-nm crystal grown with a total exposure time of 100 μs and 4.1 nJ per pulse; (d) A 500-nm crystal grown with an exposure of 800 μs and 1.5 nJ per pulse. (e) & (f) Crystals with irradiation from a 11-MHz, 1050-nm laser with pulses of 270-fs duration and an average laser power of 80 mW.

nanocrystal is composed of silver. The Si-peak is from the glass substrate underneath and In-peak is from the ITO coating on the glass substrate.

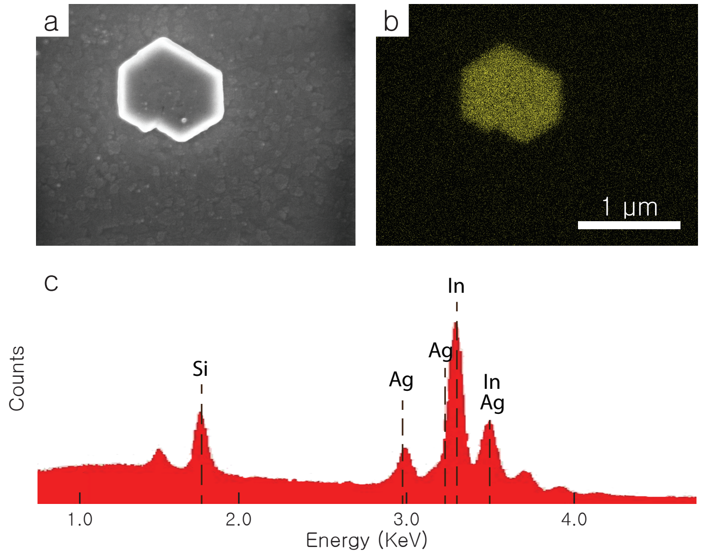

Figure 4.5: (a) shows an SEM image of a nanocrystal grown at an exposure of 800 μs and its corresponding energy dispersion x-ray spectroscopy (EDS) map of silver element (b). EDS gives an elemental distribution map in the electron image. The EDS elemental map and the spectrum (c) confirm that the nanocrystal is composed of silver. The Si-peak is from the glass substrate underneath and In-peak is from the ITO coating on the glass substrate.

We further characterized the crystals through electron backscatter diffraction (EBSD) measurements, which provide information on the orientation and crystalline structure of a material. EBSD is a fast reliable diffraction technique applicable to most crystalline materials for obtaining microstructural and microtextural information. It can provide maps of grain orientation and phase distribution, plots of orientation (pole figures), grain boundaries and crystallographic texture. These maps in EBSD are created by colored-map pixels or boundaries between pixels based on the data recorded from the probing area. The data gathers properties of quality, phase, orientation, grain boundaries, special grain boundaries, and texture-related components and produce a color or a brightness [150]. Figure 4.6 shows EBSD measurements which indicate that the probed crystal has a single crystalline silver lattice structure. Figure 4.6(a) is an SEM image of the hexagonal silver crystal and the area that was probed. Figure 4.6(b) is an EBSD map that shows uniform color and brightness, and therefore uniform grain orientation and phase distribution with no grain boundary. Figure 4.6(d) shows the crystallographic orientation of the fabricated silver nanocrystal. The (100) pole plot in Figure 4.6(c) represents a stereographic projection of the crystallographic directions present in the grains that make up the material. The directions plotted are the stereographic projection of crystal directions parallel to either the normal direction (ND), rolling direction (RD) or transverse direction (TD) in the sample. All individual point orientation measurements from the sample are shown together as three closely packed clusters of points on the pole figure representing the (100), (010) and (001) planes of the sample. These results indicate that probed portions of the silver structure are single-crystal and higher quality than silver grown through previously reported femtosecond laser techniques [62–65, 68, 144, 145]. Through EDS and EBSD analysis, we conclude that under appropriate conditions, the femtosecond-laser direct metal writing leads to single-crystal nanoparticle growth.

During fabrication, in-situ optical imaging shows that patterned samples have silver growth at close to 100 % of irradiation spots. However, after irradiation, due to the degrading nature of the polymer film prepared with this chemistry method, the film has to be dissolved with water or ethanol for sample analysis, leaving behind only those silver nanostructures strongly adhered to the glass substrate (Figure 4.7).

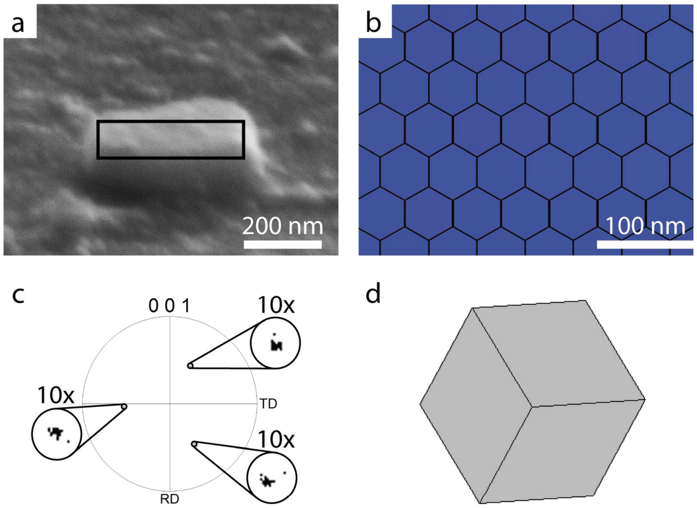

Figure 4.6: SEM image of a silver 400-nm nanocrystal and corresponding EBSD data showing single crystal structure. (a) SEM image taken from a 70° angle; outline shows the area mapped with EBSD. (b) The honeycomb contour in the EBSD map outlines the individually probed pixels; the color uniformity is indicative of single crystal orientation. (c) The (001) pole figure further highlights single crystal orientation; the insets show a 10× close-up. RD refers to sample rolling direction and TD refers to transverse direction. The silver crystal orientation is shown in (d), where the substrate is in the plane of the page.

Scanning electron microscopy (SEM) image analysis reveals the yield of silver adhered to irradiation sites after the washing step is 4.4 %. From this yield, 45 % are crystals with hexagonal shaped bases (6 facets with 120° internal angles), 21 % are partially ablated or cracked hexagonal crystals, 15 % are crystals with hexagonal-like bases (which have small deformations, or greater than 6 facets, with additional facets positioned with 120° or -120° internal angles), and 12 % are twinned crystals.

As discussed in Chapter 3, by varying the polymer to metal precursor ratio and laser parameters, we obtain an assortment of nanocrystal shapes (Figure 4.8), including nanowires, emerald shapes, cubes and more exotic nanocrystal configurations that vary in size from tens of nanometers to several micrometers. The yield of

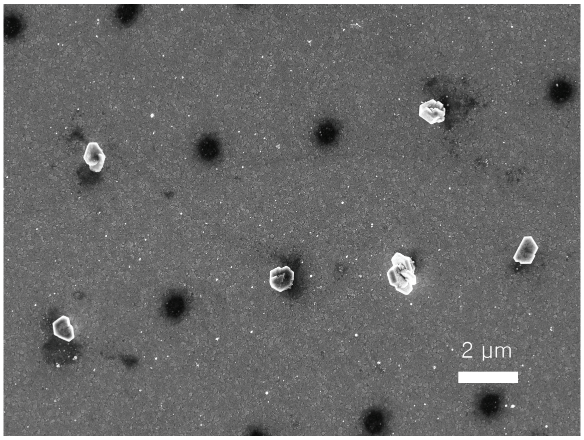

Figure 4.7: SEM image of laser irradiated area. Many crystals have been removed from the washing step.

these shapes is low compared to the yield of the hexagonal nanocrystals. However these nanocrystals are found only in the adjacent areas near laser irradiated spots. Therefore based on the unique hexagonal structure and the time scale of formation, we hypothesize that the femtosecond laser favors a non-equilibrium crystal growth path that mostly allows formation of hexagonal nanocrystals. This will be discussed more in section 4.1.2.3.

4.1.2.2 Doped film characterization

In order to study optical characteristics and degradation properties of the background matrix (before dissolving), we use a spectrophotometer and an ellipsometer to analyze a 160-nm thick doped film. Speed higher than 3000 rpm was used to spin-coat thinner films for analysis in an ellipsometer. (Typical spin-coating parameters of 1000 rpm spinning speed for 30 seconds produce a 1-μm film). Figure 4.9 is a transmission spectrum of the thin film. Lower transmission around 420 nm is due to the absorption from plasmon resonance of silver nanoparticles and the drop near 300 nm is from the

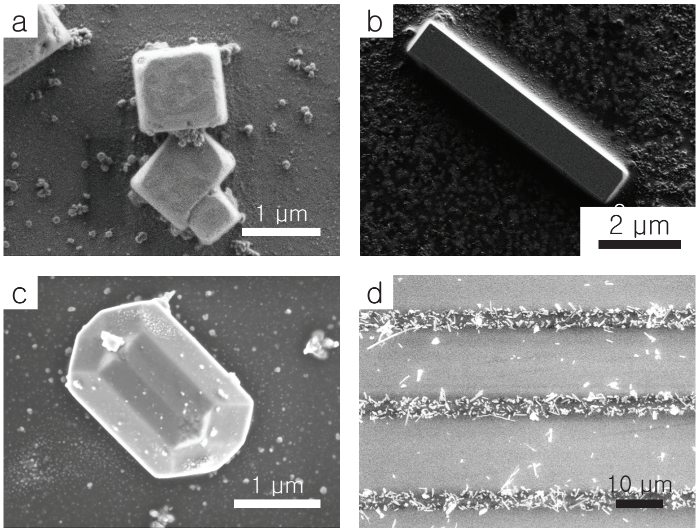

Figure 4.8: SEM images of various nanocrystals by varying PVP to $AgNO_3$ ratios: (a) nanocubes, (b)nanorods, (c) emerald shapes, (d) nanowires.

glass substrate.

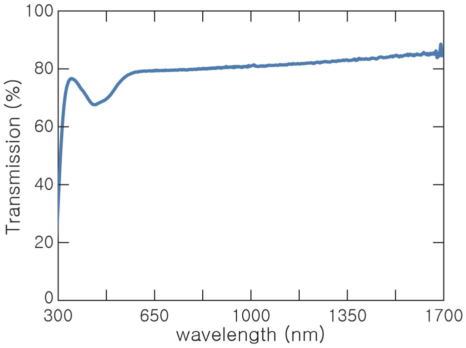

Figure 4.9: Transmission vs. wavelength of a doped PVP matrix with ethanol as a solvent.

Figure 4.10 show additional results acquired from the spectroscopic ellipsometer (right is a plot of the refractive index (n) and right is a plot of extinction coefficient (k)). With an ellipsometer, we can determine the optical constants by measuring the change in polarization as light reflects or transmits from our sample. B-Spline method was used to fit the parameters. B-spline fitting method is a mathematical parameter fitting model of a dielectric function that was developed by J.A.Woollam as an alternative to direct fits or oscillator models in typical ellipsometer softwares [151]. These films with the ethanol chemistry method were determined to have a graded refractive index layer with the top refractive index value being higher than the bottom layer. This may be due to the fact that as ethanol evaporates faster from the top layer, it forms a denser layer on the top. The difference in the k values were determined to be insignificant and showed same values throughout the top and bottom layer. The extra loss (increase in the k value) around ∼420 nm is due to the plasmon resonance from the silver nanoparticles. The inhomogeneous refractive index due to the evaporative nature of this matrix causes a problem when trying to develop three dimensional matrices. A method that we developed to resolve this problem will be discussed in Chapter 5. Furthermore, as studied in Chapter 3, the addition of alcohols into the solution expedites the initial silver seed growth process and leads to a faster degradation of the matrix. Therefore this method is only suitable for 2D fabrication and works favorably to crystal growing techniques.

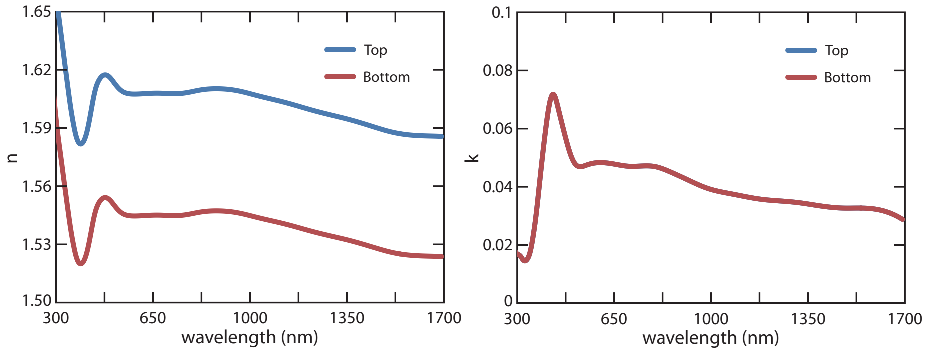

Figure 4.10: Ellipsometer results of n and k values for a doped PVP matrix with ethanol as a solvent. (Plots of k values are overlapped.)

4.1.2.3 Discussion

Traditionally, wet chemistry methods have been used to fabricate silver nanocrystals. However this is not a patternable technique that allows crystal formation in specific desired regions and is relatively slow; at a typical refluxing temperature of 120 to 160 °C and/or with a sodium or a halogen lamp, it takes between 0.5 and 30 hours to grow silver crystals between 80 nm and 280 nm in size [116, 117, 142, 143]. Below is a table of some of the wet chemistry methods.

By using traditional wet chemistry the shape and size of silver crystals can be tuned by varying chemical composition [116, 117, 142]. As discussed in Chapter 3, because PVP interacts preferentially with {100} planes in silver crystals, it results in a faster growth in specific crystal directions (that are covered less by PVP) which leads to cubic, spherical or rod silver nanocrystals [116, 117]. However, the size and shape of the nanocrystals we produce with the laser technique described in this letter are rarely observed using wet chemistry even when the same chemical reagent mixture is used [135, 143]. Extra additives such as sodium citrate must be added to the wet chemistry method to modify the nanocrystals into triangular or hexagonal shapes. In addition, the direct laser writing method uses exposure times that are over 8 orders of magnitude shorter and yet leads to larger crystals. Such ultrafast growth rate has not been previously reported. We hypothesize that the irradiation with our femtosecond laser system leads to plasmon resonances and higher temperatures in the irradiation focal volume during fabrication. These observations suggest that the non-equilibrium dynamics arising from the femtosecond excitation play a role in the ultrafast growth of hexagonal nanoprisms.

4.2 2D Lines & Grids

In this short section we present silver structures that are fabricated with a continuous exposure to create silver wires instead of crystals. We obtain similar results as other previously reported publications [62].

4.2.1 Materials & Method

Same materials, method and fabrication setup were used to fabricate 2D structures, such as lines and grids. Refer to section 4.1.1 for details. However, instead of using the AOM for spot-exposures, the lines were created with continuous irradiation. Same characterization tools were utilized.

4.2.2 Results & Discussion

Figure 4.11 shows various widths of silver wires we obtained ranging from 300 nm to 3μm depending on the various writing speeds and laser power. EDS measurements were taken to confirm the silver content (Figure 4.12). In addition to the silver peak, the EDS spectrum shows a very strong carbon peak which may be due to PVP being mixed in the fabricated silver wires[1].

As discussed in Chapter 3, gold also has a high reduction potential and therefore has a tendency to be easily reduced than other metals. Using the same setup, we can also fabricate gold wires. However experiment parameters have not been optimized

---

[1] Conductivity measurements were also carried out in order to determine the quality of the fabricated silver wires. However due to insufficient adhesiveness of the silver lines to the substrate, we were not able to fabricate intact lines that are long enough for a 4 point probe measurement. With a 2 point probe measurement we confirmed a large increase in the conductivity compared to the ITO substrate, but these results are not presented in this thesis due to insufficient data.

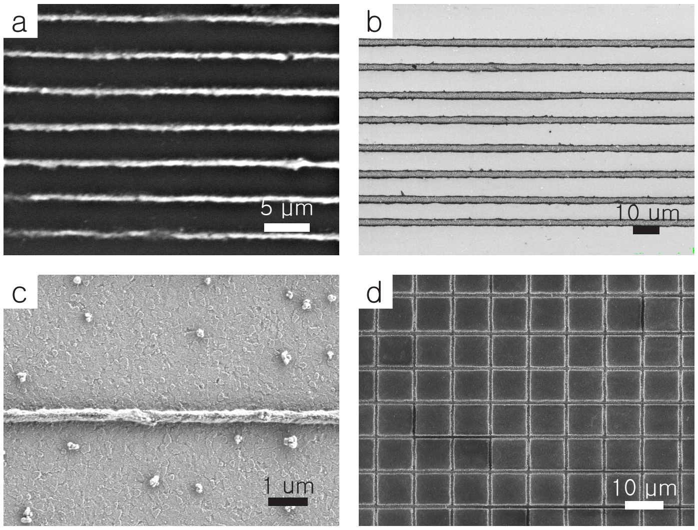

Figure 4.11: An SEM image of direct laser written 2D silver lines ((a)-(c)) and silver grid (d).

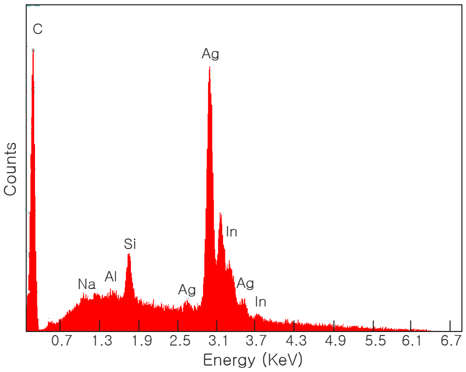

Figure 4.12: EDS of fabricated 2D Silver lines.

for this chemistry and more research needs to be conducted. Figure 4.13 shows gold lines fabricated with chloroauric acid ($HAuCl_4$), a gold precursor. A mixture of 0.33 g of $HAuCl_4$, 2 g of polyvinylalcohol and 20mL of deionized H_2O was used to make the doped film.

Although the preliminary result of gold fabrication was successful, throughout this thesis we focus only on silver structure fabrication to benefit from its low loss property in the optical regime [115].

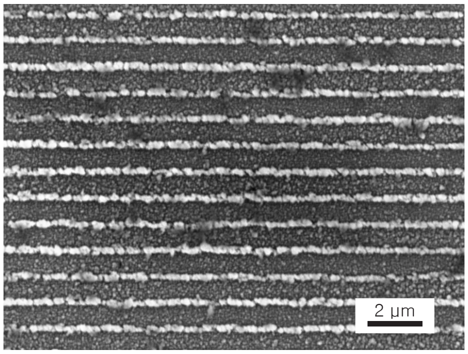

Figure 4.13: An SEM image of direct laser written 2D gold lines.

4.2.3 Annealing

Figure 4.14 shows a close-up image of the silver wires. We observe a high surface roughness structure with undissolved residual PVP in between the lines. To investigate whether we can reduce surface roughness and discontinuity in the structures, we test the annealing method.

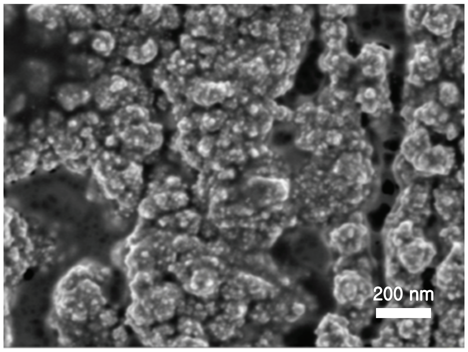

Figure 4.14: A magnified SEM image of one of the fabricated silver lines showing high roughness.

Among the three typical methods of annealing; Laser Anneal, furnace Anneal and rapid thermal anneal (RTA), we investigate furnace annealing and RTA method which are more cost-effective and have a higher throughput than the laser annealing method. Our preliminary results show no significant improvements in the structures at temperatures less than 300 °C. With an RTA that allows higher temperatures, we start observing Ostwald ripening around 750 °C which has adverse effects and decreases the quality of the structure by making the lines more discontinuous. Furnace annealing at temperatures between 300 °C and 750 °C also did not give any improvement in the quality of the silver structures and was unsuccessful at removing the residual polymer. Figure 4.15(a) and Figure 4.15(b) show pre- and post- RTA annealing at 750 °C. Figure 4.15(c) and Figure 4.15(d) show pre- and post- furnace annealing at a temperature around 500 °C. Bright rectangular areas are composed of tightly spaced fabricated lines and darker area surrounding the pads is the residual PVP.

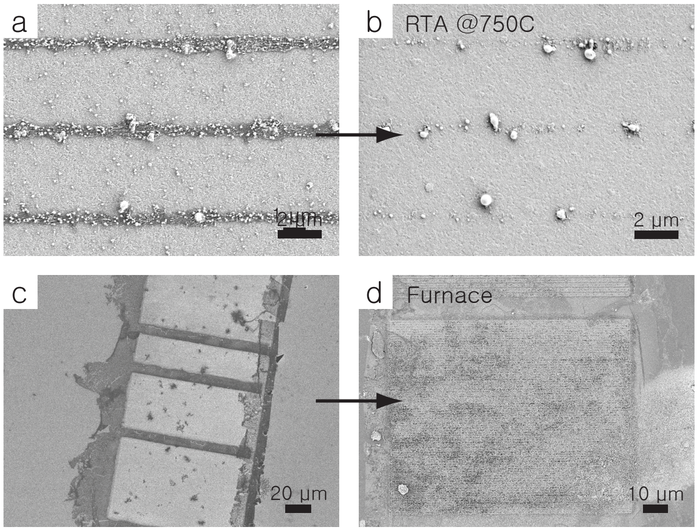

Figure 4.15: Pre- and post- annealing SEM images of direct laser written silver lines. (a) & (b) show pre- and post- RTA annealing at 750 °C. (c) & (d) show pre- and post- furnace annealing at a temperature around 500 °C.

Although more studies still need to be carried out, such as optimizing the annealing time, temperature, and gas flow, annealing does not seem to effectively resolve the surface roughness or the discontinuity problem. In Chapter 5, we present a new chemistry that allows us to fabricate higher quality 2D and 3D silver structures.

4.3 Summary

In conclusion, the femtosecond laser fabrication method combines the advantages of a bottom up cryatal growth technique with the positioning capability of top down patterning process. The use of femtosecond laser irradiation drastically increases the growth speed and size of nanocrystals compared to traditional techniques; we obtain hexagonal shapes that are hundreds of nanometers in size with sub-millisecond laser exposure. By fine tuning the laser parameters and chemical reagents, the technique outlined in this chapter may be modified to control the shape of silver crystals with increased yield.

Chapter 5

Direct laser writing of 3D metal structures in a polymer matrix

This chapter describes our innovative single-step silver growth technique for direct-writing disconnected silver nanostructures in 3D. Compared to other conventional techniques that typically require multiple time-consuming post steps to add metal layers, this technique allows us to directly create any metal patterns inside a dielectric medium. No photoinitiators or complex synthesized molecules are required for our process. We leverage nonlinear optical light-matter interactions and an accompanying photoreduction reaction to fabricate 3D silver structures at the nanoscale. Previous work on direct metal writing has largely been applied to generate 2D structures, [62,63,65,68,152] low resolution 3D structures [68,152], or freestanding 3D structures [63–65]. We demonstrate the writing of disconnected silver structures in 3D with 300-nm resolution (in PVP matrix) and 80-nm resolution (in gelatin matrix) and writing speeds up to 100 μm/s. Many metamaterial designs are based on metal/dielectric composites, so incorporating metal compositions into a bulk dielectric medium is crucial. This fabrication technique to write metal structures embedded in polymer provides us freedom to choose different types of polymers and to optimize them.

Section 5.1 presents our work on the fabrication of disconnected three-dimensional silver nanostructures in a PVP matrix for possible mid-IR photonics application. Section 5.2 will discuss the technique in a gelatin matrix for possible vis-near IR and THz photonics applications.

5.1 Silver nanostructures in PVP matrix for vis-near IR and mid-IR applications

We present a simple, one-step technique for direct-writing of a structured nanocomposite material with disconnected silver nanostructures in a polymer matrix. A nonlinear optical interaction between femtosecond laser pulses and a composite material creates silver structures that are embedded inside a polymer with submicrometer resolution (300 nm). We create complex patterns of silver nanostructures in three dimensions. The key to the process is the chemical composition of the sample that provides both a support matrix and controlled growth. This technique offers a cost-effective approach for the fabrication of bulk optical devices with engineered dispersion.

The silver is grown inside a polymer support matrix, enabling us to move beyond freestanding structures to create arbitrary 3D disconnected silver patterns with submicrometer resolution.

5.1.1 Materials & Method

5.1.1.1 Materials

Silver nitrate ($AgNO_3$) was purchased from Sigma-Aldrich. Polyvinylpyrrolidone (PVP) with an average molecular weight of 58,000 g was chosen for this method and was purchased from Alfa Aesar. Mercapto propyl trimethoxy silane (MPTS) was purchased from Alfa Aesar. Deionized water was used. Regular 25 × 75 mm plain, precleaned microscope glass slides were purchased from VWR and were cleaved into a third to make 25 × 25 mm glass substrates for sample preparation.

5.1.1.2 Method

Sample preparation

We use a mixture of PVP, $AgNO_3$, and deionized(DI) water to make a 0.16M $AgNO_3$ solution, with polyvinylpyrrolidone (PVP) as support polymer and DI water as solvent. In detail, we first prepare a solution by dissolving 0.206 g of PVP in 8 mL of DI water at room temperature. Next 0.21 g of $AgNO_3$ is added to the mixture. Once both mixtures are dissolved, we drop-cast 1 mL of the prepared solution onto a glass slide. Lastly, the sample is baked in an oven for 2 hours at 50 °C. These steps are done in a room filtered of ultraviolet light to minimize unnecessary silver nanoparticle formation. The resulting sample consists of approximately 200-μm thick polymer layer doped with silver ions on a glass substrate. For SEM analysis, 2D samples were made on a glass substrate that was oxygen plasma treated and silanized with MPTS prior to depositing the mixture. Then the fabricated samples that include glass-substrate bound patterns are immersed in water at RT to dissolve the polymer layer, leaving behind only the 2D patterns for further analysis. A thin layer of gold or platinum was sputter-coated to reduce charging while SEM imaging. Figure 5.1 is a schematic of the sample preparation steps.

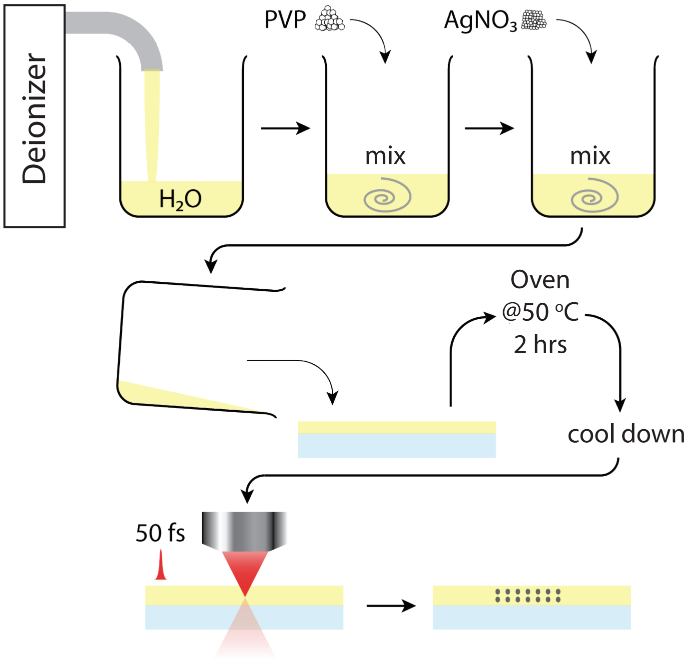

Figure 5.1: Schematic of sample preparation steps for writing 3D metallic structures in a dielectric matrix.

Laser fabrication

We use a Ti:sapphire laser centered at 795 nm with an 11-MHz repetition rate, and 50-fs pulse length for the irradiation process. Refer to 4.1.1.2 for a schematic of the set-up. This is the same laser set-up that was used to create 2D nanocrystals. An objective with a numerical aperture (NA) of 0.8 focuses the pulses into the sample. The laser is focused inside the bulk of the doped PVP matrix to create multi-layered 3D structures. At the focus, nonlinear light-matter interactions induce metal-ion photoreduction processes in a volume smaller than the diffraction-limited focal spot initiating silver nanocrystal growth. By varying the laser parameters we can adjust the size of the resulting silver structures. At an exposure of 1.3×10^6 pulses per voxel with 0.15 nJ per pulse, we create structures clearly resolved by optical imaging.

Characterization

SEM, EDS and EBSD measurements were performed in Zeiss ULTRA and SUPRA 55VP microscopes, using in-lens, EDAX and EBSD detectors. Optical measurements on doped films (prior to laser exposure) were made with Hitachi U-4100 spectrophotometer and J.A.Woollam V VASE-32 spectroscopic ellipsometer. Electron Microscopy Sciences (EMS) 300TD Dual Head Sputter Coater was used to sputter-coat a 5-10 nm of gold or platinum for SEM imaging 2D structures.

5.1.2 Results & Discussion

5.1.2.1 Structural characterization

Figure 5.2 shows a 3D rendering of stacks of sequential 2D in-situ bright-field optical images taken of an array of silver voxels; adjacent rows of voxels are in different vertical planes. The images highlight a key attribute of our fabrication process: we can direct-write silver structures that are disconnected in 3D inside a polymer.

Figure 5.3 shows optical images of a sample, similar to the one fabricated in Figure 5.2(a), captured by an in-situ microscope. At different stage positions in the z-direction (from z=0 μm to 6.2 μm), different layers come into focus. Silver dots at the ends of each line are larger than the rest of the dots due to longer laser exposure.

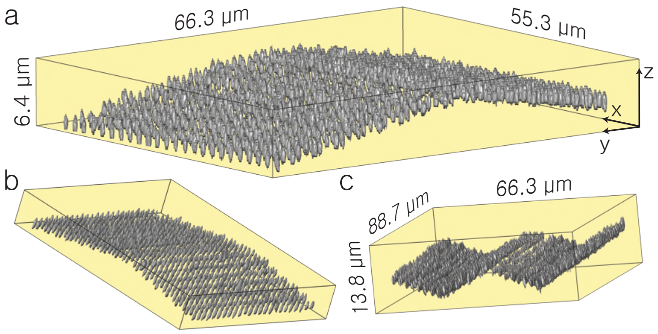

Figure 5.2: 3D rendering of stacks of sequential in-situ bright-field optical microscopy images of fabricated structures. (a,b) An array of silver voxels fabricated in a single tent structure fabricated at an exposure of 1.3 x 10^6 pulses with 0.15 nJ per voxel. The stage was translated at 10 μm/s during fabrication. The chosen exposure creates features clearly resolved by optical imaging. Neighboring rows of patterned features are in different z-planes. For clarity, the z-scale is stretched by a factor of 1.6 relative to the x- and y-scales. (c) Portion of an array of tent structures fabricated using the same parameters. The feature size imaged with optical microscopy is limited by the spatial resolution of the in-situ microscope.

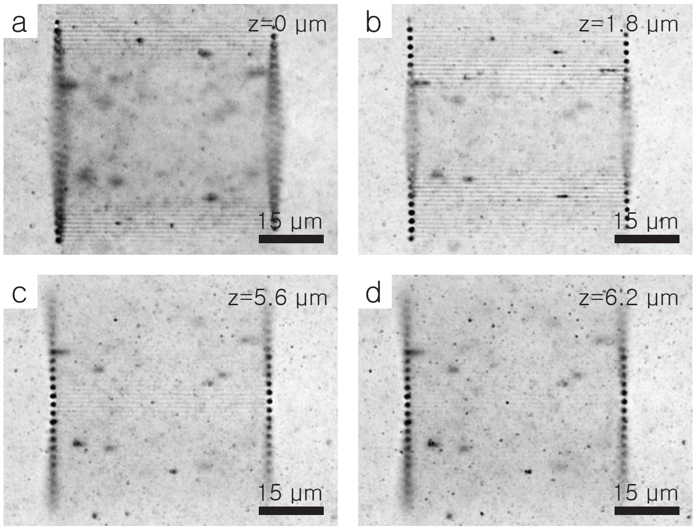

Figure 5.3: In-situ optical images of a 3D tent structure taken at different focal lengths. Images are taken as the image focal plane is raised from (a) bottom of the structure to (d) apex of the tent.

Figure 5.4 shows additional 3D rendered images of sequential stacks of in-situ bright-field optical microscopy images of various fabricated structures. Figures 5.4 (a) and (b) are from a 2 layer structure where smaller dots were fabricated on top of a layer of larger dots. Figure 5.4(c) is from a dotted spiral structure.

ąą

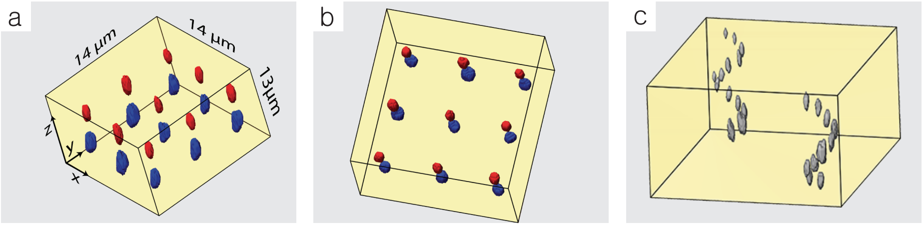

ąą

Figure 5.4: Rendered images of fabricated 3D silver structures. (a) & (b) show two layer silver dot structure with a smaller sized dots on top layer. (c) shows silver dots fabricated in a spiral.

When we reduce the laser exposure to 2.8×10^5 pulses per voxel with 0.2 nJ per pulse, the silver features are reduced to submicrometer scales (less than 300 nm, Figure 5.5). At the operating wavelength of 795 nm, the transverse resolution of our overfilled microscope objective is approximately 600 nm – about twice the size of the fabricated nanostructure in Figure 5.5(c). Unlike most multiphoton absorption lithography techniques that use oil immersion objectives to achieve high resolution, our results were obtained at a numerical aperture of 0.8. Although higher-NA objectives have a smaller focal volume, the primary advantage of a lower-NA objective is the longer working distance (3 mm), which is useful for bulk 3D nanolithography. In addition to enabling 3D disconnected nanostructure fabrication, our process is approximately two orders of magnitude faster than other 3D direct-write techniques with similar resolution [63] using an 11-MHz laser we achieve write speeds of 100 μm/s.

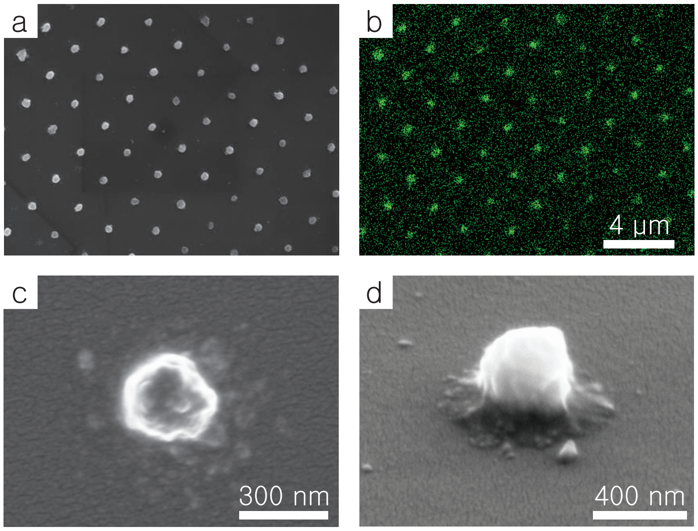

Figure 5.5: High-resolution SEM images of a patterned sample. (a) An image of a 2D array of dots and (b) its corresponding EDS silver elemental map confirm that silver structures are grown in areas irradiated by the laser. Close-up views of individual dots shown (c) head on and (d) at a 61° tilt angle. SEM imaging requires a washing step to avoid sample contamination from additional silver growth driven by the electron beam.

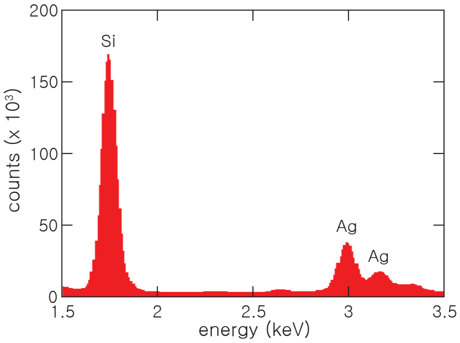

Figure 5.6: EDS spectrum of the patterned silver structure. Strong silver signal is detected with a Si signal that is from the glass substrate.

To determine the constituent elements in the direct written features, we used high-resolution energy dispersion x-ray spectroscopy (EDS) and scanning electron microscopy (SEM). Figure 5.5 (a) shows SEM images of an array of dots fabricated on a glass substrate. Figure 5.5 (b) shows its corresponding high-resolution EDS silver elemental map, confirming that the fabricated dots contain silver. The presence of silver is corroborated by a strong silver signal in the EDS spectrum (Figure 5.6) of a patterned feature. The strong Si peak is due to the glass substrate underneath.

Further characterization through transmission electron microscopy (TEM) (Figure 5.7) indicates that the silver does not grow as a single crystal in each irradiated voxel; rather, structures are composed of agglomerations of smaller silver nanoparticles. The inset of Figure 5.7 is a higher magnification image of a silver nanoparticle created during the fabrication process that shows a clear silver lattice structure.

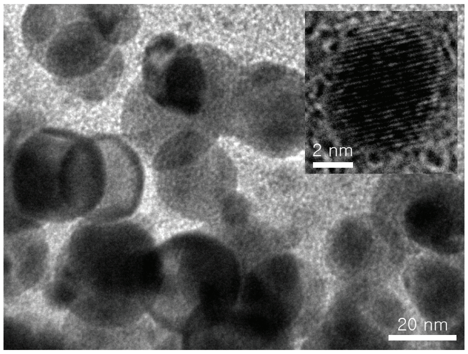

Figure 5.7: TEM image of fabricated silver structures. The silver does not grow as a single crystal in each irradiated voxel. Instead the silver structures are composed of agglomerations of smaller silver nanoparticles. The inset shows a close-up view of a silver nanoparticle.

Ultraviolet and visible micro-absorption and scattering spectroscopy (Figure 5.8) shows a characteristic silver surface plasmon peak centered around 425 nm. The broad extinction spectrum indicates polydispersity of the silver nanoparticle size.

Most work on high-resolution 3D femtosecond laser direct-writing involves reagent combinations that either include an alcohol solvent or omit the polymer. For example, a solution of $AgNO_3$ in H2O can be used to direct-write silver nanostructures, [64] but does not offer a solid matrix for support. In contrast, a polyol based system using

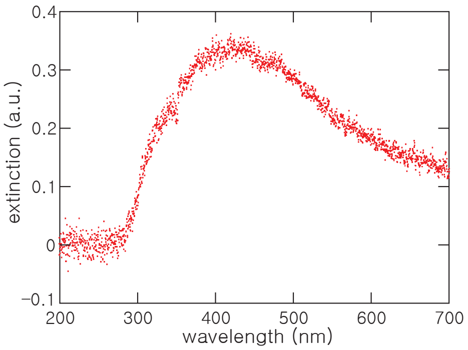

Figure 5.8: Extinction spectrum of silver nanoparticles from direct laser written silver structures

$AgNO_3$, PVP, H_2O and ethanol [62, 68] has a polymer that could act as a support matrix, but the redox interactions between ethanol -OH groups and Ag^+ ions begin immediately upon reagent mixing causing nanoparticle growth throughout the sample. Thus, the polyol mediated growth technique, as it is, cannot be used to provide a polymer support matrix for 3D laser writing. By omitting the alcohol solvent, however, we found that the reduction reactions decrease significantly. We retained PVP as a support matrix because it helps control silver nanoparticle synthesis. [116, 117] By optimizing the concentration of PVP in H_2O, we simultaneously gain control over the localization of Ag^+ reduction processes and obtain a polymer support matrix. Our technique does not require addition of two-photon dyes, seed nanoparticles, or non-commercially available reagents.

The key to our fabrication process is the chemical composition of the sample. Conventional methods to synthesize silver nanoparticles and nanostructures through polyol processes [116, 117] are subject to redox reactions unfavorable for polymer-embedded 3D silver nanofabrication. In the process we present here, PVP is dissolved in H_2O, minimizing reduction reactions outside the laser-irradiated volume.

PVP plays an important role in controlling the size and shape of silver nanoparticles: the strong affinity of N and O atoms in the amide groups of PVP to surfaces of transition-metal clusters restrains their growth [116,117,153]. By combining PVP and water we obtain both a support matrix and controlled growth. Nonlinear light matter interactions then permit the direct writing of silver nanostructures in the bulk of the sample. Transmission measurements indicate the support matrix has several transparency windows in the near-infrared and infrared portions of the electromagnetic spectrum.

5.1.2.2 Optical characterization

Figure 5.9 shows a transmission spectrum of the doped PVP matrix (unpatterned) spanning a range of 0.35 μm to 16 μm. There are two high transparency windows in the vis-near IR and mid-IR regimes; this allows for the possibility of creating electromagnetic metamaterial devices for these regions

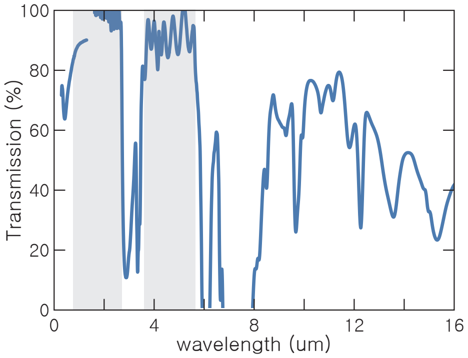

Figure 5.9: Transmission vs. wavelength plot of a doped PVP matrix (unpatterned) measured from 0.35 μm to 16 μm.

To find values of n and k for further theoretical studies to design metamaterials, optical properties of a 50-nm thick Ag ion doped PVP film was measured. Speed higher than 3000 rpm was used to spin-coat to make very thin films for analysis using an ellipsometer. Typical method of fabrication is drop-casting which generates ∼13μm films. Figure 5.10 is a n vs. wavelength plot and a k vs. wavelength plot of the doped PVP film. Higher extinction around 420 nm is due to plasmon resonance form the silver nanoparticles.

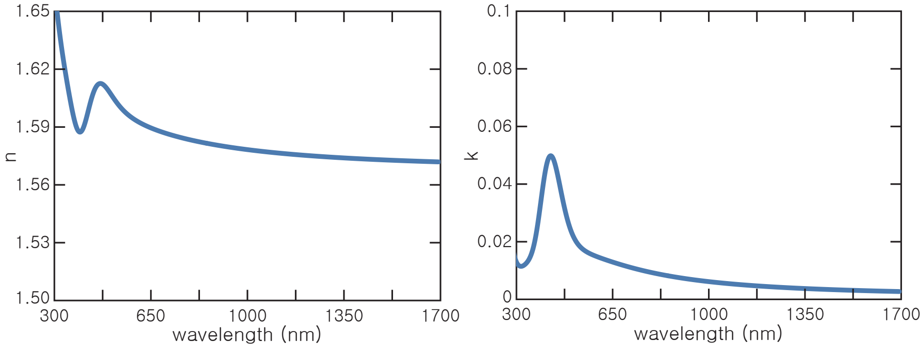

Figure 5.10: n vs. wavelength plot and a k vs. wavelength plot of a doped PVP film. Higher extinction around 420 nm is due to plasmon resonance from the silver nanoparticles.

5.2 Silver nanostructures in gelatin matrix for vis-near IR and THz applications

In this section we present a new chemistry method to fabricate higher-resolution silver nanostructures in 3D using femtosecond laser direct metal writing. Nonlinear absorption inside a gelatin matrix doped with silver ions leads to the growth of silver nanostructures embedded and fixed inside a dielectric matrix. 2D SEM images show sub-100 nm features. Gelatin provides several advantages over previously reported dielectric matrices for the fabrication of 3D nanostructures. The gelatin-silver matrix is an order of magnitude thicker allowing more layers during bulk 3D nanofabrication; it has over an order of magnitude longer shelf life; it has fewer defects in the matrix; it produces a much smaller silver feature size; and it is stretchable up to 10 %. Lastly, it has good transmission window for vis-near IR and THz metamaterial device applications.

5.2.1 Materials & Method

5.2.1.1 Materials

Silver nitrate ($AgNO_3$) and type B[1] bovine gelatin were purchased from Sigma-Aldrich. Gel strength is indicated by Bloom, which can be determined by a method that was developed in 1925 by O. T. Bloom [155]. For this method, a Bloom grade[2] of 75 was chosen to fabricate a flexible substrate. Mercapto propyl trimethoxy silane (MPTS) was purchased from Alfa Aesar. Deionized water was used.

5.2.1.2 Method

Sample preparation

To fabricate the nanostructures we use a mixture of gelatin, silver nitrate ($AgNO_3$), and deionized water. We prepare a solution by dissolving 0.8 g of gelatin in 4 mL of deionized water in a vial. We mix the two components using a vortex mixer then heat the sample vial in a 55 °C water bath to dissolve the gelatin. We repeat this step until

---

[1] Gelatin is derived from collagen protein, which is retrieved from cows, pigs, fish and poultry. When collagen is treated with either alkali or acid, it breaks up to form type A or type B gelatin, respectively. [154]

[2] The "Bloom" test determines the weight of gelatin(in g) needed by a probe (typically with a diameter of 0.5 inch) to deflect the surface of the gel 4 mm without breaking it [155]. Typical gelatin ranges from 50-300 Bloom. Higher number means higher gelatin strength.

all the gelatin fully dissolves. Next, we add 0.105 g of $AgNO_3$ to the vial and repeat the above mixing step until all the $AgNO_3$ has completely dissolved. We drop cast the prepared solution onto a 1-inch by 1-inch glass slide. Lastly, the sample is air-dried at room temperature overnight. The resulting sample consists of approximately 200-μm thick gelatin film doped with silver ions on a glass substrate. To create 2D samples for SEM analysis, the glass substrate is oxygen plasma treated and silanized with MPTS prior to depositing the mixture. Then the fabricated samples that include glass-substrate bound patterns are immersed in water at 55 °C to dissolve the polymer layer, leaving behind only the 2D patterns. These glass substrates for 2D purposes were treated with MPTS silane prior to sample deposition.

Laser fabrication

We use a Ti:sapphire laser centered at 795 nm with an 11-MHz repetition rate, and 50-fs pulse length for the irradiation process. A detailed description of the laser fabrication setup can be found in references [144], [145] and Chapter 4. The laser exposure is limited to individual voxels where the focal volume has a full-width half-max diameter of 1 μm. The numerical aperture (NA) of the objective is 0.8, and the working distance is 3 mm. 3D structures are created by focusing laser pulses inside the bulk of the gelatin matrix; layers are patterned sequentially starting from the layer closest to the substrate and moving towards the air interface. This is a single step process and does not require further processing. To create planar 2D patterns that are suitable for SEM analysis for example, laser pulses are focused near the substrate such that the grown silver is bound to the glass.

Structure characterization

SEM and EDS measurements were performed in Zeiss Ultra and SUPRA 55VP microscopes, using in-lens and EDAX detectors. The stretcheability of a 200-μm thick silver-doped gelatin matrix was determined by using an Instron 3342 tensile measurement setup. Transmittance measurements were made in 4 different regions on a 200-μm thick unpatterned silver-doped gelatin matrix. The 200-1750 nm wavelength range was probed using a Cary 500i UV-Vis-NIR dual-beam spectrophotometer. Transmittance in the 1.8-15 μm wavelength range was measured using a Thermo Fisher continuum fourier transform infrared (FTIR) microscope connected to a Thermo Fisher FTIR 6700 spectrometer. The 15-200 μm wavelength range was measured using a Thermo Fisher FTIR 6700 spectrometer. The 200-1,500 μm (THz) range was measured using a broadband Hg-arc lamp THz source and a liquid helium-cooled Si bolometer detector.

5.2.2 Results & Discussion

Nonlinear absorption inside a gelatin matrix doped with silver ions induces the growth of silver nanostructures to be embedded inside the dielectric matrix. Gelatin provides several advantages over previously reported materials for the fabrication of 3D nanostructures. Gelatin is an easy to use, inexpensive, non-toxic, biodegradable, water soluble polymer that has hydrogel-like gelling properties. This allows us to make thicker and more durable samples with reduced brittleness and increased sample lifetime. Its numerous electron donor groups in the polymer chain help fabrication of high resolution silver structures and limit unnecessary growth which results in fewer defects in the matrix. We obtained sub-100nm silver features and fabricated more than 16 layers. The doped gelatin matrix is also stretchable up to 10 %, allowing the possibility of flexible devices. Lastly, it has high transparency windows that correspond well to potential applications in optical and THz metamaterial.

5.2.2.1 Structural characterization

Transmission optical microscopy images of a fabricated 3D silver pattern are shown in Figure 5.11. Figure 5.11a and 5.11b show two representative in-situ images taken from a 10-layer array of dots. Figure 5.11c shows a computer generated model to illustrate the 3D pattern. The pattern contains alternating layers of silver dots arranged in square (Figure 5.11a) and pseudo-hexagonal arrays (Figure 5.11b). The 3D pattern is fabricated by irradiating layers sequentially. Since the background matrix is solid and provides mechanical support, it is possible to create silver structures that are disconnected in the z-direction, as shown in Figure 5.11.

Figure 5.12 shows a scanning electron microscopy (SEM) image of an array of silver dots with sub-100-nm size, which is smaller than any other previously reported direct metal writing results. [63–65, 68, 144, 145, 156] We measure silver diameters as small as 80 nm. Unlike previous reports showing silver nanoparticle aggregates with high roughness, there are no readily visible domain separations in these nanostructures. [63–65, 68, 144, 145, 156] The dots are fabricated with an exposure of 79,000 pulses with 0.1 nJ per pulse at a stage translation speed of 10 μm/s.

Figure 5.13 shows an SEM image of a 100 nm fabricated dot (Figure 5.13a) and its corresponding energy dispersion spectroscopy (EDS) map (Figure 5.13b) of

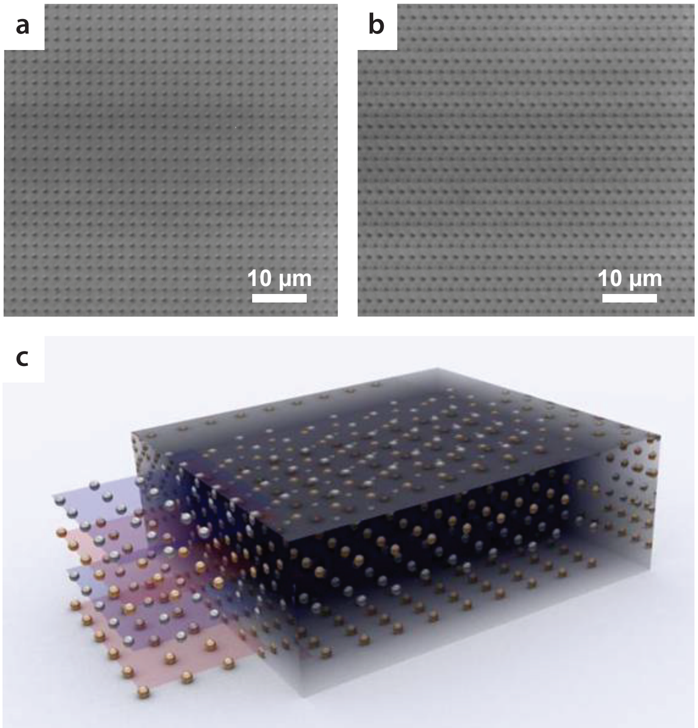

Figure 5.11: In-situ optical images of interleaved (a) square and (b) pseudo-hexagonal arrays of silver dots that alternate over the z-direction as part of a 10-layered 3D pattern inside gelatin. The pitch between dots is 2 μm in the x-direction, 2 μm in the y- direction and 4 μm in the z- direction. (c) A computer generated image provides a schematic illustration of the 3D pattern.

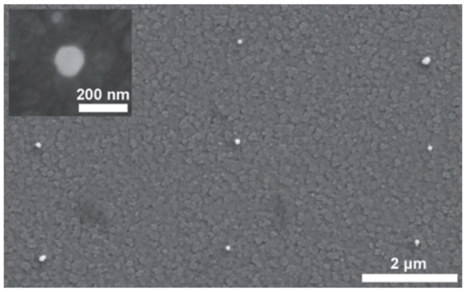

Figure 5.12: SEM image of an array of fabricated silver nanostructures. There is some variability in the size, with the smallest structures being sub-100nm in diameter. The inset shows a closeup view of a single silver nanostructure.

silver-element signal. We also show EDS spectra from the nanodot (Figure 5.13c) and a directly adjacent area (Figure 5.13d). The spectra show a strong silver signal from the dot compared to the neighboring volume. The signals next to the silver peak are from the indium-tin-oxide layer on the substrate (under the silver dot). EDS data indicates that fabricated dots are composed of silver. Furthermore the SEM image shows a smoother structure compared to previous reports. [63–65, 68, 144, 145, 156] The Ag signal from the spectrum is also significantly stronger than any previously reported for silver direct laser writing. [63–65, 68, 144, 156]

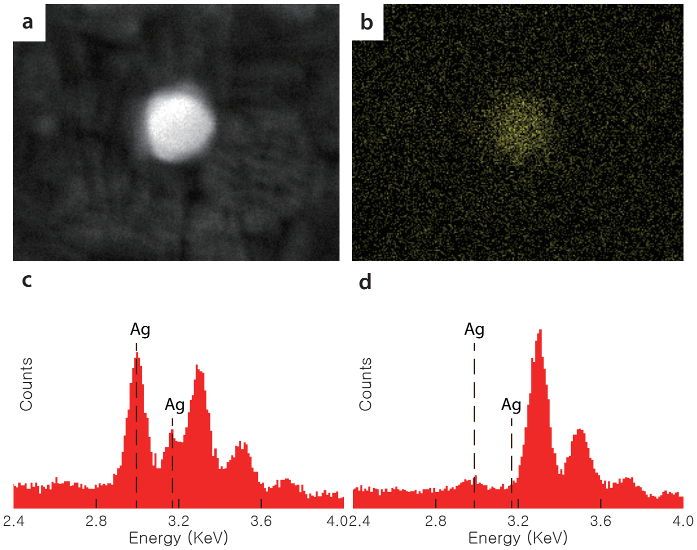

Figure 5.13: (a) An SEM image and its corresponding (b) EDS map of elemental silver for a 100-nm fabricated structure. The EDS map shows strong silver signal from the nano-dot. The EDS spectra taken from (c) the nanodot (d) and its neighboring area clearly indicate that the silver signal stems from the fabricated nanostructure. The peaks next to the silver signal are from a layer of indium tin oxide on the glass substrate to relieve charging problems during SEM analysis.

The critical difference between the method described here and previously reported femtosecond laser writing works arises from our choice of using gelatin as the background matrix [63–65, 68, 144, 145, 156]. The matrix both helps growth, and mechanically supports silver nanostructures. Gelatin is comprised of high molecular weight water-soluble long protein strands derived from collagen, which leads to large amounts of C=O, -COOH and -NH2 polar groups. We hypothesize that a nonlinear optical interactions between the carbonyl group and femtosecond pulses induces a metal-ion photoreduction process, and the extra lone pairs in the polar groups (such as -COOH and -NH2) restrain silver particle growth through strong affinity towards Ag^+ ions. We believe the large amount of lone pair groups with long chains of gelatin compared to other polymers restrains silver growth more effectively during femtosecond laser irradiation and allow us to fabricate 3D silver nanostructures with sub 100-nm resolution in a matrix with fewer defects.

Furthermore gelatin goes through a gelation process during the air-drying procedure where abundant oxygen and hydrogen in the long strands of protein form hydrogen bonds to create a tangled network. [154] Water can remain captured between these hydrophilic strands, which allows gelatin to have hydro-gel like (or elastomer like) behaviors. This increased viscosity allows us to make samples that are thick (over 200 μm) and stretchable. Measurements with a tensile testing device (Figure 5.14) show approximately 10% stretchability). Tangential modulus[3] was determined to be roughly 0.2 GPa which also shows the softness when compared to other values (steel: 207 GPa, Aluminum: 69 GPa, silver: 74 GPa, PMMA & PS: around 3 GPa, Polyethylene: around 0.2 GPa) [157, 158].

---

[3] Young's modulus (or modulus of elasticity) is the ratio of stress to strain in a material. Since this is a polymer it doesn't show totally elastic behavior and instead shows a slight non-linear stress-strain curve. For a more complete characterization, techniques such as nanoindentation technique should be used.

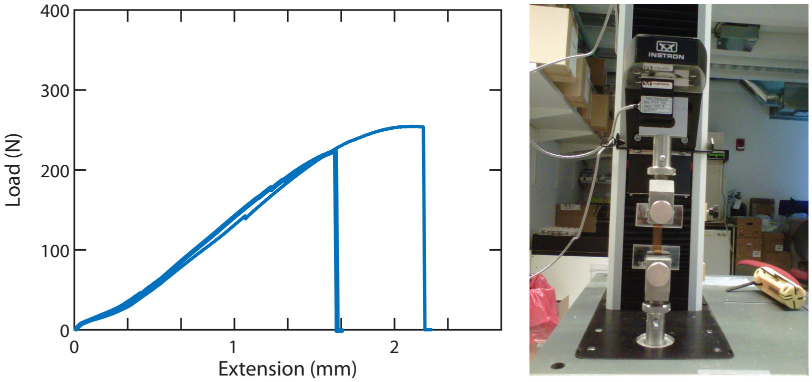

Figure 5.14: Tensile load vs. extension plot of a 215-μm thick doped gelatin matrix (left). Instron tensile testing equipment shown on right.

By carefully choosing the gel strength and optimizing its concentration, we obtain gelatin films that exhibit durable (reduced brittleness and increased sample lifetime) and stretchable behavior while being suitable for 3D silver growth during femtosecond laser irradiation. Figure 5.15 below compares the brittleness of a doped PVP matrix with the flexible gelatin matrix. The stetchability of the gelatin matrix also opens the door for creating tunable optical devices.

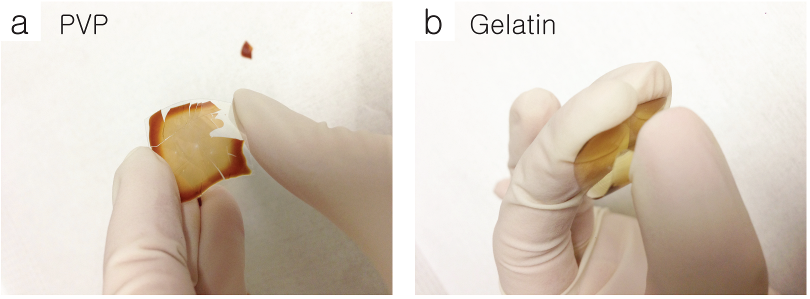

Figure 5.15: (a) A 13-μm doped PVP matrix on acetate film (for support) showing brittleness. (b) A 230-μm doped gelatin matrix showing flexibility

5.2.2.2 Optical characterization

Figure 5.16 shows a transmission spectrum of the doped gelatin matrix (unpatterned) spanning a range of 0.2 μm to 1,500 μm. There are two high transparency windows in the optical and THz regimes. This allows for the possibility of creating electromagnetic metamaterial devices for these regions.

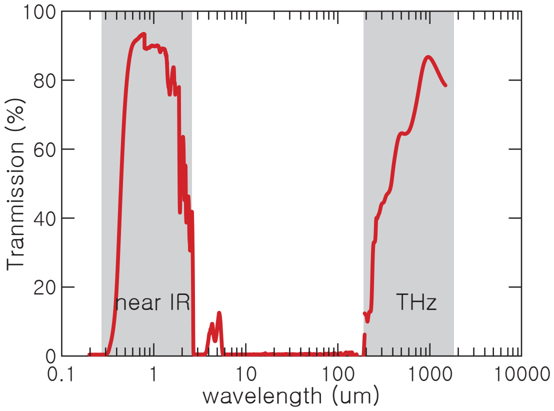

Figure 5.16: Transmission spectrum for an unpatterned silver-ion-doped gelatin sample. The spectrum, obtained through measurements on multiple instruments, spans the ultraviolet to terahertz wavelength range of the electromagnetic spectrum (0.2-1,500 μm). The x-axis is plotted with a log-scale. The spectrum shows two high transmission windows. The first window is in the visible to near-IR range and the second window is in the terahertz range. These windows indicate regions where electromagnetic devices could be designed.

To find values of n and k for further theoretical studies to design metamaterials, optical parameters of a 60-nm thick doped gelatin film were measured. Typical sample thickness acquired from a drop-casting method is 200 μm. A spin coat speed higher than 3000 rpm was used to make very thin films for analysis using an ellipsometer. Figure 5.17 shows n vs. wavelength for our doped gelatin film. The values of refractive index are higher than PVP due to the longer and denser polymer chain network in the gelatin matrix. Fitted k values were ∼0 showing low loss. No resonance is observed around 420 nm suggesting negligible silver nanoparticle formation.

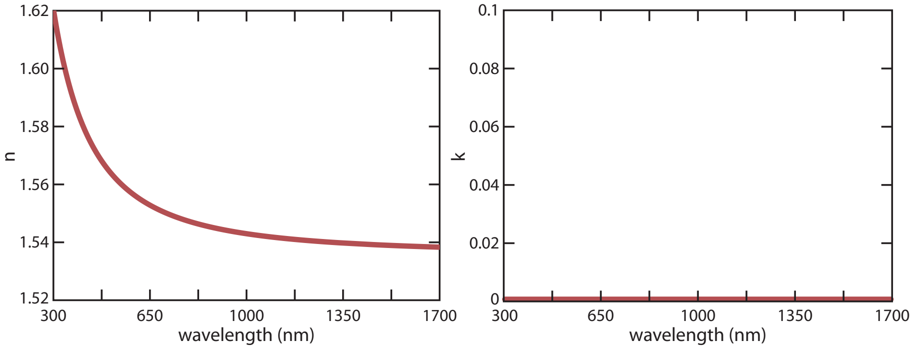

Figure 5.17: Index of refraction (n) (left) and extinction coefficient (k) (right) vs. wavelength plot of a doped gelatin matrix before laser irradiation, measure with an ellipsometer

Figure 5.18 compares refractive index values of various gelatin concentrations. As one would expect, the half-concentration gelatin film (gelatin 0.4 g) had the lowest refractive index. The doped gelatin matrix (ready for writing structures that includes 0.8 g of gelatin and 0.105 g of silver nitrate) had the highest refractive index possibly due to initial atomic silver formation.

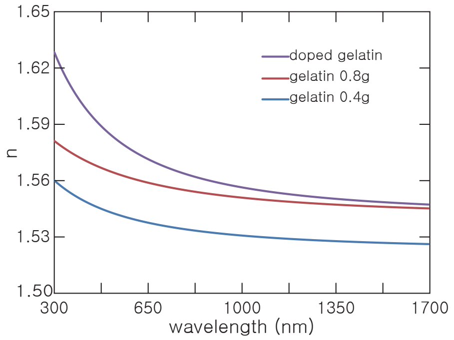

Figure 5.18: n vs. wavelength for different concentrations of gelatin

The method presented in this section can easily produce many disconnected layers of metal patterns. We readily produce over 15 layers of structures using the single-step writing process.

5.3 Applications

5.3.1 Diffraction gratings

As a first step to confirm that we can produce high quality silver structrures for optical device applications we fabricated a 3D silver diffraction grating. Just like in TEM electron diffraction where atoms act as scattering centers, the fabricated silver dot structures in our structures act as scatter centers. Figure 5.19 shows the diffraction pattern we acquired from a 10 layer BCC lattice tiled at 30° degrees with a continuous 633-nm wave laser source. Laser power of 0.05 mW and an exposure of 30 seconds were used to produce the pattern. The number of diffraction spots and their position match pretty well with our theoretical prediction using Ewald sphere construction that meets the Laue diffraction condition.

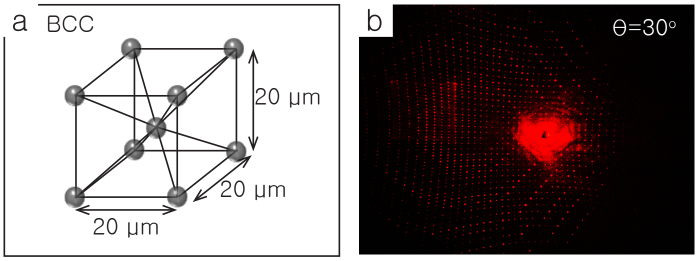

Figure 5.19: Diagram of a unit cell of a body-centered-cubic (BCC) diffraction grating (a) and its diffraction pattern (b). (Results soon to be published. Moebius et al. (2014))

5.3.2 Zone plates

A zone plate is a device composed of circular diffraction gratings that is used to focus waves [159]. Since zone plates use diffraction phenomenon instead of refraction or reflection, it can be used as an application for any wavelength and eliminate the need of selecting an optimal transparent medium for each wavelength [160]. One zone plate can be used to focus several wavelengths to different focal lengths, or different zone plates can be used to vary focal lengths for a single wavelength.

In addition to fabricating zone plates for focusing optics, by utilizing our 3D fabrication technology, we can create multi-layer optics comprised of two layers of zone plates and a pinhole in the mid layer to create a device for collimating light as in Figure 5.20. A pinhole is added to cut out the 2nd, 3rd (and so forth) order diffractions.

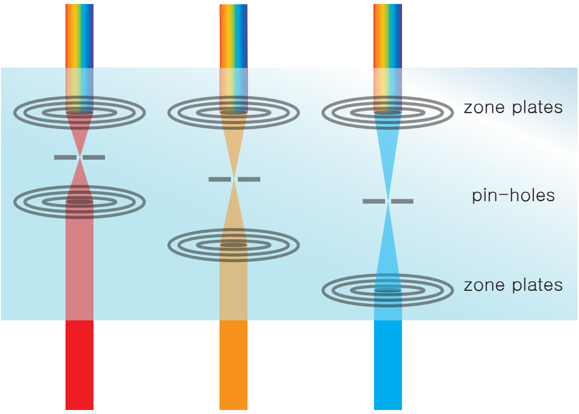

Figure 5.20: Schematic illustration of a multi-layer zone plate application.

Figure 5.21 is a preliminary result of our single layer zone plates. Figure 5.21a shows a 50-μm focal length (in air) single layer zone plate fabricated with our direct laser writing method. Using the same setup as in Chapters 4 and 5, an average laser power of 4-20 mW was used with writing speed varying from 10 to 200 μm/s. Figure 5.21b shows light getting focused when the stage was translated about 50 μm. Figure 5.21c is a traditional e-beam lithography patterned zone plate and Figure 5.21d shows the focused light (results to be published. Moebius et al. (2014)).

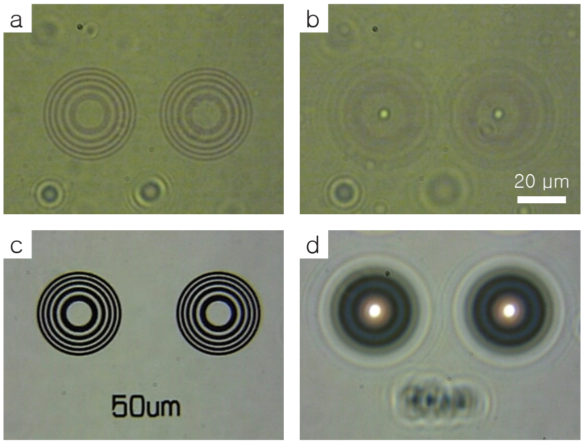

Figure 5.21: A set of one-layer zone plates: (a) direct laser written zone plates without illumination. (b) direct laser written zone plates with illumination showing focusing effect. (c) zone plates made with e-beam lithography (without illumination), (d) zone plates made with e-beam lithography showing focusing effect. (Results soon to be published. Moebius et al. (2014))

5.3.3 Other examples

With our fabrication method we can make connected and/or disconnected metal structures in a dielectric matrix. To fabricate free-standing 3D structures, we would just have to write the 3D structure at the interface of the substrate and the polymer matrix and wash away the unexposed polymer layer with a solvent to leave the free-standing structure behind. Both of these options give many possibilities to fabricate various kinds of complicated structures for various device applications and even an option to create truly isotropically functional 3D metamaterials that are independent of direction of propagation and polarization of the incident light. All the metamaterials so far have been metasurfaces, which depend on the direction and the polarization of the incident light. We can realize structures such as the one Guney and his collaborators theoretically demonstrated [18]. Figure 5.22 is a schematic of the studied structure and Figure 5.23 shows simulated values of effective refractive index, permeability and permittivity.

Figure 5.22: Diagrams of a three-dimensionally isotropic optical NIM. Adapted from reference [18].

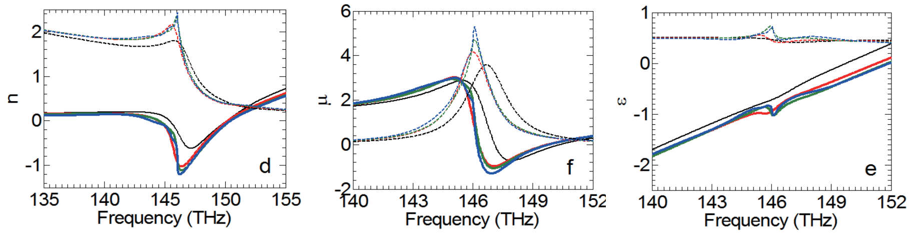

Figure 5.23: Effective refractive index (left), μ (center), and ε (right) of the fully isotropic optical negative index metamaterial from Figure 5.22. Adapted from reference [18].

These designs were originally designed for a two-photon polymerization based DLW processes combined with electroplating, which requires an overly complicated connected structure. Our new method allows the freedom to create disconnected and/or connected structures. Figure 5.24 is an example of a complex 3D pattern we fabricated. The unit cell of this 3D structure is comprised of 6 silver rings with diameter of 8 μm on each face of a cubic cell. Three layers were fabricated with 16 μm spacing between the layers. Center to center unit cell distance is also 16 μm. Each layer consists of 16 (4 × 4) unit cells. Figure 5.24 (b), (c) and (d) are optical images taken at each focal plane as indicated in (a). With further fine tuning of the writing parameters, the silver agglomerates on each edge of the cubic cell can be removed. This was due to two silver rings overlapping at each edge.

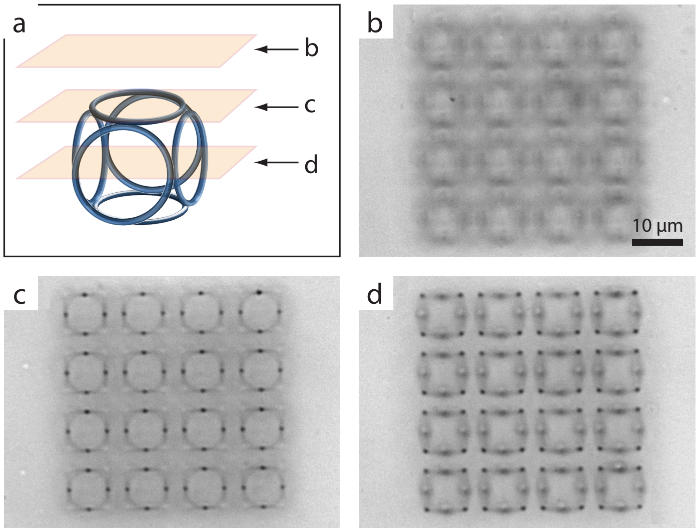

Figure 5.24: Illustration and in-situ optical images of a direct laser written complex 3D structure. (a) Illustration of a unit cell from a 4 × 4, 3 layer 3D structure. (b), (c) & (d) In-insitu images of the structure focused at b, c and d planes, respectively. b,c and d positions are shown in illustration (a). A video of a full image stack can be seen in reference [161].

5.4 Conclusion

We first demonstrate high-resolution 3D disconnected silver nanostructure fabrication in a PVP matrix through multiphoton absorption of ultrashort laser pulses. This chemistry allows fabrication of 300-nm silver structures and the PVP matrix has potential use for optical devices that work in 1-2.5 μm and 3.5-5.5 μm ranges. The second chemistry method takes advantage of unique gelatin properties to yield higher resolution (sub-100nm) 3D silver nanostructures in a flexible gelatin matrix. The doped-gelatin matrix enables bulk 3D metal nanofabrication over large volumes (tens of cubic millimeters in size). This method may enable the realization of tunable, bulk metal-dielectric optical and THz metamaterial devices that were not feasible with previous techniques.

Compared to other 3D fabrication techniques that yield metal nanostructures [63–65,68,144,145,156], this process only requires readily available chemical reagents, a simple experimental setup, and a single fabrication step. By using a higher-NA objective and modifying the chemistry we expect it will be possible to further increase the resolution and fabrication speed and to extend the method to other metals, such as gold. The approach presented in this chapter may permit the creation of new types of metamaterials and other photonic devices that cannot be made using current fabrication techniques [18].

Chapter 6

Fabrication of 2D graphite

Graphene has recently emerged as one of the most versatile materials ever discovered due to its extraordinary electronic, optical, thermal, and mechanical properties [33, 34]. However, device fabrication is a well-known challenge [33, 34]. The conventional techniques that were discussed in Chapter 2 have several limitations and therefore, novel fabrication methods are required to realize large-scale integration of graphene-based devices. Here, we demonstrate direct writing of reduced graphene oxide 2D patterns using femtosecond-laser irradiation at 800 nm. We perform a systematic study of the reduction process of graphene oxide to graphene by varying both the laser fluence and the repetition rate. Our observations show that the reduction process has both thermal and non-thermal components, and the reduced patterns written through only non-thermal mechanism may produce higher quality structures. By using pulse trains of low-kHz repetition (rep) late to limit thermal components we may be able to achieve a high degree of flexibility and control in the fabrication of graphene layers.

6.1 Materials & Method

Materials

170-nm layer graphene oxide (GO) films on 2-inch diameter glass substrate were purchased from Graphene Laboratories Inc.. For 4-probe conductivity measurements, gold contacts were patterned using optical lithography and deposited using Sharon EE-3, and Denton EE-4 electron beam evaporators.

Laser fabrication

Two different lasers were used to test various laser parameters. A Femtosource Ti:sapphire laser centered at 795 nm was used on a CW mode and on a pulsed mode at 11-MHz repetition rate, with a pulse duration of 300 fs. A Coherent Ti:sapphire laser centered at 794 nm was used for 80-MHz, 10-kHz and 250-KHz repetition rate experiments, with pulses durations of 125-, 180- and 400-fs for the irradiation process. Different laser spot sizes were tested using lenses with various focal lengths and various objectives. To draw lines and patterns, a high-precision Aerotech 3-axis translation stage was used to select the region to be exposed and was translated at 100 μm/s.

Characterization

Optical microscopy was carried out for post-fabrication characterization of structure dimensions. Scanning electron microscopy (SEM) was performed using a Zeiss ULTRA microscope, with an in-lens detector. Atomic force microscopy (AFM) was done with Asylum-2 MFP-3D Coax AFM. X-ray photoelectron spectroscopy (XPS) is surface spectrometry equipment that is used to determine elemental chemical compositions. Using Thermo Scientific K-Alpha XPS, the laser reduced GO samples were compared with the un-treated control GO films to identify the concentration of the remaining oxygen. To test the quality of the reduced GO structures, conductivity measurements were made with Signatone S-1160 4-probe station.

6.2 Results & Discussion

6.2.1 Results

We utilize a simple method to determine the reduction threshold of graphene oxide. We irradiate graphene oxide films with different laser parameters. Continuous wave (CW) and a train of femtosecond pulses with varying pulse widths were tried. We expect the absorptive properties of the film to change as the film is reduced to graphite. By monitoring the transmission of the laser beyond the sample, we observe changes in transmission that indicate material modification. Figure 6.1 through Figure 6.10 show how transmission changes as different laser powers were tested with respect to its total irradiated time. Two regimes are identified. In the first regime, transmission decreases as a function of time elapsed indicating a modification in the material to absorb more light. As the laser power increases the transmission saturates. At even higher laser powers the transmission begins to increase again, indicating thinning of the material. We use the term *energy threshold* for the laser power required for the transmission plot to show a saturating behavior. After laser modification, the laser irradiated spots were observed using an optical microscope. Results from various laser parameters are presented first and a more detailed discussion will follow.

CW laser irradiation

The laser spot size for CW laser irradiation was 35 μm in diameter. Figure 6.1 is a plot of transmission vs. time at various laser powers. The left plot indicates the fist regime where transmission decreases until saturation. The plot on the right is the other regime where transmission starts increasing again. We observe the energy threshold of the film to be around 90 mW. Figure 6.2 shows optical images of the laser irradiated spot. The diameter of the laser modified area for a 100-mW irradiated sample is about 50 μm, which is larger than the original laser spot size. This indicates material modification due to thermal effects. At 90 mW, we start seeing darker regions in the middle of the spots indicating formation of graphene layers.

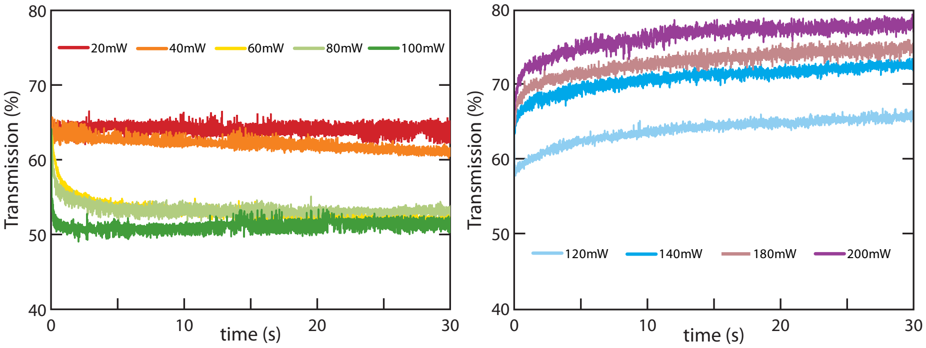

Figure 6.1: Transmission vs. time plots with a CW laser at various average powers. The left plot indicates the first regime prior to transmission saturation and the right plot indicates the second regime.

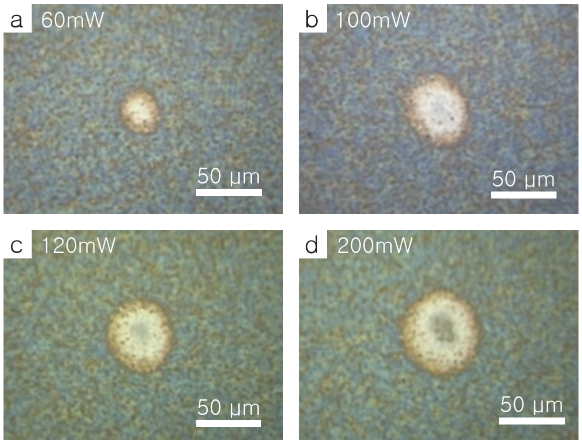

Figure 6.2: Optical images of CW laser irradiate spots at various laser powers.

76-MHz laser irradiation

For the 76MHz laser irradiation experiment, a pulse duration of 180 fs and a laser spot size of 35 μm (in diameter) was used. Figure 6.3 is a plot of transmission vs. time at various laser powers. We observe the energy threshold of the film to be around 60 mW. Figure 6.4 shows optical images of the laser irradiated spot. The diameter of the laser modified area is about 40 μm, which is comparable to the original laser spot size. Likewise, we start observing darker regions in the middle beginning at laser powers of 60 mW.

250-kHz laser irradiation

Two different pulse durations were tested; one of 400 fs and the other at 125 fs. The laser spot size used was 35 μm in diameter for both pulse durations. Figure 6.5 and Figure 6.7 are plots of transmission vs. time at various laser powers for pulse durations of 400 fs and 125 fs, respectively. We observe the energy threshold of the film to be around 30 mW for 400-fs pulse durations and 15 mW for 125-fs pulse durations.

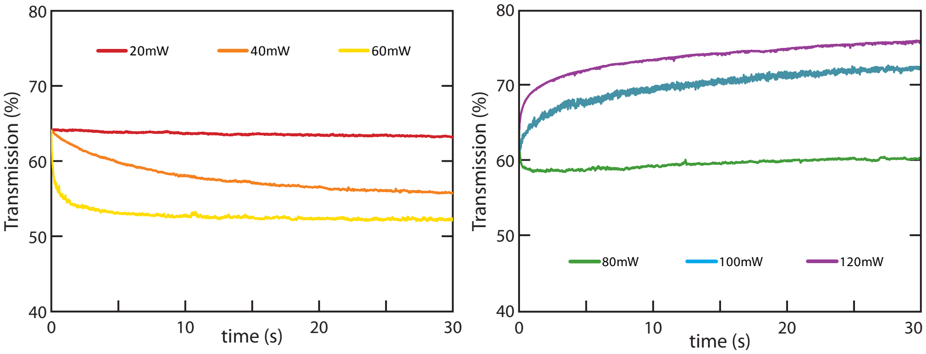

Figure 6.3: Transmission vs. time plots with a 76-MHz laser at various average powers. The left plot indicates the first regime prior to transmission saturation and the right plot indicates the second regime.

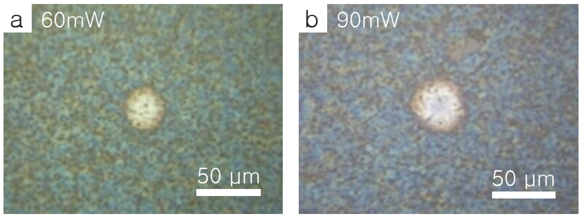

Figure 6.4: Optical images of 76-MHz laser irradiate spots at various laser powers.

Figure 6.6 and Figure 6.8 show optical images of the laser irradiated spot for pulse durations of 400 fs and 125 fs, respectively. The shape of the laser beam during these experiments was not a perfect Gaussian and therefore the irradiated spots exhibit an elliptical shape. The averaged diameter of the laser modified area is about 40 μm for a 400-fs pulse duration and 35 μm for a 125-fs pulse duration. Likewise, darker areas start appearing at laser powers corresponding to energy thresholds and can be seen in the 60-mW and 10-mW optical images respectively.

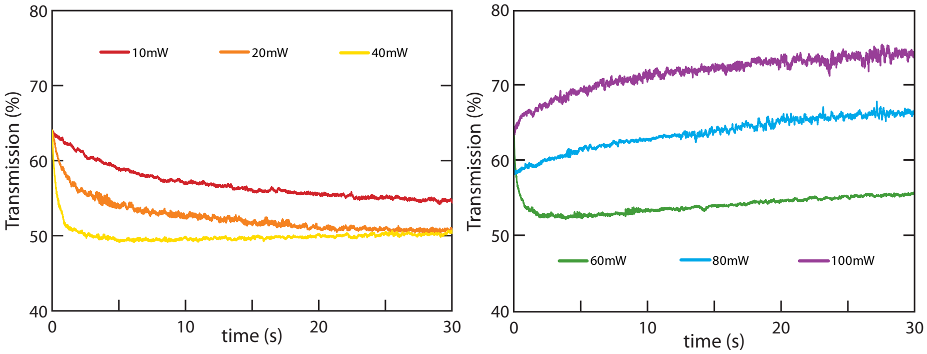

Figure 6.5: Transmission vs. time plots with a 250-kHz laser at various average powers (pulse duration is 400 fs). The left plot indicates the first regime prior to transmission saturation and the right plot indicates the second regime.

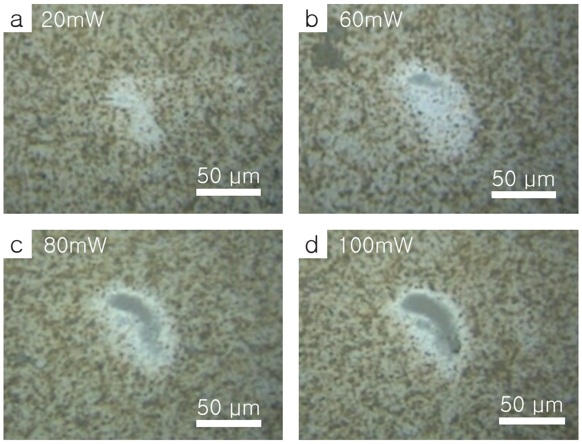

Figure 6.6: Optical images of 250-kHz laser irradiate spots at various laser powers (pulse duration is 400 fs).

10-kHz laser irradiation

For a 10kHz experiment, a pulse duration of 180 fs and a laser spot size of 150 μm in diameter was used. Figure 6.9 is a plot of transmission vs. time at various laser powers. We observe the energy threshold of the film to be around 10 mW. Figure 6.10 shows optical images of the laser irradiated spot. The diameter of the laser modified area is about 40 μm, which is close to a quarter of the original laser spot size. Likewise,

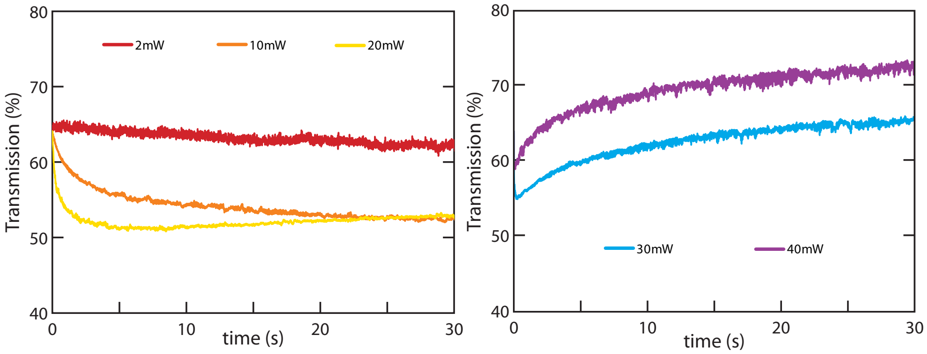

Figure 6.7: Transmission vs. time plots with a 250-kHz laser at various average powers (pulse duration is 125 fs). The left plot indicates the first regime prior to transmission saturation and the right plot indicates the second regime.

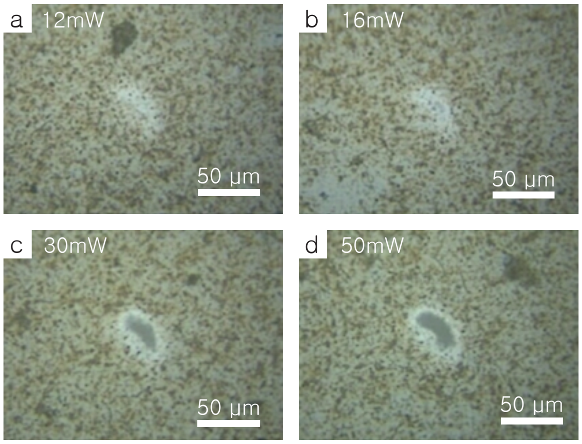

Figure 6.8: Optical images of 250-kHz laser irradiate spots at various laser powers (pulse duration is 125 fs).

darker area starts appearing at 10 mW.

Atomic force microscope (AFM) was used to further probe the structural properties of the laser irradiated spots. Figure 6.11 is an AFM image and a surface height plot of its cross-section across the middle area for a 76-MHz laser irradiated sample at 90 mW. The laser irradiated area is thinner which may indicate the reduction of GO layers into graphene sheets.

To determine whether reduced GO structures were successfully fabricated, we

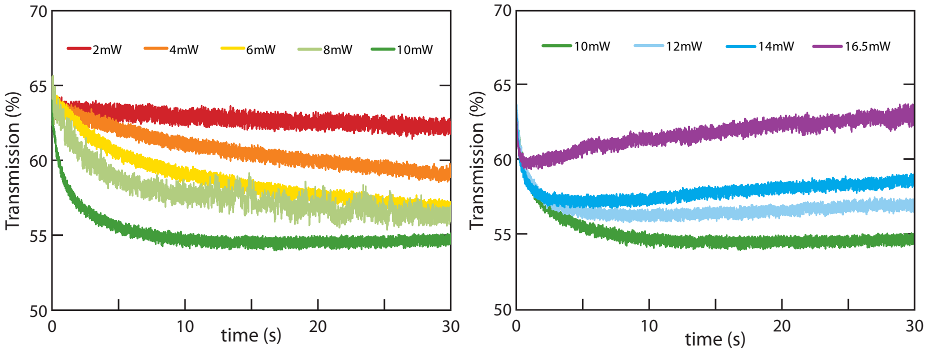

Figure 6.9: Transmission vs. time plots with a 10-kHz laser at various average powers. The left plot indicates the first regime prior to transmission saturation and the right plot indicates the second regime.

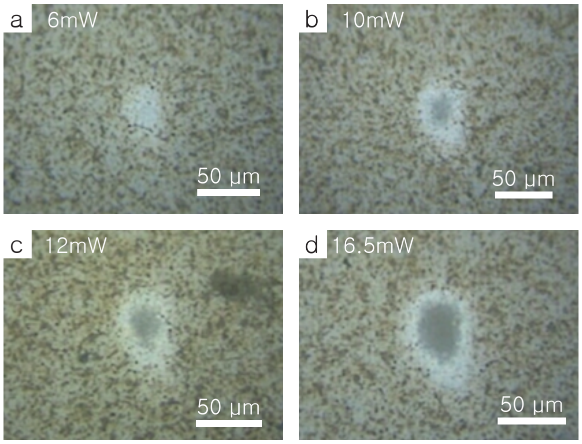

Figure 6.10: Optical images of 10-kHz laser irradiate spots at various laser powers.

perform XPS measurements. Figure 6.12 show XPS results of a 140-mW CW laser irradiate sample. The irradiated area was approximately 50-μm in diameter. The theoretical resolution (spot size of X-ray) of our XPS was 40 μm. The actual X-ray spot size is estimated to be larger. Therefore, we expect some signal from the unirradiated GO area to be also mixed in with our experiment results. The decrease in the C-O bonding peak for the reduced GO sample in the left plot of Figure 6.12 indicates that our laser fabrication technique was able to reduce the graphene oxide

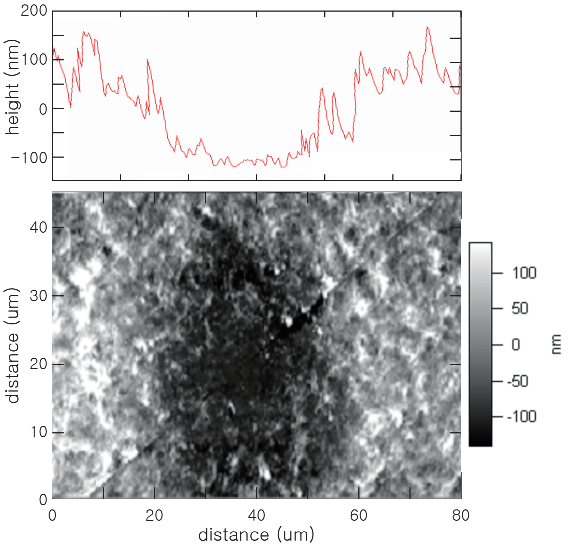

Figure 6.11: AFM results of a 76-MHz laser irradiate area. The top plot is a height trace across the middle section and the bottom is a height map (The diagonal line in the map is from an imaging software error. It does not interfere with the AFM results.)

layer. It is likely that the C-O and the C=O bonding peaks are from the surrounding unirradiated areas, due to equipment limitations as mentioned before. In addition, we observe a peak shift in the C-C bonding signal to a lower energy. While in XPS it is not easy to fit individual peaks for sp2 and sp3 arrangements respectively, the sp2 configuration in general has a slightly lower binding energy than the sp3. The shift seen in our result suggests that the laser fabricated reduced GO structure may have a higher percentage of sp2 bonding which is a unique characteristic of a defect free and pure graphene structure. The plot on the right is a magnified version of the reduced GO peak.

Lastly, conductivity of these patterned 2D graphite structures was measured. Rectangular gold contacts were e-beam evaporated onto the sample for a 4 point probe measurement. Figure 6.13 is an SEM image with a 4 point probe schematic

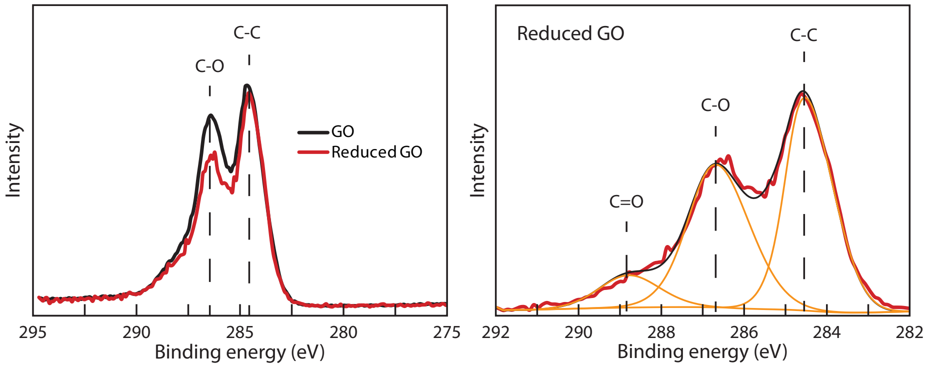

Figure 6.12: XPS results of a 140-mW CW laser irradiated sample. The left plot compares un-irradiated control sample with the irradiated sample and the right plot is a magnified view of the result.

on one of the graphite lines written at 10 μm/s. A rep rate of 10 kHz and a pulse duration of 200 fs were used to write the line. Scratches on the gold contacts are from the probes during the measurement. The laser spot size used was 5 μm and the produced line widths were around 2 μm.

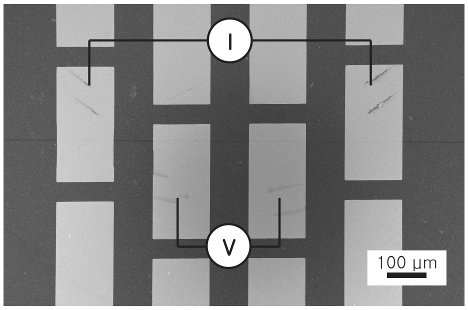

Figure 6.13: SEM image with a 4-point probe schematic. Each gold contact is 150 μm × 300 μm.

Figure 6.14 is an SEM image of one of the CW laser irradiated lines (shown between two gold contacts). A line that was wider than 3 μm was produced with a laser beam spot size of 1 μm.

Figure 6.15 is a plot of various resistances for direct laser written 2D lines. Control is the resistance of an unaltered GO sample. For the CW experiment, a spot

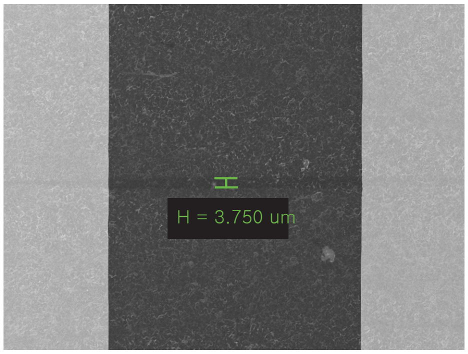

Figure 6.14: SEM image with a direct laser written 2D graphite line with a 35-mW CW laser at 10 μm/s.

size of 1 μm and writing speed of 10-100 μm/s at 34mW were used which produced 2-4-μm wide lines. The 11-MHz experiment also had a spot size of 1 μm with a writing speed of 100 μm at 32 mW and it resulted in 1-2-μm wide lines. For the 10-kHz experiment, a spot size of 5 μm and writing speeds 10-100 μm/s at 40 mW were used to produce 1-2-μm wide lines. The lines fabricated with the 10-kHz laser exhibit an increase in conductivity of 4 orders of magnitude when compared to the un-irradiated control sample.

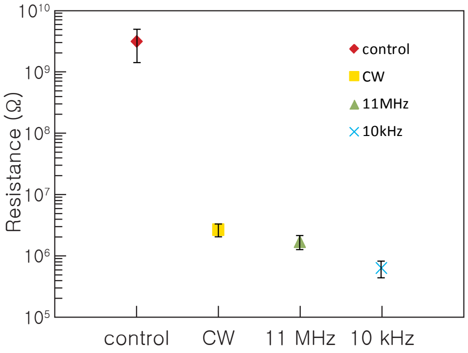

Figure 6.15: Resistances of various direct laser written lines. (Y-axis is on a log scale and x-axis lists the different types of lasers used.)

6.2.2 Discussion

Table 6.1 is a summary of the spot-laser-irradiation experiment results with respect to various laser parameters. We investigate the impact that laser pulse energy, repetition rate and pulse duration has on the reduction of graphene oxide. Spot size refers to the diameter of the initial laser spot size and sample size refers to the diameter of the laser modified area. Threshold peak intensity refers to the calculated peak intensity when the average laser power used equals the energy threshold values acquired from the plots in the previous section.

Table 6.1: Summary of spot-laser-irradiation experiment with various laser parameters.

	Pulse duration (fs)	Energy threshold (mW)	Spot size (d in μm)	Sample size (d in μm)	Threshold peak intensity (W/m^2)
CW	-	90	35	50	-
80 MHz	180	60	35	45	4.33075E+12
250kHz long pulse	400	30	35	40	3.11814E+14
250kHz short pulse	125	15	35	35	4.98902E+14
10kHz	180	10	150	40	3.1438E+14

A few interesting observations can be made. First, the threshold peak intensity increases as the rep rate gets lower and a magnitude of two orders difference in the peak intensity is found when comparing a 80-MHz and a 250-kHz with 400-fs pulse duration laser. This may indicate that CW and 80-MHz laser fabrications are dominated mostly by a thermal mechanism and a 250-kHz laser fabrication may involve both thermal and nonlinear components in the reduction of GO. Second, we notice that the affected area (sample size) is larger for a CW laser irradiated sample and gets smaller as shorter pulses are used. This can be another indication that using CW and low rep rate with long pulse duration lasers result in a thermal accumulation in the sample leading to larger modified areas. The sample size for a 10-kHz laser fabrication is approximately a quarter of the original laser spot size. Considering the fact that the rep rate used is more than 10 times lower than a 250kHz laser experiment, this may suggest that the 10-kHz laser irradiated spots are due to the purely nonlinear photoreduction mechanism rather than a mix of the two. Using a 10kHz laser, we were also able to obtain lines with a higher resolution than any other previously reported results[1] [104–106, 162]. Furthermore our conductivity measurements also indicate that the patterned graphite structures with a 10-kHz laser has the best quality. The purely nonlinear photoreduction process may result in a better resolution and minimum thermal degradation of the material. Lastly, comparing the transmission vs. time plots from the previous section for various laser parameters, we notice that it takes a longer time for a transmission plot to reach saturation for lower rep rates. By having a slower and more steady initial reaction rate, this may allow for a either more efficient or more controlled initial reduction process during an actual, scaled-up device manufacturing procedure.

---

[1] The highest resolution was achieved with respect to the laser beam spot size used. With a 5 μm beam, we obtained line widths of 1-2 μm.

6.3 Conclusion

In summary, we investigate the reduction of graphene oxide using femtosecond laser irradiation. We demonstrate direct laser writing of reduced graphene oxide structures and explore the reduction process using various repetition rates from a continuous wave laser to lasers with rep rates in the kHz regime. By comparing energy thresholds required for graphene oxide modification and the resolution of the structures, we can decouple thermal versus non-thermal reduction. Graphene formation through nonlinear process may give more control over resolution and quality of the reduced graphene oxide structures. This study provides us with new insight into the reduction process and facilitates the optimization of laser writing of graphene structures.

It has only been about 10 years since the original discovery of graphene [32,88]. Finding reliable fabrication methods and discovering the true chemical structure of graphene oxide and many other graphene derivatives is still an ongoing challenge [83]. More research needs to be done in various aspects, from fundamental structural and chemical studies to effective fabrication methods. Through further research, we expect the production of cheap GO films coupled with a low rep rate laser lithography may offer a preferred route to generating large-scale graphene integrated devices for the future.

Chapter 7

Summary & Future directions

We investigate a novel methodology of direct laser writing metal-dielectric systems and 2D graphite systems. We use the technique of ultrafast laser micromachining combined with photoreduction to: 1) gain access to inside the bulk with precise architectural control with nanometer resolution, and 2) induce chemical reactions to create metal and graphene structures. To conclude, this chapter summarizes the findings in this thesis and provides future research directions.

7.1 Summary

In Chapter 3, we discuss various laser and chemical parameters that affect the direct laser writing process and offer insight toward designing more complex metal-dielectric composite systems and producing higher quality graphene structures. We identify that the use of alcohols as solvents can provide catalytic pathways to faster reduction of silver ions. A careful choice of polymers is made to provide a transparent supporting matrix and provide effective control of silver growth. We hypothesize a possible photoreduction mechanism from C=O bonds in graphene oxide and suggest an effective fabrication method through decoupling thermal and non-thermal effects.

In Chapters 4 and 5, we present experimental methods and the resulting structures of 2D patterned silver crystals and embedded 3D silver nanostructures. We use a chemical mixture of silver nitrate, ethanol, deionized water, and PVP to initiate growth of silver seed nanoparticles for direct laser writing of silver crystals. We omit ethanol when fabricating 3D silver nanostructures that are embedded in a polymer matrix. By removing ethanol from the mixture we get rid of the need to dissolve the polymer layer and let it serve the role as a supporting matrix. To fabricate higher resolution structures, we use gelatin instead of PVP to provide more effective control in the growth of silver structures leading to a longer shelf life of the matrix. Gelatin also allows for a streachable matrix that can be used for tunable device applications.

Figure 7.1 compares values of n and k for various chemistries used in Chapters 4 and 5. We observe a decrease in the k values as we omit the polymer and change the polymer from PVP to gelatin. Also a color difference in the doped matrix (due to silver nanoparticles) can be seen in Figure 7.2.

We confirm the silver content and analyze the fabricated structures by using various techniques such as SEM, EDS, EBSD and TEM. We conduct optical characterization studies to identify the transparent (low loss) window for each chemistry method. By choosing the appropriate chemistry, one can fabricate a metamaterial device for a vis-near IR, mid IR, or THz regime. Lastly, preliminary results in appli-

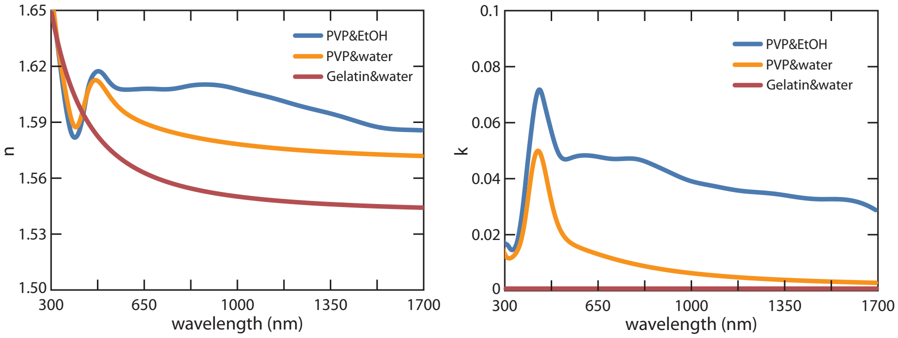

Figure 7.1: Summary plots of n and k. Features around 420 nm are from silver nanoparticles.

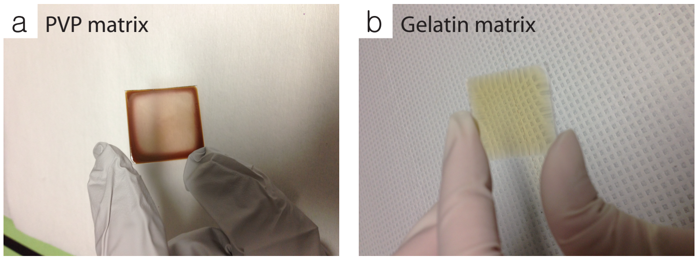

Figure 7.2: Images of samples ready for laser fabrication. (a) doped PVP matrix (brown color is due to silver nanoparticles), (b) doped gelatin matrix. (Yellowish tint is from the natural color of bovine gelatin)

cations such as 3D diffraction grating and zone plates are presented.

In Chapter 6, we show direct laser writing of 2D graphite (multi-layer graphene) structures. We control the thermal vs. non-thermal reduction mechanism by varying the laser repetition rate, pulse duration, and laser fluence. We confirm successful reduction of graphene oxide to graphene layers through optical images, XPS, and conductivity measurements. We conclude that higher resolution and lower resistivity graphite structures can be obtained through the use of lower repetition rate laser parameters.

7.2 Future directions

7.2.1 Chemical studies

3D metallic structures in a dielectric matrix

Our fabrication technique to write metal structures embedded in a polymer matrix provides us with a freedom to choose different types of polymers and modify its composition. Responsive polymers that change their characteristics (whether optical, electrical, and/or mechanical) depending on the ambient environment may allow us to fabricate tunable metamaterials with various functionalities.

One polymer for further investigation is poly acrylic acid (PAA). PAA is an anionic polyelectolyte polymer that is sensitive to pH with the ability to absorb and retain water and swell to many times its original volume [163–165]. By incorporating PAA we may be able to achieve tunable matrices that respond to different humidity levels. Figure 7.3 shows our preliminary results of direct laser writing in a PAA sample doped with silver ions. A mixture of 0.206 g of PAA, 8mL of DI H_2O and 0.21 g of $AgNO_3$ was tested. The same method and laser setup was used as in Chapters 4 and 5. (A schematic of the laser setup is shown in Chapter 4. The laser power was unstable during this experiment, and the concentrations have not been optimized, but preliminary results show the possibility of direct laser writing silver structures using PAA.) Figure 7.3(a) is an in-situ optical image of a laser patterned area. Some bubbles in the matrix are seen due to the un-optimized chemistry. Figure 7.3(b) and (c) are SEM images of the written silver dots and (d) is an EDS result from a line-scan of the dotted line in Figure (c). The line EDS result confirms a high content of silver in the fabricated dot structures.

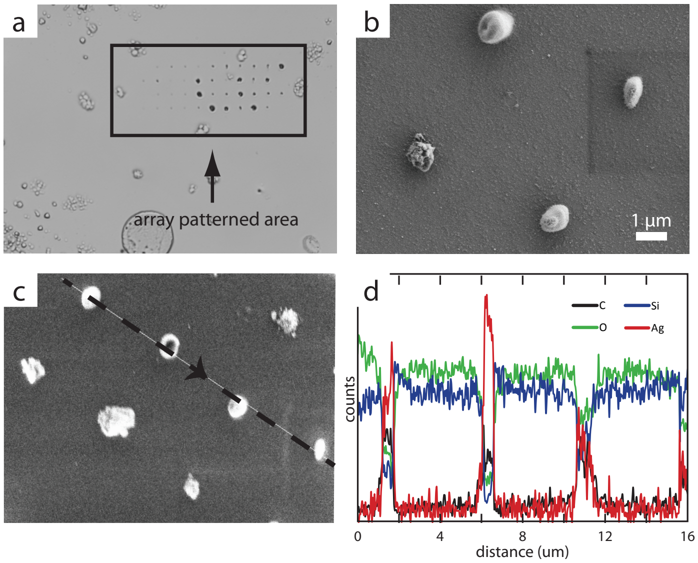

Figure 7.3: Preliminary results of PAA. (a) An in-situ optical image of the laser patterned area, (b) & (c) SEM images of the written silver dots, (d) An EDS result of a line-scan from the dotted line in figure (c).

Transmission measurement in Figure 7.4 shows effective control of initial silver nanoparticle growth and a good transmission window from 300 nm to 2.5 μm.

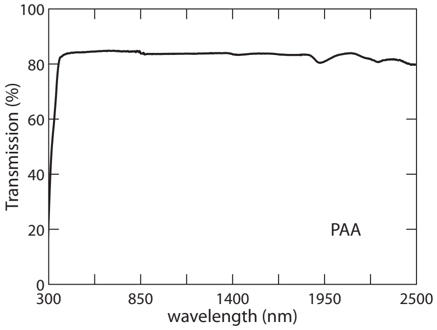

Figure 7.4: Transmission vs. wavelength of doped PAA matrix

In Chapter 3 we establish that the length of the polymer chain and the content of electron affinity groups are crucial to providing better control in the growth of silver structures. (This is one of the reasons why we utilize gelatin instead of

PVP to fabricate higher resolution structures.) However, in addition to looking into high molecular weight polymers with longer chains, consideration of steric effects and packing of polymer chains may also be very important. Figure 7.5 shows images of doped PVP matrices ready for fabrication. Figure 7.5(a) was made with a 58,000 g molecular weight (M.W.) PVP (as in the method described in Chapters 4 and 5) and (b) was made with a 360,000 g M.W. PVP that has more than 6 times longer chains than the 58K M.W. PVP. As seen in the color difference in Figure 7.5, it supports our hypothesis that longer chains restrain growth of silver particles more effectively. However, the 360K PVP sample shows some crystallizing effects. When we raise the sample temperature to 150 °C, we observe an increase in transmittance as in Figure 7.6. Polymer orientation is an important problem in many polymer applications because it can change the optical and mechanical properties of the film [166, 167]. We suspect that by increasing the temperature to 150 °C, we bring the polymer sample beyond its glass transition temperature allowing it to be more transparent and fluid-like which results in free ion-movement leading to formation of silver nanoparticles. When we bring the temperature down to room temperature, we observe that our sample has turned into a metallic-looking film due to complete reduction of the silver ions and shows extremely low transmission. (Gelatin on the other hand has a broad molecular weight and has varying lengths of polymer chains from hydrolysis of collagen.)

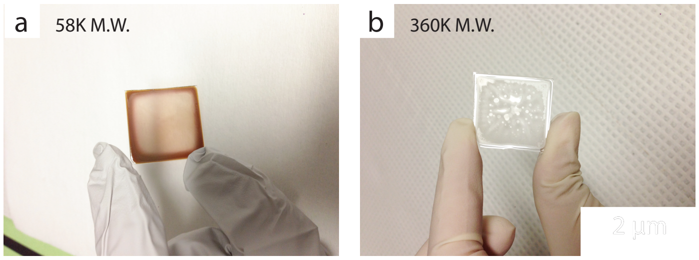

Figure 7.5: Images of doped polymer matrices ready for fabrication. Made with: (a) 58K g M.W. PVP and (b) 360K g M.W. PVP

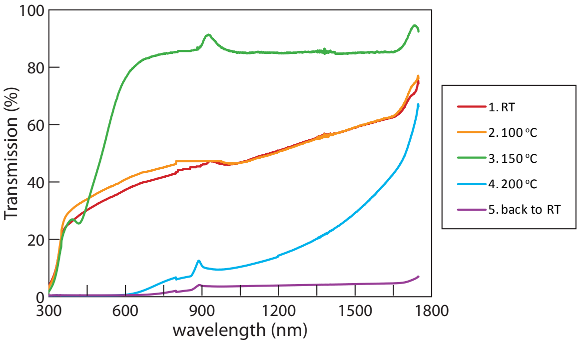

Figure 7.6: Transmission vs. wavelength plot of doped 360K g M.W. PVP matrix at various temperatures. Temperature was raised to 200 °C then was lowered back to room temperature (RT).

2D graphite fabrication

In Chapter 6 we conduct our experiment with a 170-nm graphene oxide film. If the thickness of one layer of graphene oxide is ∼10 Å [82,126], then our 170-nm graphene oxide film is comprised of ∼170 layers. To produce one or a bi-layer graphene instead of 2D graphite, we can start with thinner graphene oxides films as our beginning material. More analysis and characterization need to be carried out with cross-sectional area studies of the sample to acquire more information.

Furthermore, since the exact structure and reduction mechanism of graphene oxide remains unknown, there is a countless number of possible experiments that can be done. Many experiments are being conducted which try various ways to produce higher quality graphene layers. One example is where titanium dioxide (TiO_2) nanoparticles are added to graphene oxide as an additional photocatalyst to aid the reduction process [83, 103]. Other interesting approaches include integrating additional metal nanowires to graphene films to improve electrical conductivity [94].

7.2.2 Fabrication & Characterization of devices

We expect that the flexibility and patternability of our technique will enable fabrication of complex 3D photonic structures such as a perfect lens, waveguides, resonators, gratings, and photonic crystals. Also with further optimization of the graphene oxide reduction process, our method may enable direct patterning of pristine graphene structures for applications such as graphene transistors, integrated circuits, energy storage, and solar cells.

Development of functional metamaterials

Further fine tuning of the technique will allow fabrication of higher resolution structures and 3D isotropic metamaterials (as theoretically demonstrated by Guney [18]). Unlike previous direct laser writing techniques where connectivity between neighboring unit cells is inevitable, our technique does not require a inter-connected design, which gives more freedom in designing various metamaterials. Laser beam engineering (as mentioned in Chapter 3) may also facilitate the fabrication of more complex structures.

We expect the production of cheap GO films coupled with laser lithography may offer a preferred route to generating very large-scale graphene integrated devices in the future. Compared to the previous conventional methods where production of random strips of graphene or only a large 2D sheet of graphene was possible, our technique allows precise patterning of graphene layers. With our technique, we may be able to produce 2D graphene metamaterials or graphene circuits in the future.

Our fabrication techniques can also be applied to other material system, in addition to metal and graphene structures. Materials that go through a photoreduction process and can be used in future devices may be worth investigating. We believe that, in the near future, we will be able to tune and design the optical and electronic response of materials through ultrafast laser direct writing.

Material characterization

For the development of three dimensional dispersion-engineered metamaterials, methods of optical characterization are also cruicial. A characterization system that includes the capability to measure transmission and reflection amplitudes as well as phases as a function of angle of incidence and position on the sample will be necessary for a thorough analysis. Several systems may need to be developed in order to operate at various ranges of wavelengths. (Our PVP matrix allows devices in the near-IR and mid-IR wavelengths and the gelatin matrix allows near-IR and THz devices.) Advanced variable angle spectroscopic ellipsometers can be used or home-built systems may be necessary. Once the optical characterizations are made, numerical techniques can be applied to extract the effective permittivity and permeability of the fabricated sample, or the experimental values can be compared with the theoretical values obtained from FDTD simulations. The latter comparison will also allow us to characterize properties of the fabrication process such as precision, accuracy, structure roughness, and reliability of the fabrication method.

Scalability & Device packaging

Femtosecond-laser patterning is a desirable method to design and fabricate innovative materials because of its potential as a cheap, reliable, and scalable technique. As mentioned in Section 3.1.1, with SLMs and pulse shaping techniques we can obtain a multiple complex beam profile to generate many structures simultaneously at a faster speed. One typical fabricated 2D array of dots had an average size of 468 nm with a standard deviation of 63.9 nm. Through the use of pulse shaping techniques, more stable laser systems and adaptive optics with feedback loops, we can achieve a higher uniformity in the structures. Micro-lens arrays may also be incorporated to scale up the process. For fabrication of commercializable devices, we should also consider the next steps after laser-fabrication. Gelatin matrix and unpatterned graphene oxide have hygroscopic properties and therefore, would require water-proof packaging. To use the PVP matrix for mid-IR applications, a robust substrate will be needed due to its brittleness. Also UV-coatings will be necessary to prevent photoreduction of unreacted silver ions in the matrix. In the future, we hope our method can help move research from the lab to producing innovative commercial products.

Appendix A

Z-scan technique

To gain a further understanding of the nonlinear absorption mechanism that occurs during the fabrication process, we can perform a Z-scan analysis on our sample. A Z-scan technique (also known as nonlinear transmittance measurements) is a simple experimental method to measure nonlinear absorption processes (specifically the nonlinear index n_2 and the nonlinear absorption coefficient α) and unlike other nonlinear absorption measurement methods, it is not restricted to fluorescent materials. [168, 169]. Figure A.1 is a schematic of our open aperture Z-scan setup.

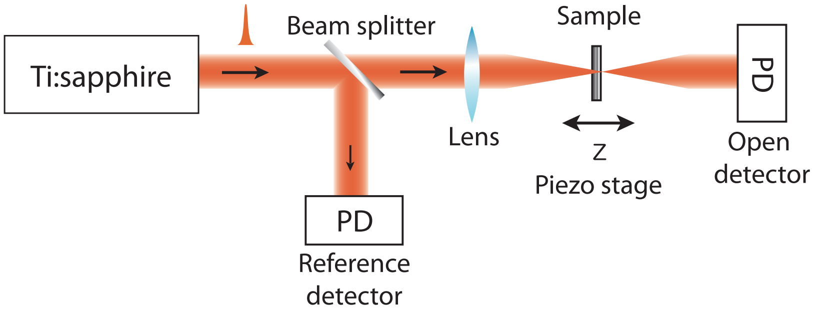

Figure A.1: Schematic of an open-aperture Z-scan technique.

We use an open aperture Z-scan method where a normalized transmittance in the far field is measured as our sample is scanned in the Z-axis through the focal plane of a focused Gaussian beam. Since nonlinear absorption is strongest at the focus, a sharp dip occurs when transmission is plotted as a function of distance. By comparing the obtained plot with theoretically fitted curves of two-, three- or four-photon absorption, we can determine the nonlinear absorption properties of our sample [168]. The theoretically fitted transmission vs. distance plots are shown in Figure A.2. (Refer to reference [168] for the theoretical model.)

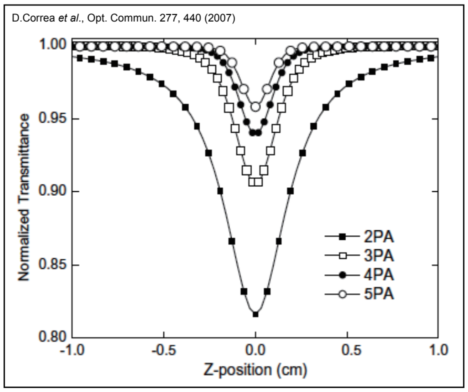

Figure A.2: Z-scan curves for 2, 3, 4 and 5-photon-absorptoin obtained with theoretical nonlinear absorption equations. Adapted from reference [168].

As a first step to verify whether PVP undergoes a nonlinear absorption process (i.e, whether PVP has a large nonlinear absorption cross-section), we perform simple absorption and threshold measurements while maintaining the samples at the focal point on the Z-axis. We measure power out (behind the sample) as we increase the laser input power. We prepare the sample by dissolving 0.206 g of polyvinylpyrrolidone (PVP) in 8 mL of DI water. Figure A.3 shows power out vs. power in plots of the PVP sample measured with two different laser parameters.

A 800-nm laser with pulse durations of 1 ps (low peak intensity) and 60 fs (high peak intensity) were tested on the PVP solution. The average laser power was

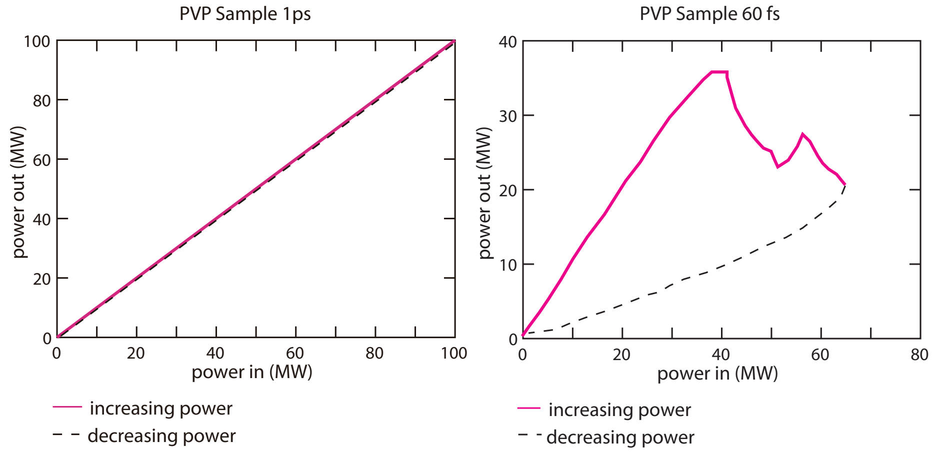

Figure A.3: P_{out} vs. P_{in} plots for 800-nm pulsed laser with 1-ps pulse duration (left) and 60-fs pulse duration (right).

slowly increased (pink trace) and then lowered back to zero (black dashed trace). We observe no change in the transmittance (power out/power in) at any laser power for the sample irradiated with 1-ps pulses (low peak intensity). However, we observe a drop in transmittance once the laser power reaches ∼40 mw for the sample irradiated with 60-fs pulses (high peak intensity). Since multiphoton absorption occurs in a volume surrounding the intensity peak above the threshold for nonlinear absorption (as discussed in chapter 3), we can establish that PVP goes through a multiphoton absorption process instead of a linear absorption process. In chapter 3, we also confirm the many linear absorption peaks of PVP around and below 266 nm. Therefore we expect this mechanism to be a 3-photon or a 4-photon absorption process.

For the z-scan measurement, the laser power and pulse duration is fixed but the sample is translated in the z-direction. Figure A.4 shows a preliminary z-scan result for the PVP solution. We observe a dip in the transmittance as expected, however the signal to noise ratio was low and would require multiple measurements to confirm the result.

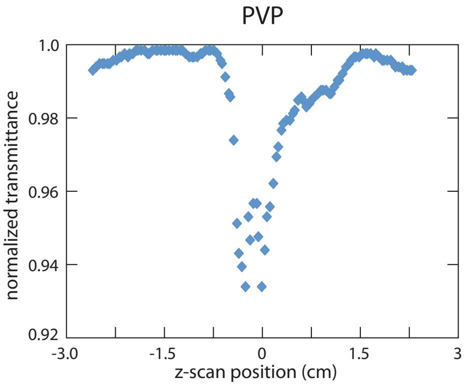

Figure A.4: Preliminary Z-scan absorption plot of PVP in DI water.

Although these are preliminary results, our threshold measurements and the Z-scan plot seem to confirm the existence of multi-photon absorption in PVP solutions. For more detailed analysis, future work will involve obtaining more Z-scan measurements using a flow cell configuration (to omit possibility of material degradation) and using a shorter wavelength pulsed laser to induce a 2-photon absorption instead of 3- or 4-photons to increase signal-to-noise ratio. We expect that a deeper understanding of the fabrication mechanism can be acquired with a thorough Z-scan analysis.

Bibliography

[1] J.D. Joannopoulos, Pierre R. Villeneuve, and Shanhui Fan, Nature **386**, 143 (1997).

[2] David J Norris, Nature materials **6**, 177 (2007).

[3] Jes Broeng, Dmitri Mogilevstev, Stig E. Barkou, and Anders Bjarklev, Optical Fiber Technology **5**, 305 (1999).

[4] Markus Deubel, Georg von Freymann, Martin Wegener, Suresh Pereira, Kurt Busch, and Costas M Soukoulis, Nature materials **3**, 444 (2004).

[5] Georg von Freymann, Alexandra Ledermann, Michael Thiel, Isabelle Staude, Sabine Essig, Kurt Busch, and Martin Wegener, Advanced Functional Materials **20**, 1038 (2010).

[6] Rick C. Schroden, Mohammed Al-Daous, Christopher F. Blanford, and Andreas Stein, Chemistry of Materials **14**, 3305 (2002).

[7] Kevin a Arpin, Mark D Losego, Andrew N Cloud, Hailong Ning, Justin Mallek, Nicholas P Sergeant, Linxiao Zhu, Zongfu Yu, Berç Kalanyan, Gregory N Parsons, Gregory S Girolami, John R Abelson, Shanhui Fan, and Paul V Braun, Nature communications **4**, 2630 (2013).

[8] Lindsey a Ibbotson and Jeremy J Baumberg, Nanotechnology **24**, 305301 (2013).

[9] D R Smith, J B Pendry, and M C K Wiltshire, Science **305**, 788 (2004).

[10] J B Pendry, D Schurig, and D R Smith, Science **312**, 1780 (2006).

[11] Vladimir M. Shalaev, Nature Photonics **1**, 41 (2007).

[12] Dr Smith, Wj Padilla, Dc Vier, Sc Nemat-Nasser, and S Schultz, Physical review letters **84**, 4184 (2000).

[13] R a Shelby, D R Smith, and S Schultz, Science **292**, 77 (2001).

[14] Jason Valentine, Shuang Zhang, Thomas Zentgraf, Erick Ulin-Avila, Dentcho a Genov, Guy Bartal, and Xiang Zhang, Nature **455**, 376 (2008).

[15] Anthony J Hoffman, Leonid Alekseyev, Scott S Howard, Kale J Franz, Dan Wasserman, Viktor a Podolskiy, Evgenii E Narimanov, Deborah L Sivco, and Claire Gmachl, Nature materials **6**, 946 (2007).

[16] G Dolling, M Wegener, C M Soukoulis, and S Linden, Optics letters **32**, 53 (2007).

[17] Michael S Rill, Christine E Kriegler, Michael Thiel, Georg von Freymann, Stefan Linden, and Martin Wegener, Optics letters **34**, 19 (2009).

[18] Durdu O Güney, Thomas Koschny, and Costas M Soukoulis, Optics express **18**, 12348 (2010).

[19] a N Grigorenko, Optics letters **31**, 2483 (2006).

[20] Henri J Lezec, Jennifer a Dionne, and Harry a Atwater, Science **316**, 430 (2007).

[21] Gunnar Dolling, Christian Enkrich, Martin Wegener, Costas M Soukoulis, and Stefan Linden, Science **312**, 892 (2006).

[22] Alexandra Boltasseva and Vladimir M. Shalaev, Metamaterials **2**, 1 (2008).

[23] Vladimir M Shalaev, Wenshan Cai, Uday K Chettiar, Hsiao-Kuan Yuan, Andrey K Sarychev, Vladimir P Drachev, and Alexander V Kildishev, Optics letters **30**, 3356 (2005).

[24] M. C. K. Wiltshire, Science **292**, 60 (2001).

[25] Martin W McCall, Akhlesh Lakhtakia, and Werner S Weiglhofer, European Journal of Physics **23**, 353 (2002).

[26] Huanyang Chen, C T Chan, and Ping Sheng, Nature materials **9**, 387 (2010).

[27] Costas M. Soukoulis and Martin Wegener, Nature Photonics **5**, 523 (2011).

[28] Justyna K Gansel, Michael Thiel, Michael S Rill, Manuel Decker, Klaus Bade, Volker Saile, Georg von Freymann, Stefan Linden, and Martin Wegener, Science **325**, 1513 (2009).

[29] Hongyou Fan, Kai Yang, Daniel M Boye, Thomas Sigmon, Kevin J Malloy, Huifang Xu, Gabriel P López, and C Jeffrey Brinker, Science **304**, 567 (2004).

[30] Na Liu, Hongcang Guo, Liwei Fu, Stefan Kaiser, Heinz Schweizer, and Harald Giessen, Nature materials **7**, 31 (2008).

[31] Ming Fu, Kundan Chaudhary, Jonathan G Lange, Ha Seong Kim, Jamie J Juarez, Jennifer a Lewis, and Paul V Braun, Advanced materials (Deerfield Beach, Fla.) 1 (2013).

[32] K S Novoselov, a K Geim, S V Morozov, D Jiang, Y Zhang, S V Dubonos, I V Grigorieva, and a a Firsov, Science **306**, 666 (2004).

[33] A K Geim and K S Novoselov, Nature materials **6**, 183 (2007).

[34] A. K. Geim, Science **324**, 1530 (2009).

[35] Qiaoliang Bao and Kian Ping Loh, ACS nano **6**, 3677 (2012).

[36] Qiaoliang Bao, Han Zhang, Bing Wang, Zhenhua Ni, Candy Haley, Yi Xuan, and Yu Wang, Nature Photonics **5**, 411 (2011).

[37] B. Obradovic, R. Kotlyar, F. Heinz, P. Matagne, T. Rakshit, M. D. Giles, M. a. Stettler, and D. E. Nikonov, Applied Physics Letters **88**, 142102 (2006).

[38] L Vicarelli, M S Vitiello, D Coquillat, a Lombardo, a C Ferrari, W Knap, M Polini, V Pellegrini, and a Tredicucci, Nature materials **11**, 865 (2012).

[39] Nicholas Petrone, Inanc Meric, James Hone, and Kenneth L Shepard, Nano letters **13**, 121 (2013).

[40] Xin Yan, Xiao Cui, Binsong Li, and Liang-shi Li, Nano letters **10**, 1869 (2010).

[41] Hyesung Park, Sehoon Chang, Matthew Smith, Silvija Gradečak, and Jing Kong, Scientific reports **3**, 1581 (2013).

[42] Jeremy T Robinson, F Keith Perkins, Eric S Snow, Zhongqing Wei, and Paul E Sheehan, Nano letters **8**, 3137 (2008).

[43] J. F. van Staden, R. Georgescu, R.-I. Stefan-van Staden, and I. Calinescu, Journal of the Electrochemical Society **161**, B3014 (2013).

[44] Ming Liu, Xiaobo Yin, Erick Ulin-Avila, Baisong Geng, Thomas Zentgraf, Long Ju, Feng Wang, and Xiang Zhang, Nature **474**, 64 (2011).

[45] Chenguang Liu, Zhenning Yu, David Neff, Aruna Zhamu, and Bor Z Jang, Nano letters **10**, 4863 (2010).

[46] Yan Wang, Zhiqiang Shi, Yi Huang, Yanfeng Ma, Chengyang Wang, Mingming Chen, and Yongsheng Chen, The Journal of Physical Chemistry C **113**, 13103 (2009).

[47] Ashkan Vakil and Nader Engheta, Science **332**, 1291 (2011).

[48] Nikitas Papasimakis, Zhiqiang Luo, Ze Xiang Shen, Francesco De Angelis, Enzo Di Fabrizio, Andrey E Nikolaenko, and Nikolay I Zheludev, Optics express **18**, 8353 (2010).

[49] Long Ju, Baisong Geng, Jason Horng, Caglar Girit, Michael Martin, Zhao Hao, Hans a Bechtel, Xiaogan Liang, Alex Zettl, Y Ron Shen, and Feng Wang, Nature nanotechnology **6**, 630 (2011).

[50] Seung Hoon Lee, Muhan Choi, Teun-Teun Kim, Seungwoo Lee, Ming Liu, Xiaobo Yin, Hong Kyw Choi, Seung S Lee, Choon-Gi Choi, Sung-Yool Choi, Xiang Zhang, and Bumki Min, Nature materials **11**, 936 (2012).

[51] Yong-Lai Zhang, Li Guo, Hong Xia, Qi-Dai Chen, Jing Feng, and Hong-Bo Sun, Advanced Optical Materials **2**, 10 (2014).

[52] Silvia Vignolini, Nataliya a Yufa, Pedro S Cunha, Stefan Guldin, Ilia Rushkin, Morgan Stefik, Kahyun Hur, Ulrich Wiesner, Jeremy J Baumberg, and Ullrich Steiner, Advanced Materials **24**, OP23 (2012).

[53] Rafael R Gattass and Eric Mazur, Nature Photonics **2**, 219 (2008).

[54] E N Glezer, M Milosavljevic, L Huang, R J Finlay, T H Her, J P Callan, and E Mazur, Optics letters **22**, 422 (1997).

[55] Chris B Schaffer, André Brodeur, and Eric Mazur, Measurement Science and Technology **12**, 1784 (2001).

[56] Kwang-Sup Lee, Dong-Yol Yang, Sang Hu Park, and Ran Hee Kim, Polymers for Advanced Technologies **17**, 72 (2006).

[57] Wojciech Haske, Vincent W Chen, Joel M Hales, Wenting Dong, Stephen Barlow, Seth R Marder, and Joseph W Perry, Optics express **15**, 3426 (2007).

[58] M. Göppert-Mayer, Annalen der Physik **18**, 466 (2009).

[59] Aleksandr Ovsianikov and Boris Chichkov, in *Nanoelectronics and Photonics: From Atoms to Materials, Devices, and Architectures*, edited by Anatoli Korkin and Federico Rosei (Springer New York, ADDRESS, 2008), p. Chapter 12.

[60] Christopher N LaFratta, John T Fourkas, Tommaso Baldacchini, and Richard a Farrer, Angewandte Chemie **46**, 6238 (2007).

[61] Michael S Rill, Christine Plet, Michael Thiel, Isabelle Staude, Georg von Freymann, Stefan Linden, and Martin Wegener, Nature materials **7**, 543 (2008).

[62] Tommaso Baldacchini, Anne-Cécile Pons, Josefina Pons, Christopher Lafratta, John Fourkas, Yong Sun, and Michael Naughton, Optics express **13**, 1275 (2005).

[63] Yao-Yu Cao, Nobuyuki Takeyasu, Takuo Tanaka, Xuan-Ming Duan, and Satoshi Kawata, Small **5**, 1144 (2009).

[64] Takuo Tanaka, Atsushi Ishikawa, and Satoshi Kawata, Applied Physics Letters **88**, 081107 (2006).

[65] A Ishikawa, T Tanaka, and S Kawata, Applied physics letters **89**, (2006).

[66] N. Takeyasu, T. Tanaka, and S. Kawata, Applied Physics A **90**, 205 (2007).

[67] Jin-Feng Xing, Xian-Zi Dong, Wei-Qiang Chen, Xuan-Ming Duan, Nobuyuki Takeyasu, Takuo Tanaka, and Satoshi Kawata, Applied Physics Letters **90**, 131106 (2007).

[68] Shoji Maruo and Tatsuya Saeki, Optics express **16**, 1174 (2008).

[69] C. Enkrich, F. Pérez-Willard, D. Gerthsen, J. F. Zhou, T. Koschny, C. M. Soukoulis, M. Wegener, and S. Linden, Advanced Materials **17**, 2547 (2005).

[70] Xiaolin Wang, Alla Albrecht, Hanh Mai, Carsten Woidt, Tamara Meinl, Martin Bartels, and Hartmut Hillmer, Microelectronic Engineering **110**, 44 (2013).

[71] Se Hyun Ahn and L. Jay Guo, Advanced Materials **20**, 2044 (2008).

[72] Wei Wu, Zhaoning Yu, Shih-Yuan Wang, R. Stanley Williams, Yongmin Liu, Cheng Sun, Xiang Zhang, Evgenia Kim, Y. Ron Shen, and Nicholas X. Fang, Applied Physics Letters **90**, 063107 (2007).

[73] I Bergmair, B Dastmalchi, M Bergmair, a Saeed, W Hilber, G Hesser, C Helgert, E Pshenay-Severin, T Pertsch, E B Kley, U Hübner, N H Shen, R Penciu, M Kafesaki, C M Soukoulis, K Hingerl, M Muehlberger, and R Schoeftner, Nanotechnology **22**, 325301 (2011).

[74] Bok Y Ahn, Eric B Duoss, Michael J Motala, Xiaoying Guo, Sang-Il Park, Yujie Xiong, Jongseung Yoon, Ralph G Nuzzo, John a Rogers, and Jennifer a Lewis, Science **323**, 1590 (2009).

[75] Q. Li and J.a. Lewis, Advanced Materials **15**, 1639 (2003).

[76] Jacob J Adams, Eric B Duoss, Thomas F Malkowski, Michael J Motala, Bok Yeop Ahn, Ralph G Nuzzo, Jennifer T Bernhard, and Jennifer a Lewis, Advanced Materials **23**, 1335 (2011).

[77] S Brett Walker and Jennifer a Lewis, Journal of the American Chemical Society **134**, 1419 (2012).

[78] Michael Layani, Michael Gruchko, Oded Milo, Isaac Balberg, Doron Azulay, and Shlomo Magdassi, ACS nano **3**, 3537 (2009).

[79] Jonathan a Fan, Chihhui Wu, Kui Bao, Jiming Bao, Rizia Bardhan, Naomi J Halas, Vinothan N Manoharan, Peter Nordlander, Gennady Shvets, and Federico Capasso, Science **328**, 1135 (2010).

[80] B. Partoens and F. Peeters, Physical Review B **74**, 075404 (2006).

[81] S. Morozov, K. Novoselov, F. Schedin, D. Jiang, a. Firsov, and a. Geim, Physical Review B **72**, 201401 (2005).

[82] Daniel R Dreyer, Sungjin Park, Christopher W Bielawski, and Rodney S Ruoff, Chemical Society reviews **39**, 228 (2010).

[83] Sungjin Park, Jinho An, Inhwa Jung, Richard D Piner, Sung Jin An, Xuesong Li, Aruna Velamakanni, and Rodney S Ruoff, Nano letters **9**, 1593 (2009).

[84] Boya Dai, Lei Fu, Lei Liao, Nan Liu, Kai Yan, Yongsheng Chen, and Zhongfan Liu, Nano Research **4**, 434 (2011).

[85] Xiqing Wang, Pasquale F Fulvio, Gary A Baker, Gabriel M Veith, Raymond R Unocic, Shannon M Mahurin, Miaofang Chi, and Sheng Dai, Chemical communications (Cambridge, England) **46**, 4487 (2010).

[86] Wencheng Du, Xiaoqing Jiang, and Lihua Zhu, Journal of Materials Chemistry A **1**, 10592 (2013).

[87] Mustafa Lotya, Yenny Hernandez, Paul J King, Ronan J Smith, Valeria Nicolosi, Lisa S Karlsson, Fiona M Blighe, Sukanta De, Zhiming Wang, I T McGovern, Georg S Duesberg, and Jonathan N Coleman, Journal of the American Chemical Society **131**, 3611 (2009).

[88] Jonathan N. Coleman, Advanced Functional Materials **19**, 3680 (2009).

[89] Jonathan N Coleman, Accounts of chemical research **46**, 14 (2013).

[90] Yenny Hernandez, Valeria Nicolosi, Mustafa Lotya, Fiona M Blighe, Zhenyu Sun, Sukanta De, I T McGovern, Brendan Holland, Michele Byrne, Yurii K Gun'Ko, John J Boland, Peter Niraj, Georg Duesberg, Satheesh Krishnamurthy, Robbie Goodhue, John Hutchison, Vittorio Scardaci, Andrea C Ferrari, and Jonathan N Coleman, Nature nanotechnology **3**, 563 (2008).

[91] Keun Soo Kim, Yue Zhao, Houk Jang, Sang Yoon Lee, Jong Min Kim, Kwang S Kim, Jong-Hyun Ahn, Philip Kim, Jae-Young Choi, and Byung Hee Hong, Nature **457**, 706 (2009).

[92] Ariel Ismach, Clara Druzgalski, Samuel Penwell, Adam Schwartzberg, Maxwell Zheng, Ali Javey, Jeffrey Bokor, and Yuegang Zhang, Nano letters **10**, 1542 (2010).

[93] Alfonso Reina, Xiaoting Jia, John Ho, Daniel Nezich, Hyungbin Son, Vladimir Bulovic, Mildred S Dresselhaus, and Jing Kong, Nano letters **9**, 30 (2009).

[94] Iskandar N Kholmanov, Carl W Magnuson, Ali E Aliev, Huifeng Li, Bin Zhang, Ji Won Suk, Li Li Zhang, Eric Peng, S Hossein Mousavi, Alexander B Khanikaev, Richard Piner, Gennady Shvets, and Rodney S Ruoff, Nano letters **12**, 5679 (2012).

[95] Siew Wai Poon, Wei Chen, Eng Soon Tok, and Andrew T. S. Wee, Applied Physics Letters **92**, 104102 (2008).

[96] Z. Ni, W. Chen, X. Fan, J. Kuo, T. Yu, a. Wee, and Z. Shen, Physical Review B **77**, 115416 (2008).

[97] Dmitry V Kosynkin, Amanda L Higginbotham, Alexander Sinitskii, Jay R Lomeda, Ayrat Dimiev, B Katherine Price, and James M Tour, Nature **458**, 872 (2009).

[98] Alexander Sinitskii, Ayrat Dimiev, Dmitry V Kosynkin, and James M Tour, ACS nano **4**, 5405 (2010).

[99] Dhanraj B Shinde, Joyashish Debgupta, Ajay Kushwaha, Mohammed Aslam, and Vijayamohanan K Pillai, Journal of the American Chemical Society **133**, 4168 (2011).

[100] S. Mohammadi, Z. Kolahdouz, S. Darbari, S. Mohajerzadeh, and N. Masoumi, Carbon **52**, 451 (2013).

[101] A. Krishnan, E. Dujardin, M.M.J Treacy, J. Hugdahl, S. Lynum, and T.W. Ebbesen, Nature **388**, 451 (1997).

[102] J I Paredes, S Villar-Rodil, a Martínez-Alonso, and J M D Tascón, Langmuir : the ACS journal of surfaces and colloids **24**, 10560 (2008).

[103] Graeme Williams, Brian Seger, and Prashant V Kamat, ACS nano **2**, 1487 (2008).

[104] Denis a. Sokolov, Kristin R. Shepperd, and Thomas M. Orlando, The Journal of Physical Chemistry Letters **1**, 2633 (2010).

[105] Wei Gao, Neelam Singh, Li Song, Zheng Liu, Arava Leela Mohana Reddy, Lijie Ci, Robert Vajtai, Qing Zhang, Bingqing Wei, and Pulickel M Ajayan, Nature nanotechnology **6**, 496 (2011).

[106] Yonglai Zhang, Li Guo, Shu Wei, Yinyan He, Hong Xia, Qidai Chen, Hong-Bo Sun, and Feng-Shou Xiao, Nano Today **5**, 15 (2010).

[107] Masahiro Inoue, Yamato Hayashi, Hirotsugu Takizawa, and Katsuaki Suganuma, Colloid and Polymer Science **288**, 1061 (2010).

[108] Masaya Matsuoka, Emi Matsuda, Kouji Tsuji, Hiromi Yamashita, and Masakazu Anpo, Journal of Molecular Catalysis A: Chemical **107**, 399 (1996).

[109] David R. Brown and Larry Kevan, The Journal of Physical Chemistry **90**, 1129 (1986).

[110] Paul. Mulvaney and Arnim. Henglein, The Journal of Physical Chemistry **94**, 4182 (1990).

[111] Naoto Tsutsumi, Kazuya Nagata, and Wataru Sakai, Applied Physics A **103**, 421 (2011).

[112] Sandile Ngcobo, Igor Litvin, Liesl Burger, and Andrew Forbes, Nature communications **4**, 2289 (2013).

[113] Krystian L Wlodarczyk, Emma Bryce, Noah Schwartz, Mel Strachan, David Hutson, Robert R J Maier, David Atkinson, Steven Beard, Tom Baillie, Phil Parr-Burman, Katherine Kirk, and Duncan P Hand, The Review of scientific instruments **85**, 024502 (2014).

[114] David R. Lide, *CRC Handbook of Chemistry and Physics, 85th Edition* (CRC Press, ADDRESS, 2004), p. 2712.

[115] P.B. Johnson and R.W. Christy, Physical review. B **6**, 4370 (1972).

[116] Yugang Sun and Younan Xia, Science **298**, 2176 (2002).

[117] Benjamin Wiley, Yugang Sun, Brian Mayers, and Younan Xia, Chemistry (Weinheim an der Bergstrasse, Germany) **11**, 454 (2005).

[118] Addison Ault and Gerald O. Dudek, *NMR: an introduction to proton nuclear magnetic resonance spectroscopy* (Holden-Day, ADDRESS, 1976), p. 141.

[119] John McMurry, *Organic Chemistry: A Biological Approach* (Cengage Learning, ADDRESS, 2006), p. 1024.

[120] Zongtao Zhang, Bin Zhao, and Liming Hu, Journal of Solid State Chemistry **110**, 105 (1996).

[121] Rishi Pal Chahal, Suman Mahendia, A.K. Tomar, and Shyam Kumar, Digest Journal of Nanomaterials and Biostructures **6**, 299 (2011).

[122] P. K. Khanna, R. Gokhale, and V. V. V. S. Subbarao, Journal of Materials Science **39**, 3773 (2004).

[123] Yugang Sun, Brian Mayers, and Younan Xia, Nano Letters **3**, 675 (2003).

[124] Tamas Szabo, Otto Berkesi, Peter Forgo, Katalin Josepovits, Yiannis Sanakis, Dimitris Petridis, and Imre Dekany, Chemistry of Materials **18**, 2740 (2006).

[125] W. Scholz and H. P. Boehm, Zeitschrift fi£¡r anorganische und allgemeine Chemie **369**, 327 (1969).

[126] Alexandra Buchsteiner, Anton Lerf, and Jörg Pieper, The journal of physical chemistry. B **110**, 22328 (2006).

[127] A. Thiaville, Science **284**, 1939 (1999).

[128] T. Bein and G.D. Stucky, Chemistry of Materials **8**, 1569 (1996).

[129] Geoffrey a. Ozin, Advanced Materials **4**, 612 (1992).

[130] Zhihai Huang, Xiaoli Jiang, Dawei Guo, and Ning Gu, Journal of Nanoscience and Nanotechnology **11**, 9395 (2011).

[131] David T Schoen, Alia P Schoen, Liangbing Hu, Han Sun Kim, Sarah C Heilshorn, and Yi Cui, Nano letters **10**, 3628 (2010).

[132] Dapeng Chen, Xueliang Qiao, Xiaolin Qiu, and Jianguo Chen, Journal of Materials Science **44**, 1076 (2009).

[133] Zhong-Jie Jiang, Chun-Yan Liu, and Lu-Wei Sun, The journal of physical chemistry. B **109**, 1730 (2005).

[134] Prashant Jain and T Pradeep, Biotechnology and bioengineering **90**, 59 (2005).

[135] Paul Alivisatos, Nature biotechnology **22**, 47 (2004).

[136] Prakash D Nallathamby, Kerry J Lee, and Xiao-hong Nancy Xu, ACS nano **2**, 1371 (2008).

[137] Fumitaka Mafune, Jun-ya Kohno, Yoshihiro Takeda, and Tamotsu Kondow, The journal of physical chemistry. B **104**, 0 (2000).

[138] Angshuman Pal, Sunil Shah, and Surekha Devi, Materials Chemistry and Physics **114**, 530 (2009).

[139] Carlos Miguel Gonzalez, Yun Liu, and J C Scaiano, The Journal of Physical Chemistry C **113**, 11861 (2009).

[140] R. a. Salkar, P. Jeevanandam, S. T. Aruna, Yuri Koltypin, and a. Gedanken, Journal of Materials Chemistry **9**, 1333 (1999).

[141] Maria Starowicz, Barbara Stypula, and Jacek Banas, Electrochemistry Communications **8**, 227 (2006).

[142] J.H. Zhang, H.Y. Liu, P. Zhan, Z.L. Wang, and N.B. Ming, Advanced Functional Materials **17**, 1558 (2007).

[143] Jong-Seok Kim, Journal of Industrial and Engineering Chemistry **13**, 566 (2007).

[144] Kevin Vora, SeungYeon Kang, Shobha Shukla, and Eric Mazur, Applied Physics Letters **100**, 063120 (2012).

[145] Kevin Vora, SeungYeon Kang, and Eric Mazur, Journal of Visualized Experiments 1 (2012).

[146] E Metwalli, D Haines, O Becker, S Conzone, and C G Pantano, Journal of colloid and interface science **298**, 825 (2006).

[147] EP Plueddemann, *Silane coupling agents* (Plenum Press, New York, 1982).

[148] B Arkles, Chemtech **7**, 766 (1977).

[149] K.L. Mittal, *Silanes and Other Coupling Agents* (VSP BV, The Netherlands, 2000), No. 2, p. 292.

[150] Tim Maitland and Scott Sitzman, in *Scanning Microscopy for Nanotechnology - Backscattering Detector and EBSD in Nanomaterials Characterization*, edited by Weilie Zhou and Zhong Lin Wang (Springer New York, New York, NY, 2007), pp. 41–75.

[151] Blaine Johs and Jeffrey S. Hale, Physica Status Solidi (a) **205**, 715 (2008).

[152] By Francesco Stellacci, Christina A Bauer, Timo Meyer-friedrichsen, Wim Wenseleers, Valorie Alain, Stephen M Kuebler, Stephanie J K Pond, Yadong Zhang, Seth R Marder, and Joseph W Perry, Advanced Functional Materials **14**, 194 (2002).

[153] H H Huang, X P Ni, G L Loy, C H Chew, K L Tan, F C Loh, J F Deng, and G Q Xu, Langmuir **12**, 909 (1996).

[154] I.J Haug and K.I Draget, in *Handbook of hydrocolloids Second edition Edited by*, 2nd ed., edited by G.O Phillips and P.A Williams (Woodhead Publishing, Cambridge, UK, 2009), p. 948.

[155] O.T. Bloom, Machine for testing jelly strength of glues, gelatins, and the like, 1925.

[156] Wei-Er Lu, Yong-Liang Zhang, Mei-Ling Zheng, Yan-Peng Jia, Jie Liu, Xian-Zi Dong, Zhen-Sheng Zhao, Chao-Bo Li, Yang Xia, Tian-Chun Ye, and Xuan-Ming Duan, Optical Materials Express **3**, 1660 (2013).

[157] William D. Callister and David G. Rethwisch, *Fundamentals of Materials Science and Engineering: An Integrated Approach* (John Wiley & Sons, ADDRESS, 2012), p. 910.

[158] *Modern Plastics Encyclopedia* (McGraw-Hill, ADDRESS, 1991).

[159] Janos Kirz, Journal of the Optical Society of America **64**, (1974).

[160] M. Young, Journal of the Optical Society of America. **62**, 972 (1972).

[161] Kevin Vora, Ph.d. thesis, Harvard University, 2014.

[162] Yong Zhou, Qiaoliang Bao, Binni Varghese, Lena Ai Ling Tang, Chow Khim Tan, Chorng-Haur Sow, and Kian Ping Loh, Advanced Materials **22**, 67 (2010).

[163] Z. F. Li and E. Ruckenstein, Nano Letters **4**, 1463 (2004).

[164] Olga E Philippova, Dominique Hourdet, Roland Audebert, and Alexei R Khokhlov, Macromolecules **9297**, 8278 (1997).

[165] Jian Dong, Yukihiro Ozaki, and Kenichi Nakashima, Macromolecules **9297**, 1111 (1997).

[166] Mark S. Chen, Jeremy R. Niskala, David A. Unruh, Crystal K. Chu, Olivia P. Lee, and Jean M. J. Fréchet, Chemistry of Materials **25**, 4088 (2013).

[167] Ling-Nan Zou, Xiang Cheng, Mark L Rivers, Heinrich M Jaeger, and Sidney R Nagel, Science **326**, 408 (2009).

[168] Daniel S. Corrêa, Leonardo De Boni, Lino Misoguti, Ion Cohanoschi, Florencio E. Hernandez, and Cleber R. Mendonça, Optics Communications **277**, 440 (2007).

[169] Han Zhang, Stéphane Virally, Qiaoliang Bao, Loh Kian Ping, Serge Massar, Nicolas Godbout, and Pascal Kockaert, Optics letters **37**, 1856 (2012).